Advancing Astronomical Instrumentation: an Adaptive Optics Kinematic Study of z ~ 1 Star-Forming Galaxies

by

Etsuko Mieda

A thesis submitted in conformity with the requirements
for the degree of Doctor of Philosophy
Graduate Department of Astronomy & Astrophysics
University of Toronto

Abstract

Advancing Astronomical Instrumentation: an Adaptive Optics Kinematic Study of z ∼ 1 Star-Forming Galaxies

Etsuko Mieda
Doctor of Philosophy
Graduate Department of Astronomy & Astrophysics
University of Toronto
2015

This thesis has a dual focus on improving ground-based astronomical instruments and an observational study of distant star-forming galaxies to study galaxy formation and evolution. Of fundamental importance to this work are adaptive optics (AO) technology and integral field spectrographs (IFSs), both of which offer powerful means of studying high redshift galaxies. First, I describe the design and development of an instrument to characterize the vertical atmospheric turbulence using the SLODAR (SLOpe Detection and Ranging) method. This instrument was used in a campaign at Ellesmere island (∼ 80°N) and determined that the site has half of the total turbulence residing in the ground layer (<1 km), and that the median seeing at Ellesmere is comparable to the best worldwide observing sites. Secondly, I present the design and implementation of an experimental setup to evaluate a new grating designed for OSIRIS (OH-Suppressing Infra-Red Imaging Spectrograph), an IFS at the Keck I telescope. I tested and installed a new grating in OSIRIS, and the improved sensitivity with the new grating is a factor of 1.83 between 1-2.4 μm. Finally, taking direct advantage of the improved OSIRIS performance, I built-up the currently largest sample of $z \sim 1$ star-forming galaxies taken with an IFS coupled with AO. I present the first results of IROCKS (Intermediate Redshift OSIRIS Chemo-Kinematic Survey), a spatially resolved Hα survey containing sixteen $z \sim 1$ and one $z \sim 1.5$ star-forming galaxies. The Hα kinematics and morphologies of these galaxies were investigated, including resolved star-forming clumps. These IROCKS results show that $z \sim 1$ star-forming galaxies have elevated line-of-sight velocity dispersions ($\sigma_{\rm ave} \sim 60$ km/s) compared to local galaxies yet have lower dispersions compared to their counterparts at higher redshift ($z > 1.5$). Four of the $z \sim 1$ galaxies are well-fit to an inclined disk model, and the disk fraction is similar to high-z samples. The size-luminosity relation of clumps at $z \sim 1$ is consistent with a scaled-up relation from local HII regions, but with orders of magnitude higher Hα luminosities and sizes. I confirm that the mean star formation rate surface density in clumps increases with redshift, and suggest that this favors disk fragmentation as the main clump formation mechanism.

Acknowledgements

First, I would like to thank my thesis supervisor Shelley Wright and Dunlap Institute for their unlimited amount of support and encouragement. They gave me an abundance of opportunities for research projects and extracurricular activities to make my graduates school experience unique and interesting. I would also like to show special gratitude to Bob Abraham for accepting me in his group in the last crazy six months. I always felt welcomed and belonging as a member of his team.

I am grateful to my collaborators, especially Lee Armus and James Larkin for their hospitality when I visited Caltech and UCLA, and when we were observing together. I would also like to acknowledge Jerome Maire, Stephanie Juneau, Samir Salim, Dae-Sik Moon, Sean Adkins, Jim Lyke, Randy Campbell, Tuan Do, and Jacob Gordon for their contributions to Chapter 2, 3, and 4.

I want to give special thanks to my very first research advisers James Graham and Holly Maness for inspiring me to pursue my career in astronomy.

I want to say thank you to my family for giving me everything without expecting anything in return.

And Jeffrey, without you, I am just a nice, polite, Japanese girl. With you, I am the one and only unique Etsuko.

Contents

List of Tables

List of Figures

Chapter 1

Introduction

In the mid-seventeenth century, about 50 years after Galileo Galilei first introduced refractive telescopes to astronomy, Isaac Newton studied the dispersion of light and recognized that any medium with dispersive power can produce chromatic aberration. Because mirror reflection is achromatic, he built his own reflecting telescope, and reflecting telescopes became the common basis for modern large telescopes. As telescope apertures became larger, astronomers soon realized that the atmosphere changes the positions of stars and blurs the images. For 300 years until the mid-twentieth century, astronomers had not even the slightest idea how to correct for atmospheric turbulence. It is only in the last ~ 60 years that techniques to remove the effects of atmospheric disturbance have developed.

This thesis focuses on evaluating the capabilities and limitations of ground-based astronomical observations and probing the evolution of distant, young galaxies using new observational techniques. I designed and developed an instrument to characterize the atmospheric turbulence, using a triangular method called SLODAR (SLOpe Detection and Ranging). It was tested in the lab and three different astronomical observational sites, including a 2012 site-testing campaign on Ellesmere Island in the Canadian Arctic. The instrument design and performance testing will be described in Chapter 2. I also tested and evaluated the quality of a new spectrograph grating component for an integral field spectrograph (IFS) instrument, OSIRIS, behind an adaptive optics (AO) system at the Keck telescope to further improve its sensitivity. The efficiency measurements, installation, and final throughput of the new grating and OSIRIS are reported in Chapter 3. Using this newly upgraded instrument equipped with a new, powerful AO system, we were able to build the largest sample of IFS + AO $z \sim 1$ galaxy samples. In Chapter 4, I will present the sample of sixteen $z \sim 1$ and one $z \sim 1.5$ galaxies and discuss their kinematics, star-forming properties, and their individual clumps. In Chapter 5, I compare the z~1 sample to other IFS studies, discuss their results, and touch upon future directions for the survey.

1.1 Atmospheric Turbulence

In the simple picture of atmospheric turbulence by Kolmogorov (1941, 1991), input energy is added to a fluid medium as large-scale disturbances, which are then broken down into smaller and smaller structures until the Reynolds number (*Re*) of the medium at that scale becomes smaller than a critical value. The Reynolds number is the ratio of inertial force to the viscous force and quantifies the relative importance of the two in a given fluid condition, which dictates the critical value. When the velocity and/or size of the flow is low, and/or the viscosity of the medium is high (hence *Re* is low), the input energy is dissipated immediately, and no further small structures

are created.

The Kolmogorov model describes the velocity of motion in a fluid medium (mechanical turbulence), and this turbulence can produce absolutely no visible effect to our eyes if the medium is homogeneous with no temperature and humidity variations. The optical effects of turbulence are only produced by changes in refractive index (n), which is a function of temperature and concentration of water. Mechanical turbulence mixes the medium with different temperatures and humidities at the same physical scale as the motion of the fluid.

Kolmogorov (1941) introduced a structure function to describe the turbulence. The structure function, D_f, is defined as:

$$D_f(\tau) =< [F_t(\tau)]^2 >=< [f(t+\tau) - f(t)]^2 >, \tag{1.1}$$

where <> denotes the average over t, $f(t)$ is a non stationary random function, and $F_t(\tau) = f(t+\tau) - f(t)$ is a difference function. $D_f(\tau)$ measures an amplitude of the fluctuation in $f(t)$ over a period of $\lesssim \tau$. In case where the optical effect of the turbulence is discussed, instead of the fluctuation in time, the fluctuation of the index of refraction of air in spatial scale, r, is used. The structure function of the refractive index given by the Kolmogorov model takes the following form:

$$D_n(r) = C_n^2 r^{2/3}, \tag{1.2}$$

where C_n^2 is the refractive index structure constant and measures the strength of the optical turbulence. This power low is valid between the inner scale (l_0) and outer scale (L_0). The size of l_0 can be 1 mm to 10 cm, and L_0 can be 1 m to a few hundred meters (e.g. Roddier, 1981). The values of C_n^2, l_0, and L_0 vary with time and altitude. At a typical site, C_n^2 is high ($\sim 10^{-14}$ m$^{-2/3}$) at the ground layer (0 - 1 km), where heating and cooling of the ground due to the Sun causes to change the temperature in the ambient air. As altitude increases, C_n^2 decreases ($\sim 10^{-17}$ m$^{-2/3}$) up to about 10 km height. The peak of C_n^2 occurs around 10 km in the tropopause due to wind shear in this layer. Beyond this point, C_n^2 decreases rapidly.

Turbulence in the air constantly changes the value of C_n^2, and the fluctuation in C_n^2 can be as high as an order of magnitude. To thoroughly understand sites and design telescopes and instruments, measurements of C_n^2 should be obtained over extended periods of time. In Chapter 2, I will describe our own portable instrument that measures a vertical profile of C_n^2, and briefly report the measurement results at an Arctic site.

The most commonly used parameter to quantify the wavefront distortion by the air turbulence is Fried's parameter (Fried, 1966). Fried's parameter, r_0, is a diameter over which the optical phase distortion has a mean-square value of 1 rad^2 at a wavelength of 0.5 μm, and is expressed as follows:

$$r_0 = \left(0.423k^2(\sec\zeta)\int C_n^2(h)\,dh\right)^{-3/5}, \tag{1.3}$$

where k is the wave number $2\pi/\lambda$ and ζ is an angle from the zenith. When r_0 is smaller than the diameter of the telescope D, which is usually the case, then the angular size of the image for long exposures is limited by λ/r_0, instead of diffraction limit λ/D. Even at an excellent seeing site, r_0 is $\sim$ 20 cm. This means the resolution of a telescope does not improve beyond $D > 20$ cm, and that a bigger aperture simply serves as a light bucket. When observations are taken with short exposures, a technique called Lucky imaging can be used to achieve the higher resolution for large telescopes. In Lucky imaging, carefully selected less distorted observations (usually $\sim$ 10 % of the data) are combined to produce an almost-diffraction-limited image.

Today, there are fourteen 8 to 10-m class telescopes worldwide. In the next 10 years, there will be a few 30-m class telescopes. At the 30-m diffraction-limit, telescopes are capable of reaching a spatial resolution of a few milli-arcseconds; however, under seeing-limited conditions, resolution is $\gtrsim$ 0.5 arcsecond at visible wave-

lengths. It is obvious that the gain of removing the wavefront aberration produced by the atmospheric turbulence is enormous. High resolution observations are key to numerous science programs including directly imaging extrasolar planets, measuring the orbit of the stars near the Galactic center, and evaluating substructure in high redshift galaxies. Moreover, as a consequence of increased spatial resolution, concentrated light directly improves signal-to-noise ratio (SNR), and benefit to spectroscopy and fainter source observations.

At the end of the nineteenth century, "wavefront sensing" techniques were developed to initially measure the quality of primary mirrors. These ideas began to be generalized, and the field of adaptive optics began to emerge in the 1950's (Babcock, 1953). As technology advances, the application of adaptive optics systems in telescopes become viable in the 1990's. Since then, it has performed remarkably well, providing scientific data with resolutions unprecedented in ground-base observations. In the next section, I will give an in-depth overview of the inner workings of such a system.

1.2 Adaptive Optics

Adaptive optics is an optical technique to correct for the random aberrations in a wavefront created by atmospheric turbulence in real time. Figure 1.1 shows a schematic description of how an AO system works and its functional components. In general, AO systems consist primarily of three essential activities: a wavefront sensing, an advanced control system, and a wavefront correction. The particular configuration shown in Figure 1.1 is a closed-loop AO system where the distorted wavefront hits the adaptive mirror, and the correct adjustments to the mirror are sent by the control systems a few moments later (~kHz). In contrast, when the distorted wavefront hits the wavefront sensor (WFS) first (in precise term, incoming light hits the beam-splitter first and then the WFS), it is called an open-loop system. In Figure 1.1, wavefront sensing happens at the WFS, whose information is sent to the control system where counter movement is calculated from the measurements. The control command is then sent to the adaptive mirror to operate the wavefront correction to cancel out the disturbed wavefront.

The wavefront sensing is performed by a WFS by observing a guide star which is typically a point source that generates a pure point spread function (PSF) when observed through an optical system. The wavefront produced by a guide star at infinite distance is perfectly collimated before it enters the Earth's atmosphere. When the wavefront reaches the ground it is distorted by atmospheric turbulence, and when it goes through a telescope aperture, different parts of the wavefront are focused at different parts of the image plane. A Shack-Hartmann wavefront sensor (SHWFS; Hartmann, 1900a,b; Shack & Platt, 1971), for example, uses a microlens array at the pupil to segment the pupil plane into sub-apertures. Each sub-aperture forms an image, which is just a dot, and at the image plane of the microlens array, many dots are formed. Using the deviation of observed (distorted) dot locations from the well measured locations for a plane wavefront, the path length difference and hence wavefront error is measured. We built our own portable SHWFS to measure the turbulence in the Arctic site and is described in Chapter 2.

A star that is used for wavefront sensing is called a natural guide star (NGS). In terms of wavefront, all stars are at an infinite distance and produce a plane wavefront. Unfortunately, not all NGSs are bright enough for wavefront sensing, and they are not always in close proximity on-sky to the science target of interest. When the angular separation of the NGS to the target is far ($\gtrsim$ a few arcseconds), light passes through significantly different turbulence layers, and the resultant wavefront error measured at the WFS is not applicable to the target wavefront correction. This wavefront correction limitation due to the angular separation is called angular anisoplanatism. Typically, the guide star needs to be within 2 arcseconds for visible and 10 arcseconds for near infrared (IR) observations (Hardy, 1998). In addition, even if the star is next to a target it still may not be suitable as a guide

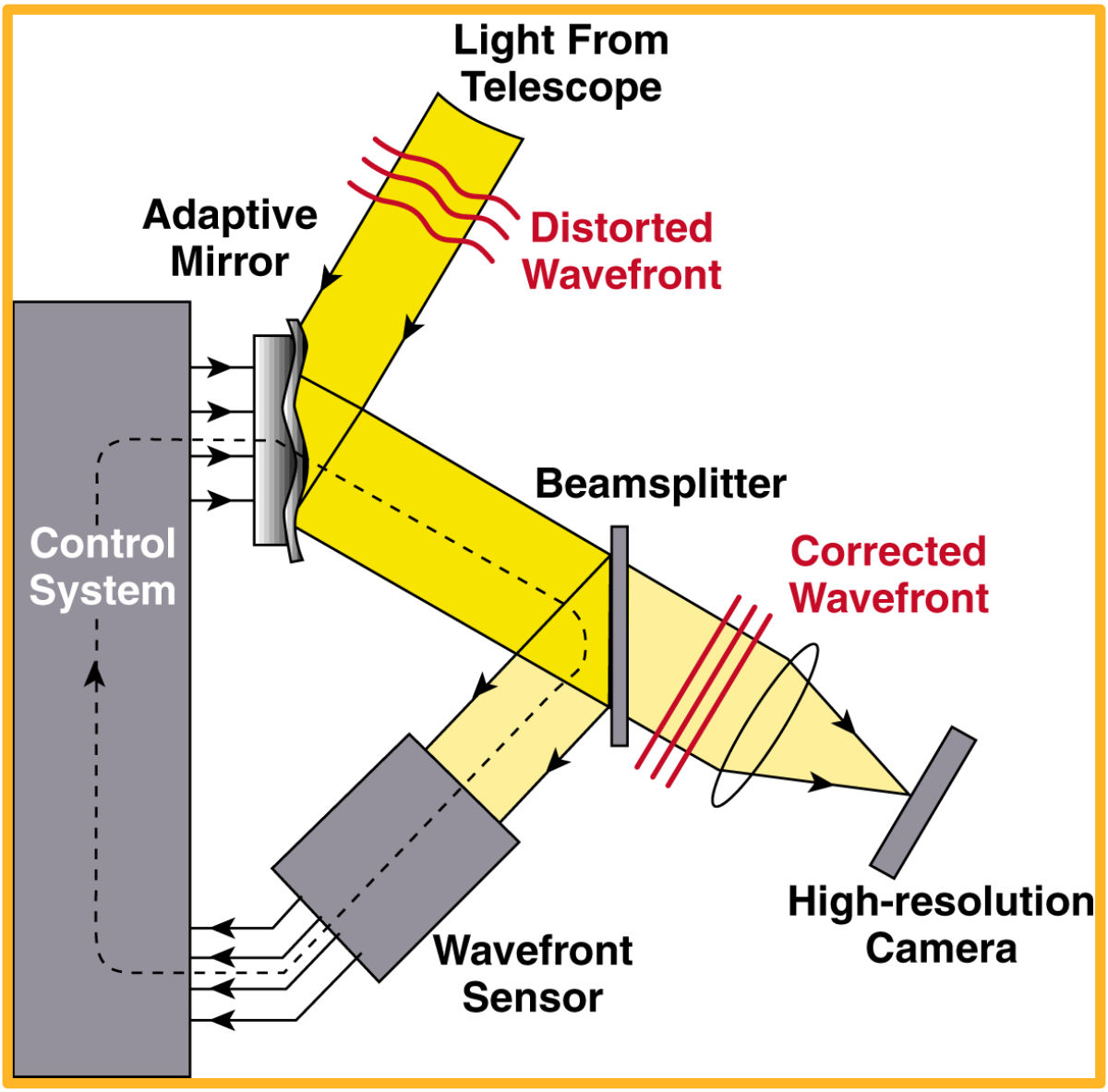

Figure 1.1 A schematic description of an AO system. It mainly consists of three parts: wavefront sensor that measures the incoming wavefront; a control or computer system; and an adaptive mirror that is able to perform wavefront correction. A distorted wavefront is measured at the wavefront sensor, and the counter motion is calculated at the control system. The command is then sent to the adaptive mirror, and the path length difference is corrected by adjust the mirror rapidly (~ kHz). This particular configuration where distorted wavefront hits the adaptive mirror first is called closed loop. Credit: C. Max, Center for Adaptive Optics.

star unless it has high enough SNR for wavefront sensing. This anisoplanatism is one of the major limitations to the NGS AO correction, which eventually led to the concept and use of generating an artificial guide star using a laser beacon.

A laser guide star (LGS) is an artificial guide star that is created by a high power laser beacon ($\gtrsim$1 W). An optical laser beacon is propagated near the optical axis of the telescope and creates a guide star near (or on top) of the science target. The laser generates an artificial star using light scattering by atoms or molecules in the air.

These scattered photons are returned to the ground and detected by a WFS. The two most common scattering types used for AO systems today are Rayleigh scattering and resonance scattering of sodium. Rayleigh scattering uses the property of back scattering from small (smaller than the wavelength) particles in the air and is able to generate an artificial star up to 30km above the telescope. The turbulence profile at higher altitudes is not detected, and hence Rayleigh scattering lasers have been primarily used for ground layer AO. Ground layer AO is particularly effective when the dominant turbulence layer is near the ground, or when science programs require correction over a wide field of view (FOV). Sodium resonance scattering, on the other hand, uses a laser at a wavelength of 589.2 nm to excite sodium atoms at $\sim$ 100 km above the ground to place the guide star as close to infinity as possible. Since sodium laser's artificial star is at a higher altitude to include most of the turbulence profile, it is preferable for good correction over a narrow FOV (anisoplanatism still limits the correctable FOV). However, the sodium atoms can be saturated, meaning all atoms are excited before they decay to produce returning photons to the wavefront sensor. Therefore simply increasing the laser power does not generate a brighter guide star. Optimized laser power and pulse duration have to be considered (Hardy, 1998). For both classes of laser, extra compensation for image motion is required using a star at infinite distance. Image motion, or tip-and-tilt (TT) motion, is an overall image displacement of up-down and right-left. It cannot be measured by a LGS because the photon returning happens within the atmosphere and thus it does not contain the whole column of atmospheric layers and beyond. Fortunately, the TT star does not need to be as bright and close to the target as for NGS since it only measures the low order aberration.

Once the wavefront error is measured at the WFS, the counter motion of the adaptive mirror is calculated, by for example, zonal or model fitting methods, at the control system. With the SHWFS, the x- and y-displacement of the dot locations measure the local wavefront slopes within a sub-aperture in x- and y-directions. With the zonal method, simply the equal and opposite slopes are applied to directly cancel out the local slopes. With the model fitting method, wavefront aberration is assumed to be a linear combination of orthogonal polynomial terms. The polynomial family that is used most often in AO are Zernike polynomials (Zernike, 1934; Noll, 1976), whose terms take the same form as the optical aberration tests (e.g., tip/tilt, defocus, astigmatism, and coma). Usually, the counter motion is calculated using a generalized least-squares solution. In the matrix form, for a $n \times n$ aperture, there are $2n^2$ measurements (n^2 for x- and another n^2 for y-slope measurements) to calculate the wavefront phase at $n \times n$ locations. Since the measurements do not form a square matrix, its inverse matrix does not exist, but the so-called pseudo-inverse can be calculated using a singular value decomposition (see for example, Southwell, 1980). The pseudo-inverse is not an actual inverse matrix, and the solution is not absolute, but it serves as the best approximation. The counter motion is then sent to the adaptive mirror, which changes the shape of the mirror surface at the same scale as the observed wavefront sensing. For instance, when 10 by 10 dots are measured with a SHWFS, there are 10 by 10 corrections applied at the adaptive mirror.

Figure 1.2 shows a point source taken at Lick Observatory 3m telescope under seeing-limited conditions (left) and with AO correction (right). The AO correction improves the angular resolution of a telescope from seeing-limited λ/r_0 to close to the diffraction-limit λ/D, and directly improves the SNR. For example, with AO correction, an observation of the Galactic center in Figure 1.3 shows not just sharp images of stars and dusts/gases but also many more faint stars. The benefits of AO are not limited to imaging observation but also spectroscopy and interferometry. More concentrated light can be placed in a narrower slit in a spectrograph and path length compensation allows longer integration times in long-baseline interferometry.

Today, almost all major telescopes are equipped with NGS and LGS AO, such as Keck I (Chin et al., 2012), Keck II (Wizinowich et al., 2006), and ALTAIR at Gemini North (Christou et al., 2010). Moreover, the development of next generation AO systems have already started. For example, bigger FOV can be corrected by using

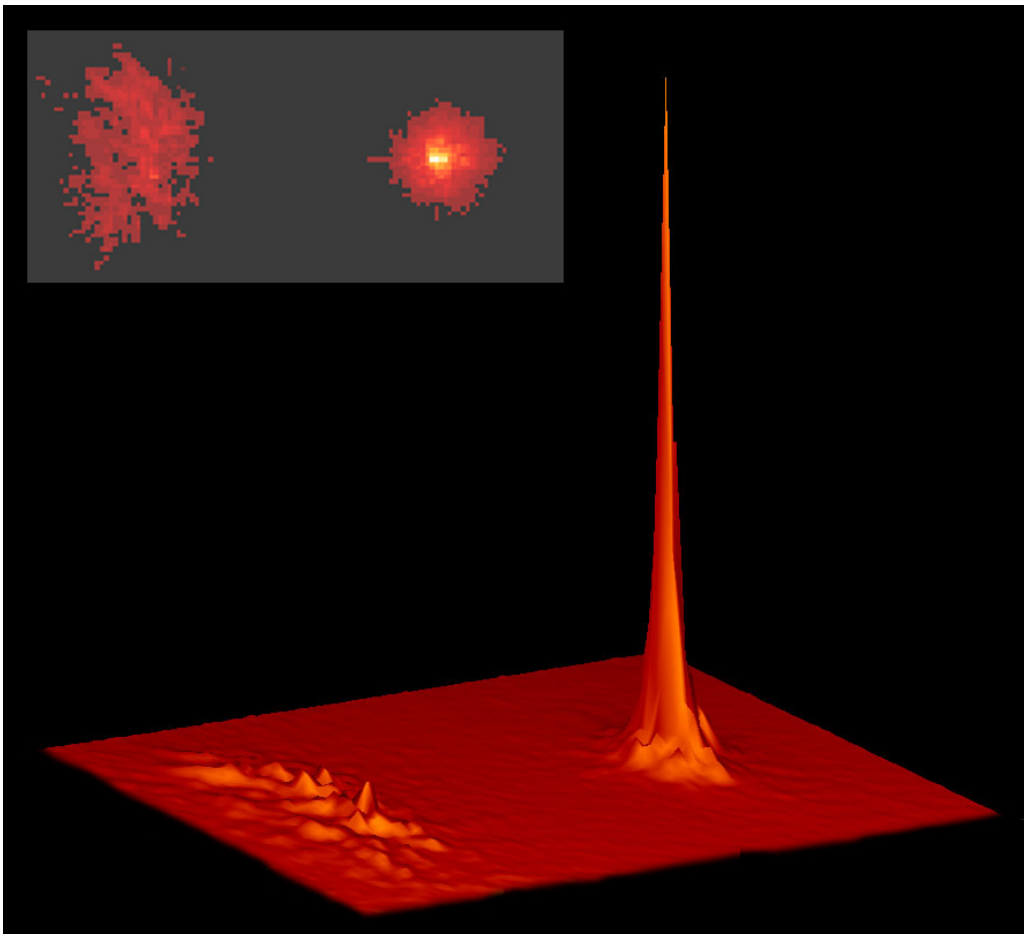

Figure 1.2 Two- (top) and three-dimensional (bottom) presentation of a PSF, without (left) and with (right) AO correction. AO correction improved angular resolution and SNR. Credit: James R. Graham with IRCAL on the Lick Observatory 3m, CfAO.

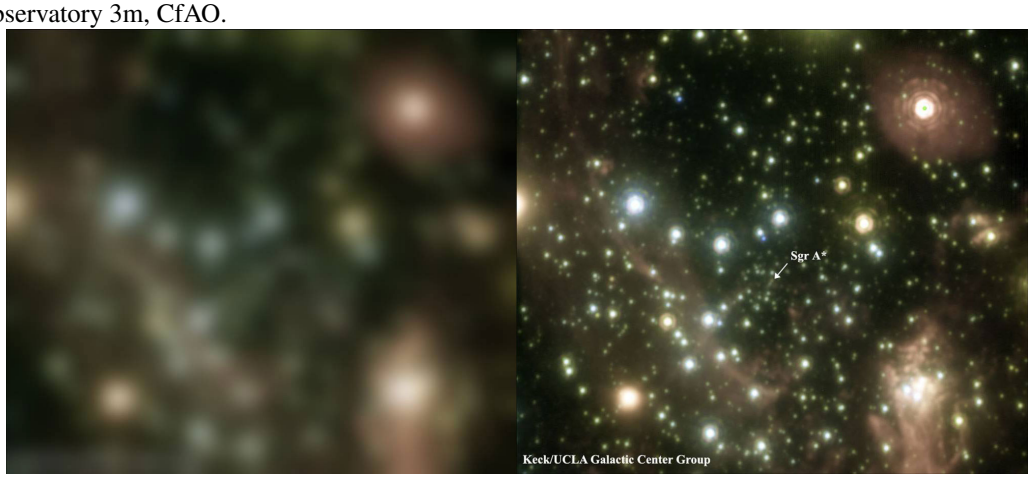

Figure 1.3 Observation of Galactic center without (left) and with (right) AO correction. Compared to non AO observation, AO observation enables the observations of structural detail and the detections of fainter objects. Credit: Keck Observatory and the UCLA Galactic Center Group.

multiple LGSs. MCAO (multi-conjugate AO: e.g., GeMS at Gemini; Rigaut et al., 2014; Neichel et al., 2014), which corrects many different turbulent layers, and MOAO (multi-object AO: e.g., Raven at Subaru; Lardière et al., 2014), which corrects many different regions of the sky, are already (or about to be) in use. For the next generation of ~30-m scale extremely large telescopes (ELT), AO systems are an essential component (see §1.1) and are designed to be ready at first light of these telescopes (e.g., NFIRAOS at TMT; Herriot et al., 2014).

The final AO correction can not be perfect since wavefront sensing and adaptive mirror AO corrections are discrete measurements while wavefronts are continuous (at least in classical physics). Theoretically speaking, increasing the number of sub-apertures in SHWFS and actuators (motors used to change the shape of the mirror surface in an adaptive mirror) will increase the correction performance; however, more sub-apertures means guide stars have to be brighter to distribute enough photons to each sub-aperture. Limitations from the brightness of the guide stars is a huge challenge, for both NGS and sodium LGS. In addition, more data points require more computational power and faster actuator movement. These are not just astronomical challenges, but directly interface with the computer processor and engineering technological abilities. Technically, these problems can be solved by spending longer time at each steps: increasing exposure time at the wavefront sensor, and allocating more time for computation and actuator control. However, as described in §1.1, the optical turbulence moves at almost the same speed as the speed of winds (~ 10 m/s) in the air, and the longer it takes, the worse the correlation between the previous measurement to the actual turbulence. New technological advancements with better wavefront sensing techniques, as well as faster control algorithms and models are needed to further improve AO systems.

When astronomical instruments are operated behind AO systems, their full potential can be achieved. Integral field spectrograph observations, which resolve targets both spatially and spectrally, in particular, benefit from AO corrections. IFSs are powerful tools to probe spatial variations of spectral features. For high redshift galaxies, these observation enable us to map various quantities of individual galaxies, such as kinematics and star formation rate. I will now move on to describe the structure of IFS instruments, and follow with a summary of how IFS+AO studies have significantly contributed to our knowledge of high redshift galaxy evolution.

1.3 Integral Field Spectrograph

Until the last few decades, the majority of optical and infrared spectroscopy has made use of single-slit spectrographs that disperse light along a single axis. The slit can be arranged on-sky either on a point-source or for a resolved source along a single orientation, and slit-based spectroscopy has been a major tool to measure rotation curves for galaxies, typically only on a single axis. However, the slit based spectroscopy can only yield sparse spatial information, and observations of the full 2D information from a resolved source have been limited. Ideally, we want to simultaneously collect spectral information across two spatial axises, x and y. This is one of the primary motivations to design and implement a new technique using an integral field spectrograph (IFS) and increase both efficiency and sensitivity for spectroscopic observations.

IFS is an optical technique that observes spatially resolved spectra over a two-dimensional field of view. The instrument consists of two main components, a spectrograph and an integral field unit (IFU) which divides the spatial field into sub-apertures. The initial design goals of IFS were to overcome the disadvantages of slit-based spectroscopy and gain the ability to (1) reconstruct a monochromatic image at any chosen wavelength, (2) study velocity fields with emission and absorption lines, (3) study physical variations, such as line ratios, across the source and (4) optimize the SNR by integrating over a larger (than slit) area (Vanderriest, 1980). The first astronomical IFS instrument was used 35 years ago by Vanderriest (1980) to observe "nebulosities" of quasars to

decipher their emission's physical origins. This prototype instrument used optical fibers to obtain more than 200 spectra per observation. Today, optics fibers is one of three main IFU techniques used to generate spectra across a 2D field of view.

The three main IFUs used in astronomy today are lenslet arrays, optical fibers, and image slicer. The IFU's primary role is to divide the field of view into many sub-apertures or "spaxels". A spaxel refers to a spatial pixel that the IFU is sampling. This name distinguishes a spatial element of the IFU from a pixel on the detector. Figure 1.4 illustrates how IFUs sample the sky and generate dispersed a spectrum for each "spaxel" on the detector.

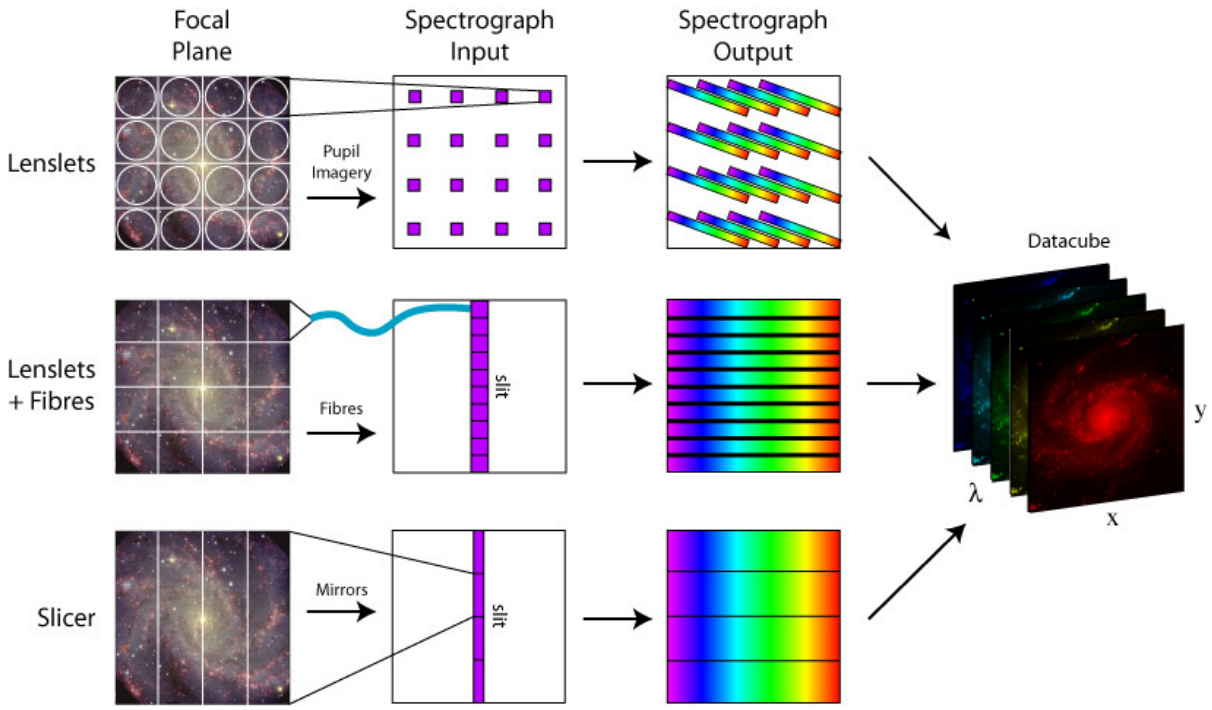

Figure 1.4 Three main IFUs, lenslet array (top), optical fiber (middle), and image slicer (bottom) to rearrange three dimensional information on a two dimensional detector. Credit: M. Westmoquette, adapted from Allington-Smith & Content (1998)

An IFU that uses a microlens array divides the telescope focal plane into separate pupil images for each spaxel location. Each pupil image is then dispersed by a dispersing element (e.g., prism, diffraction grating) and is focused linearly by a camera on a detector. The lenslet array is typically tilted with respect to the detector to avoid spectra from overlapping on the detector. Microlens array based IFSs are best suited for finer plate scales; however, due to the packing of spectra on the detector (see Figure 1.4), the spectral resolution and wavelength coverage are more limited than the other IFUs. There have been a variety of lenslet based IFUs used primarily in optical spectrographs (e.g., SAURON on the William Herschel Telescope; Bacon et al., 2001), and more recently applied in near-infrared spectrographs like OSIRIS (OH-Suppressing Infra-Red Imaging Spectrograph; Larkin et al., 2003, 2006) at the 10-m Keck I telescope, and the Gemini Planet Imager (GPI; Macintosh et al., 2006) at the 8.1 Gemini-South telescope.

The IFU technique that is most commonly used today in optical spectrographs makes use of optical fibers. Fibers can easily be bundled into a 2D array and sample the telescope focal plane. Using optical fibers also has the advantage of re-orienting the fibers from the image plane to the dispersing element, allowing spectra to neatly

fall in the middle of the detector. Unfortunately, however, fibers do not work in cryogenic temperature and thus cannot be used for longer wavelengths. Some fiber IFUs also use a microlens array in front of the fiber bundle to direct light into the fiber core more efficiently. Some examples of IFU using optical fibers with a microlens array are VIMOS (Visible Multi-Object Spectrograph; Le Fèvre et al., 2003) at 8.2-m VLT (Very Large Telescope) and GMOS (Gemini Multi-Object Spectrograph; Allington-Smith et al., 2002) at the Gemini-North and South telescopes.

An increasingly popular IFU is an image slicer that is used in both the optical and infrared regime. The use of tiny segmented mirror at the image plane of the telescope sends individual narrow image slices at slightly different reflection angles. Each image slice is then reflected by another "fanned" mirror, where individual mirrors rearrange each image slice into a single axis. Image slicer based IFUs are achromatic, make use of the whole detector pixels, and work perfectly at cryogenic temperature, but achieving small plate scales are engineeringly difficult, and the instrument itself becomes bulky due to the reflecting optical paths. Some recent examples of image slicer IFUs are KMOS (K-band Multi-Object Spectrograph; Sharples et al., 2004, 2013) and SINFONI (Spectrograph for INtegral Field Observations in the Near Infrared; Eisenhauer et al., 2003) both at VLT.

Near-infrared instrumental advancements for IFU techniques were well-timed with AO advancements on ground-based telescopes. When an IFS is fed by an AO system (§1.2), it is capable of producing high spatial resolution observations at the diffraction-limit while simultaneously providing spectra of an extended object. Near-infrared IFSs were installed on 8-10m class telescopes with AO systems only a decade ago, yet they have proven to be highly productive with a range of science topics. A few unique science studies that emerged from IFS+AO observations are: effective temperature and surface gravity of exoplanets (e.g., Chilcote et al., 2015); orbital motion and metallicity of Galactic center objects (e.g., Pfuhl et al., 2015; Valencia-S. et al., 2015; Do et al., 2015); and kinematics and star formation of lensed galaxies and AGN at high redshift (e.g., Livermore et al., 2015; Förster Schreiber et al., 2014; Riffel et al., 2015).

There have only been a few IFS designs specifically to be used with AO systems. For instance both NIFS (McGregor et al., 2003) and SPIFFI (now SINFONI) were upgraded to work with newer AO systems developed at Gemini and VLT, respectively. OSIRIS at the Keck Observatory was the first lenslet based IFU designed to work with AO. With a number of conservative design considerations, OSIRIS was designed to observe the traditional near-infrared broadbands (e.g., J, H, K) using a single, fixed grating. The original grating delivered with OSIRIS to Keck had less than optimal sensitivity, and an upgrade to this grating (if possible from industrial manufactors) would be highly beneficial to all OSIRIS science cases. In Chapter 3, a microlens based IFU instrument, OSIRIS at the Keck I telescope and upgrading of spectrograph grating component in 2012 are described. In Chapter 4, a new survey of z$\sim$1 star-forming galaxies that takes direct advantage of the upgraded OSIRIS instrument are discussed.

1.4 Young Galaxies in the Distant Universe

The launch of Hubble Space Telescope (HST) in 1990 revolutionized extragalactic astronomy and embarked on decades of discoveries of galaxies in the early universe. HST was fortuitously timed with major cosmological discoveries, like the accelerating expansion of universe and observational evidence of the lambda-cold dark matter model (Springel et al., 2006). Through our understanding of cosmology, HST has discovered some of the most distant galaxies and quasars (i.e., current highest spectroscopically confirmed redshift of a galaxy is at z=8.68; Zitrin et al., 2015). Some of HST's first discoveries were made with optical imaging cameras and revealed that rest-frame UV properties of distant galaxies were often clumpy, irregular (Glazebrook et al., 1995; Driver

et al., 1995; Abraham et al., 1996) and even "chain" like (Cowie et al. 1995a,b; also see review by Ellis 1997). Interestingly, this was in stark contrast to the more dynamically and morphologically settled galaxies observed in the local universe, where over two-thirds of local galaxies are spiral-like galaxies.

With the advent of 8-10m class telescopes with optical spectroscopy, large spectroscopic surveys (e.g., DEEP2: Newman et al., 2013a) began to build a coherent pictures of the dynamical evolution of galaxies over cosmic time. Combined with HST imaging, these ground-based optical spectroscopy surveys have offered large statistical samples and revealed global properties of high-z galaxies, such as their star formation rates, clustering, extinction, and stellar mass. For example, populations of disk galaxies up to $z \sim 1$ were identified through both their morphologies and rotation curves (e.g., Vogt et al., 1996, 1997; Lilly et al., 1998). From these large surveys, we have been able to determine that the cosmic star formation rate density peaks around $z \gtrsim 1$ (Madau et al., 1996; Lilly et al., 1996; Hopkins & Beacom, 2006; Sobral et al., 2013; Madau & Dickinson, 2014) and rapidly declines since $z \sim 1$. It has been widely recognized in the literature that AGN, stellar, and supernova feedbacks play a crucial role in regulating the growth of galaxies (i.e., rapid decline of cosmic star formation density) over a wide range of mass scales (e.g., Governato et al., 2007; Hopkins et al., 2012; Wurster & Thacker, 2013; Agertz et al., 2013). The injection of energy from these feedback mechanisms contributes to the power of turbulence in the interstellar medium, increases kinetic support in molecular clouds, and overall helps lower star formation rate. In some extreme cases, feedback can even drive outflow that removes gas from the galaxy (e.g., Law et al., 2012; Newman et al., 2012a,b).

Near-infrared spectroscopy has offered an important glimpse into the rest-frame optical properties of high-redshift ($z \gtrsim 2$) star-forming galaxies and their observed kinematics. Long-slit spectrograph studies (e.g., Vogt et al., 1996; Erb et al., 2003; Weiner et al., 2006; Kassin et al., 2012) found that $z \gtrsim 1$ galaxies typically have higher line-of-sight velocity dispersions and rotation curves that have plateau velocities similar to local spiral galaxies. These first results were tantalizing, yet were limited since these observations used a long-slit spectrograph where the velocity curves derived for each galaxy were only for a few spatial locations and along a single axis across the galaxy.

As observations expanded into the near-infrared with HST and ground-based facilities, $z \gtrsim 1$ star-forming galaxies continued to show the clumpy nature at longer wavelengths (e.g., Hα, and rest-frame optical continuum; Lotz et al., 2004; Förster Schreiber et al., 2011b). The addition of integral field spectroscopy on 8-10m telescopes has been crucial for unraveling observational clues in these distant star-forming galaxies. IFS studies have shown that globally, the majority of these systems have high velocity dispersions and high gas fractions (gas masses are estimated from Hα luminosities using Kennicutt-Schmidt law; Kennicutt, 1998) in both irregular and disk-like morphologies. IFS studies have also revealed these systems have large star-forming clumps (> kpc) (Genzel et al., 2011), where a significant fraction of the star formation is occurring. It remains challenging for theoretical models to explain the mechanisms that drive star formation in large clumps and create large scale turbulent disks (e.g., Bournaud et al., 2011; Hopkins et al., 2013). In the following, I give a summary of a few influential IFS high-z galaxy surveys; SINS (Förster Schreiber et al., 2009), MASSIV (Contini et al., 2012), and surveys by OSIRIS (Wright et al., 2009; Law et al., 2009), including WiggleZ (Wisnioski et al., 2011). In Chapter 4, I further discuss star-forming galaxies studies specifically around $z \sim 1$ redshift regime.

The SINS survey

The SINS (Spectroscopic Imaging survey in the Near-infrared with SINFONI; e.g., Förster Schreiber et al., 2006, 2009) survey was one of the first and largest (~80 targets) high-z IFS studies targeting optical nebular emission lines (Hα and [NII] emission). The majority of SINS sources are at an average redshift of z~2, and

observations were taken primarily under seeing conditions, with twelve sources using AO. The selection of sources spans a wide range of stellar masses, M_* (median $M_* = 3 \times 10^{10}$ $M_\odot$), with an overall higher stellar mass selection than other IFS studies. One ground-breaking result from this study is the detection of a large population of rotationally-supported galaxies, in particular, the deep AO observation of the galaxy "BzK-15504", which is the first high-z galaxy with a clearly defined disk-like rotation resolved in high resolution (Genzel et al., 2006). These galaxies differ from local spirals significantly due to their highly elevated velocity dispersions ($\sim$ 50 to 100 km/s) and star formation rates (SFR) (median SFR $\sim$ 70 $M_\odot$ yr^{-1}). These galaxies were also found to contain large, kiloparsec sized clumps of star formation (e.g., Genzel et al., 2011). The final survey results show roughly one-third of the observed galaxies have rotating star-forming disks, one-third dispersion-dominated, and another one-third mergers/irregulars (Förster Schreiber et al., 2009). This dynamical demographic in high-z IFS studies persists in a variety of other surveys.

The MASSIV survey

The MASSIV (Mass Assembly Survey with SINFONI in VVDS; e.g., Contini et al., 2012; Epinat et al., 2012) survey is an IFS study of galaxies at a redshift range of $0.9 \leq z \leq 1.8$. MASSIV consists of 84 galaxies (median SFR = 40 $M_\odot$ yr^{-1}, median $M_* = 1.4 \times 10^{10}$ $M_\odot$, median dispersion $\sim$ 60 km/s) with eleven sources observed with AO. They used an extra criterion for kinematic classification (rotators and non-rotators), where the kinematic position angle needs to coincide with the morphological major axis. They determined a similar distribution of kinematic populations as the z$\sim$2 SINS survey, with rotators being 44 % of their sample, non-rotators 35 %, and merger systems with close companions 25 %. Both SINS and MASSIV found that rotating galaxies are typically larger and have higher stellar mass compared to the global IFS sample (Förster Schreiber et al., 2009; Epinat et al., 2012).

Surveys by OSIRIS

Using OSIRIS at Keck Observatory, Law et al. (2007a, 2009) and Wright et al. (2007, 2009) studied thirteen galaxies at $z \sim 2$ and seven galaxies at $z \sim 1.5$, respectively. Unlike SINFONI observations, all OSIRIS observations are designed to work directly with the Keck AO system. Law et al. (2007a, 2009) sample spans a similar redshift range as the SINS survey, but lower stellar masses (median $M_* = 1.4 \times 10^{10}$ $M_\odot$) than SINS. All sources have high dispersion $\gtrsim$ 60 km/s, and five sources show velocity gradients indicative of disk systems. It is also worth noting that the Hα half light radii of Law et al. (2009) are smaller than SINS, and this may be a reason why Law et al. (2009) found fewer disk candidates. Wright et al. (2007, 2009) looked at galaxies at a lower redshift range with median $M_* = 1.1 \times 10^{10}$ $M_\odot$, average SFR = 20 $M_\odot$ yr^{-1}, and average dispersion $\sim$ 90 km/s. In contrast to $z \sim 2$ surveys, at these lower redshifts they found half of their sample well-fitted to inclined disk profiles with low residuals between observed and modelled velocities. Another $z \sim 1.3$ OSIRIS survey, WiggleZ (Wisnioski et al., 2011), targeted sources in the WiggleZ Dark Energy survey (Drinkwater et al., 2010). Half of these WiggleZ OSIRIS sources were also well fitted by disk models, yet still having elevated velocity dispersions ($\gtrsim$ 80 km/s), regardless of their velocity profile and size.

In summary, all high-z IFS studies have found that higher velocity dispersions ($\gtrsim$ 50 km/s) are ubiquitous regardless of their morphological classification. There seems to be an observed trend where the high-z disk population is found in higher stellar mass systems. Roughly 30 to 50 % of the high-z IFS sample consists of rotationally-supported galaxies, and dispersion-supported and merger/irregular in the similar proportions. There is also an observed kinematic classification difference between AO and non-AO observations, where AO observations find

more dispersion dominated galaxies while non-AO observations find more rotationally-dominated systems. Newman et al. (2013b) suggested two reasons for this observed difference: (1) smaller galaxies tend to be identified as dispersion-dominated with AO since there is insufficient sensitivity to detect the lower surface brightness emission at larger radii; and (2) non-AO observations may have beam smearing effects that smooth the velocity profiles into observed velocity gradients.

IFS observations have revealed high-z star-forming disk galaxies that are highly turbulent. One speculative explanation involves "cold flows", first explored in cosmological, hydrodynamics simulations (e.g., Kereš et al., 2005; Dekel & Birnboim, 2006; Oser et al., 2010). Cold flows represent cold gas accretion that feeds directly onto galaxies via filament structures. When a disk-like galaxy is continuously fed by cold flows, it is pushed to the edge of gravitational instability, which triggers the formation of star-forming clumps and produces strong turbulence (e.g., Law et al., 2009; Genzel et al., 2011; Wisnioski et al., 2011). Observations have shown that high-z galaxies are indeed gaseous (gas fractions of $\gtrsim 50$ %; Daddi et al., 2008, 2010; Tacconi et al., 2008, 2010, 2013) and gravitationally unstable (Toomre Q-parameter below unity; Genzel et al., 2011; Wisnioski et al., 2012). On the other hand, due to their low expected surface brightness, direct observations of cold flows remain largely elusive (precent QSO observations suggests potential evidence of cold flows: Martin et al., 2015). While cold flow is one favored explanation for the observed star-forming clumps, the precise mechanisms for the formation and evolution of high-z massive clumps are still not well constrained.

From the distant universe to present-day, galaxies have gone from turbulent star-forming systems, during which they build up their stellar mass, to settled and quiescent systems. Over this dramatic transformation, $z \sim 1$ is a critical epoch where the settling down of galactic disks and quenching of star formation begins. This redshift regime has been overlooked with IFS+AO observations due to observational challenges (lower AO performance at shorter wavelengths). The primary aim of this thesis was to improve current instrumentation to facilitate IFS and AO observations of this critical redshift regime, $z \sim 1$. In Chapter 3, I will describe the efforts to install a new grating in OSIRIS at the Keck Observatory to greatly improve the performance. In Chapter 4, I will describe our new IFS+AO surveys on $z \sim 1$ star-forming galaxies and give quantitative results on the star formation rate, kinematics and morphological parameters. I will then discuss their implications on galaxy evolution in Chapter 5.

Chapter 2

Instrument to Characterize Atmospheric Turbulence

A version of this chapter has been published in the SPIE conference proceedings as "SLODAR instrument for characterizing an Arctic site: overview of the experimental method, design, and performance", Mieda, E., Maire, J., Graham, J., R., Wright, S., A., and Moon, D., Proc. SPIE 9145, 91453K (2014). Reproduced by permission of SPIE.

2.1 Chapter Overview

We present the development of a portable SLODAR (SLOpe Detection and Ranging) instrument to measure the vertical atmosphere profile using several different telescopes (14", 16", and 20" aperture) and at varying worldwide sites. In particular, the portability and easy use of this instrument led us to operate it at Ellesmere Island in the Canadian High Arctic. We discuss the SLODAR technique, the design of the instrument, and the results of the performance tests in the lab. The results of the Arctic site testing measurements in October and November 2012 are discussed by Maire et al. (2014).

2.2 Introduction

Turbulence and temperature fluctuations in the atmosphere disturb incoming wavefronts and affect the quality of astronomical images. In ground-based observational astronomy, characterizing atmospheric quality is crucial for observation site selection, designing astronomical instruments, and optimizing their performances. Ellesmere Island in the Canadian High Arctic has been an interest for establishing a ground-based observation site, and several site testing campaigns have shown comparable seeing to the some of the best sites, such as Mauna Kea (e.g. Steinbring et al., 2013). One way to quantify the quality of the atmosphere is by measuring the refractive index structure constant C_n^2, which describes how the index of refraction varies within a given separation and yields the strength of the turbulence. The Fried parameter (r_0, seeing $\simeq \lambda/r_0$) is proportional to the vertical integral of the C_n^2 profile to the -3/5 power. The SLODAR (SLOpe Detection and Ranging) technique measures C_n^2 and wind velocity as a function of altitude using a simple triangulation method. It has already been demonstrated for several site testing campaigns (e.g. Catala et al., 2013; Goodwin et al., 2013). In 2011, we designed and built

a portable instrument to employ the SLODAR technique in order to measure detailed turbulence profile above Ellesmere Island. Including test runs, our instrument was operated at three different sites with three different telescopes: at Toronto with a 16-inch telescope, at New Mexico skies with a 20-inch telescope, and at PEARL (Polar Environmental Atmospheric Research Laboratory) on Ellesmere Island with a 14-inch telescope. In this chapter, we briefly explain how the SLODAR method works in §2.3, describe the optical and mechanical design of our instrument in §2.4, and report the result of the performance testing in the lab in §2.5.

2.3 SLODAR Method

The SLODAR method is a technique to determine the vertical profile of atmospheric turbulence. It was originally described by Wilson (2002) and further developed by Butterley et al. (2006). Rather than restating the full description of SLODAR method, we briefly summarize the method and explain the important parameters for our results here. Figure 2.1 shows a schematic of how SLODAR works: two or more stars with small angular separations (θ) are observed simultaneously by a single Shack-Hartmann wavefront sensor (SHWFS). The number

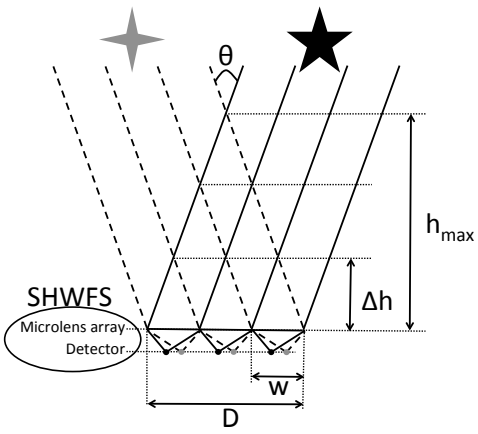

Figure 2.1 Simplified geometry of the SLODAR method. The number of subapertures (n) defines the number of layers that are resolved. The size of the aperture (D) and the separation of the stars (θ) set the height resolution (Δh) and the maximum height observable (h_{max}). The microlens array and detector combined compose a Shack-Hartmann Wavefront Sensor (SHWFS).

of subapertures defines the number of layers that can be resolved (n). The height resolution is $\Delta h = w/\theta$, where w is the size of each subaperture, which is the diameter of a telescope (D) divided by the number of subaperture ($w = D/n$). The maximum measurable height is therefore $h_{max} = n\Delta h = D/\theta$.

Two or more sets of local wavefront slopes recovered by the SHWFS are spatially cross-correlated. The thin layer turbulence model of von Kármán, with an assumed outer scale $\mathcal{L}_0$, predicts a set of spatial cross-correlation templates for each altitude, and the measured cross-correlation is decomposed into these templates by least square fitting. Since the templates are close to orthogonal, the coefficients of each template give the C_n^2 value at the corresponding altitude. The outer scale $\mathcal{L}_0$ is related to a typical distance at which the change in the structure function of the index of refraction starts to converge. For our lab experiment, we used a typical value measured at major observing sites, $\mathcal{L}_0 = 25$ m (Maire et al., 2006), that we scaled by the aperture size, constant over altitude. The detailed description of templates and decomposition are discussed in Butterley et al. (2006).

2.4 Experiment Design

The properties of this SLODAR instrument were determined by a conceptual design study. In this section, we present the instrument specifications and the observation requirements.

2.4.1 Instrument Design

The equipment required for the SLODAR experiment are a telescope and a SHWFS. A diagram of our optical layout is shown in Figure 2.2. A SHWFS consists of a collimator lens, a microlens array, and a CCD detector.

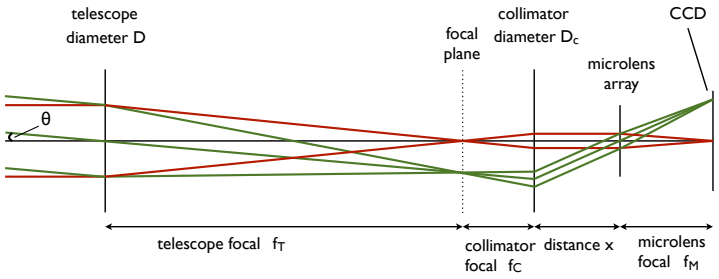

Figure 2.2 A diagram of our optical layout. A SHWFS consists of a collimator lens at its focal length (f_C) away from the telescope focus (focal length of a telescope, f_T), a microlens array at the pupil (distance from the collimator to the pupil, x), and a CCD detector at the focus of the microlens array (focal length of the microlens array, f_M). The red lines represent the on axis light rays while the green lines represent the off axis (angle of incidence = θ) light rays.

The microlens array samples the local wavefront slope as shifts of spot centroids. Among a limited selection of microlens arrays, we chose the one that has a largest pitch to maximize the photon collecting area, whose focal length is slightly longer than the distance between the aperture of the camera and the surface of the detector chip. If the focal length is too short, a special modification to the camera mount or relay optics is required to install the microlens array. If the focal length is too long, the spot size on the detector gets big and the photons are distributed over many pixels and hence lower the signal-to-noise ratio (SNR). We selected a microlens array of a size s_m = 10 mm, pitch D_m = 500 μm, and focal length f_M = 21.8 mm.

Taylor's hypothesis of frozen flow states that the turbulence is a static pattern fluctuations, e.g., refractive index variations, affected by bulk fluid flow moving at the wind speed. To capture the evolution of the atmosphere turbulence, the exposure time should be shorter than the atmospheric coherence time (<few milliseconds) and shorter than the time it takes for the pattern to be shifted by one subaperture for a given wind speed. Due to the short exposure time required to freeze the evolution of the atmospheric turbulence, we obtained an advanced Electron Multiplying Charged-Coupled Device (EMCCD) camera to minimize the effects of detector noise and provide enough photon detections. We purchased 1004 × 1002 Falcon (Raptor Photonics FA285-CL), whose pixel size is 8 μm × 8 μm, and its readout noise is <1 e^- RMS with EM gain on and <27 e^- RMS with EM gain off. When EM gain is off, the camera works as a usual CCD.

For a fixed telescope diameter and binary separation, the design involves a trade-off in the vertical resolution and SNR. For example, changing the microlens array pitch, focal length, detector pixel size, or collimator focal length can adjust the SNR and the altitude resolution. Compared to the limited selection of cameras and microlens, the vast array of commercial collimators are available, and we purchased two collimators to adjust our instrument's resolution and SNR. We acquired two collimators, both with a diameter D_C = 12.7 mm, one with a focal length

Table 2.1. Optical Parameters

Telescope	No. Layers detected	f_T	f_C	x
20" Dunlap	8	3454	30	30.26
20" Dunlap	14	3454	50	50.72
14" Dunlap	6	3556	30	30.25
14" Dunlap	10	3556	50	50.70
16" Department	5	4510	30	30.2
16" Department	9	4510	50	50.55

$f_{C,1}$ = 30 mm and one with $f_{C,2}$ = 50 mm. The larger the F/# of the collimator, the better the vertical resolution, but the lower SNR since photons are distributed over more lenslets. The principal optical parameters are listed in Table 2.1.

For our experiments, we made our SHWFS portable using a so called optical cage system. The schematic of the mechanical design is shown in Figure 2.3. In this configuration, the instrument is attached directly to the

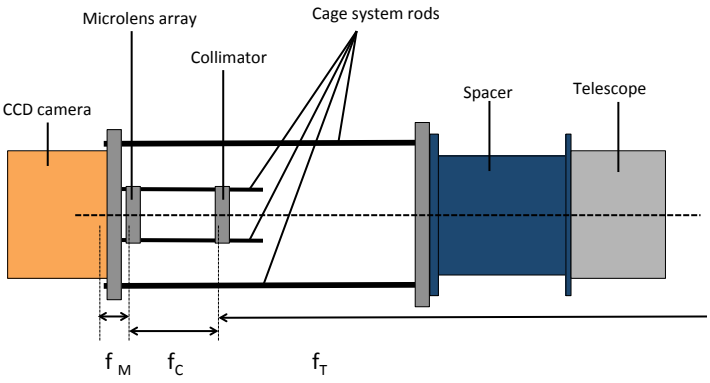

Figure 2.3 The mechanical design of our SLODAR instrument. All optical components are connected via a so called cage system, which uses four rods at the four corners to support the components.

back of the telescope without special bench requirements, making the instrument robust. This system also makes the process of switching the collimator lenses easier. A cage system connects different optical components by four rods at the corners. Instead of purchasing the rods from a store, we machined the rods to meet our length and strength requirements. The material and diameter of the rods are determined by considering the weight of the optical components, including a CCD camera, and the Young's modulus of the material. We used an 8 mm diameter 6061 T-6 Al alloy rods to connect the entire instrument to the telescope (outer rods in Fig. 2.3), and 6 mm diameter stainless steel rods to support the optical elements to the camera (inner rods in Fig. 2.3).

In order to characterize the atmosphere at the Arctic site, all optical components as well as the camera and computer have to be able to operate at extreme temperature. We purchased a compact computer, LGX AU910, which can operate at -20°C ~ -50°C. The instrument and camera operations were tested in a freezer at - 30° in the lab prior to our experiment.

Table 2.2. Target list

WDS Identifier	Name	θ [arcsec]	P_{mag} [a]	S_{mag} [b]	RA J2000.0	Dec J2000.0	H_{max} [km]
13239+5456STF1744AB	Mizar A & B	14.4[c]	2.23	3.88	13 23 55	54 55 31	7.17
01535+1918STF180AB	Gamma Arietis	7.4[d]	4.52	4.58	01 53 31	19 17 38	13.94
02039+4220STF205A,BC	Gamma Andromedae	9.5[e]	2.31	5.02	02 03 53	42 19 47	10.86
12560+3819STF1692	Cor Caroli	19.3[f]	2.85	5.52	12 56 01	38 19 06	5.35

NOTE Magnitude of the (a) primary star and (b) secondary star. Last published observation in (c) 2007, (d) 2008, (e) 2007, and (f) 2007.

2.4.2 Observation Design

The angular separation of two or more stars constrains the maximum observable altitude and the height resolution, and the brightness of the stars determines the SNR. We selected binary systems with a variety of separations that are at high elevations (more than 60 degrees) in the sky at the time of observation, and whose primary and secondary stars have magnitudes $\lesssim 6$ in the Washington Double Star Catalog (WDS) (Mason et al., 2001). Table 2.2 shows four example targets for our three different sites, Toronto, New Mexico Skies, and PEARL at Ellesmere Island. In this table, we reported the separations at the time of the last published observation. If needed, the current separation can be calculated from the orbital elements (e.g. Hartkopf et al., 2001).

2.5 Performance Tests

We tested our instrument and the SLODAR method in the lab. Figure 2.4 shows a photo (left) and schematic (right) of our optical bench. In our configuration, two light sources are separated by about 0.5°, and the maximum altitude of $\sim$ 64 cm from the detector are resolved by 13 layers ($\Delta h \sim 4.9$ cm).

Before we added any turbulence in the setup, we measured the integrated C_n^2 in our optical path. This C_n^2 is produced by the air in the lab and any systematic noise. We took 1,000 frames at the exposure time $t_{exp} = 1$ ms, and cross-correlated the local wave slopes of two light sources to calculate C_n^2. Figure 2.5 shows the integrated C_n^2, normalized by the value it converges to, as a function of the number of frames averaged. This shows that the integrated C_n^2 converges at around 200 frames.

After we find the no-turbulence-plate integrated C_n^2, we introduce turbulence in the optical path. To simulate the atmosphere, we built a "fake atmosphere layer," which consists of a clear plastic plate and a motor. The surface of the plate is covered by hair spray containing a substance called Amphomer, a polymer resin. It is rotated by the motor whose rotation speed is monitored by a power supply and multimeter. The rotation frequency [1/s] as a function of voltage (V) for our setup is measured to be $f(V) = 0.0184V - 0.0339$.

We ran several tests, changing the location of the atmosphere plate, and the speed and direction of rotation. Table 2.3 shows the summary of these measurements.

Test 1 through 6 uses one turbulence layer while Test 7 and 8 have two turbulence layers. Figure 2.6, on the left shows the integrated C_n^2, normalized to the converged value, as a function of the number of frames averaged, for the first four experiments. This shows that with the atmosphere plate, it requires about 500 frames to converge. From this result, it was determined that we would only take 500 frames for the rest of the experiments, and they

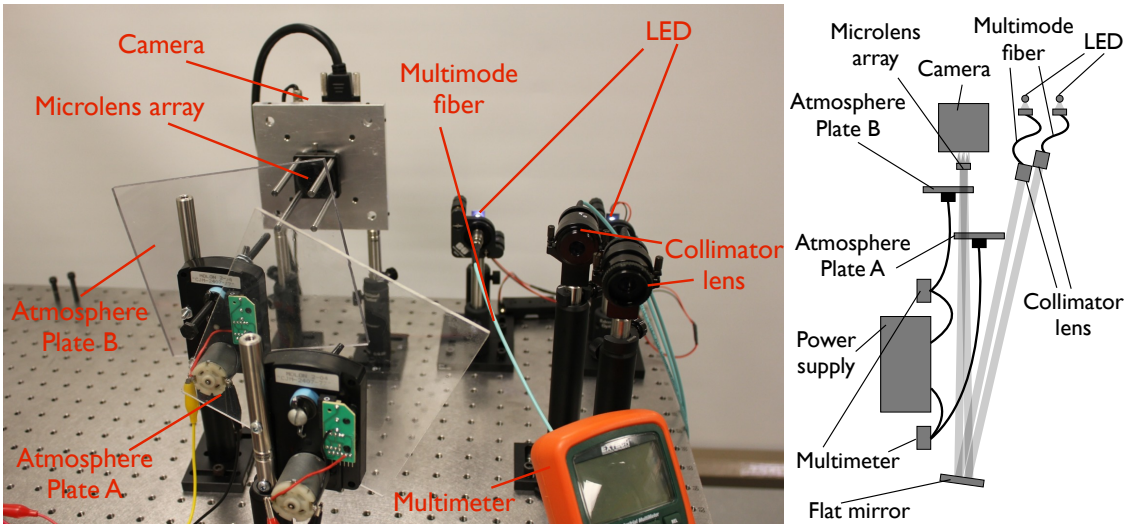

Figure 2.4 Left: Photo of our lab experiment set up. Right: Schematic of the lab experiment set up (not to scale). The light from the LED is sent to the multimode fiber, and the collimator at the end of the fiber collimates the light to a 1 cm diameter beam. Two sets of these are placed next to each other to simulate a binary star system. A flat mirror reflects the beams onto the wavefront sensor, which consists of a microlens array and a CCD detector. The distance between the LED and the flat mirror is about 72 inches, and the distance between the flat mirror and the CCD is about 80 inches. The flat mirror and power supply are outside of the photo's field of view. Instead of having a telescope to focus and a collimator to recollimate the light, the collimator lens in the wavefront sensor is removed, and the collimated beam directly illuminates the microlens array. One or two atmosphere plates are inserted between the microlens array and the maximum sensitive altitude, in our case 64 cm.

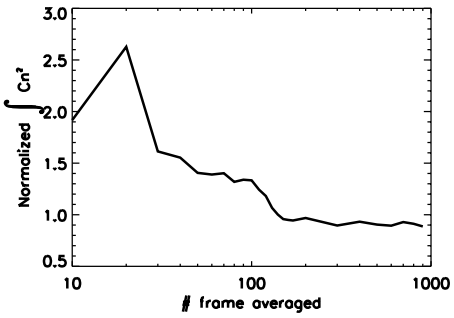

Figure 2.5 Integrated C_n^2 as a function of number of frames averaged for the no-turbulence-plate case. The integrated C_n^2 converges at around 200 frames.

were all confirmed to converge before 500 frames. The middle panel of Figure 2.6 shows the recovered C_n^2 profiles of a single layer tests, normalized by the integrated C_n^2 value, averaged at 1000 frames for Test 1 through 4, and at 500 frames for Test 5 and 6. The figure 2.6 on the right is for two layer cases averaged at 500 frames. For all tests, the altitude of turbulence layers are well detected.

The rotation speed and direction are also computed, by cross-correlating the local slopes in time. On Figure 2.7 from the left, the images show the total cross-correlation of slope frames that are separated by 1, 2, ... up to 7 time steps on the seventh image. In each image, the region that shows highest correlation, the "peak", tracks the motion of turbulence, or in this case, our plates. The right most image in Figure 2.7 is the summation of the

Table 2.3. Lab Experiments

test ID	plate	altitude [cm]	layer[a]	voltage [V]	beam[b] [cm]	WS_{in}[c] [cm/s]	ΔWS[d] [cm/s]	WD_{in}[e] [deg]	ΔWD[f] [deg]
1	A	10	3	4.8	6.5	2.22	-0.54	119	+5
2	A	10	3	3.4	6.5	1.17	-0.16	121	+3
3	A	48	10	3.4	6.5	1.17	-0.33	121	+3
4	A	25	6	3.4	5.3	0.98	-0.14	129	+4
5	A	25	6	4.8	5.5	1.88	-0.14	233	+5
6	B	10	3	4.8	5.0	1.71	-0.18	125	+5
7	A	25	6	4.8	5.5	1.88	-0.12	233	+9
	B	10	3	4.8	5.0	1.71	···	125	···
8	A	25	6	7.5	5.5	3.60	+0.13	233	+7
	B	10	3	4.8	5.0	1.71	···	125	···

[a]Location of the atmosphere plate in layer number.

[b]Distance between the beam on the atmosphere plate to its axis of rotation.

[c]Input wind speed.

[d]Difference between output (measured) and input wind speed.

[e]Input wind direction.

[f]Difference between output (measured) and input wind direction.

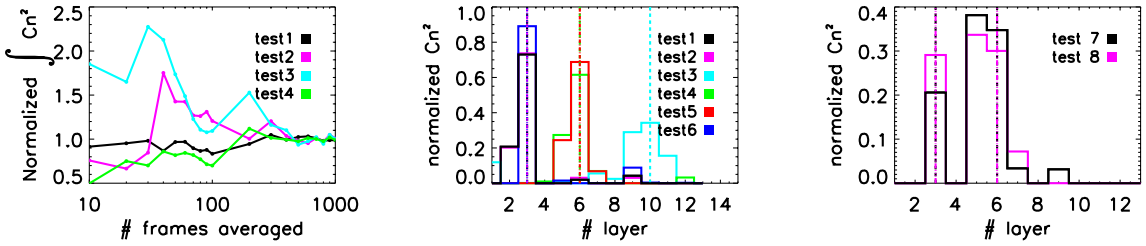

Figure 2.6 Results of the SLODAR performance tests in the lab. Left: Integrated C_n^2, normalized by the value it converges to, as a function of number of frame used to calculate the average cross-correlation function. This shows that the integrated C_n^2 value converges to ~500 frames. Middle: Recovered C_n^2 profile, normalized by the integrated C_n^2, as a function of layer number for one turbulence layer cases. Vertical dashed lines represent the actual location of the plate. For Test 1 to 4, 1000 frames are averaged while Test 5 and 6 use 500 frames. Right: Recovered C_n^2 profile, normalized by the integrated C_n^2, as a function of layer number for two turbulence layer cases. 500 frames are averaged for both cases.

first and the seventh image where it clearly shows the peak has moved from its initial location. The top row is for Test 4, which correctly measures a slower rotation speed than Test 5 in the bottom row. The difference in the direction of rotation is also correctly detected to be ~ 105°. Figure 2.8 shows the total cross-correlation of the first and the second image, the second and the third image, and so forth of Figure 2.7. The distance and the direction of the peak from the center represent the rotation speed and direction of the atmosphere plate. A two dimensional

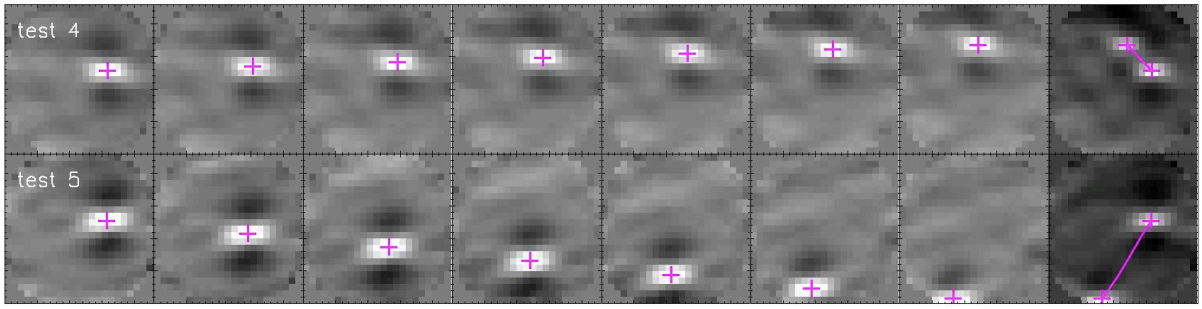

Figure 2.7 From the left, the total cross-correlation of slope frames that are separated by 1, 2, ... up to 7 time steps on the seventh figure. For example, the left most image is F1 ⋆ F2 + F2 ⋆ F3 + ..., where F1 is the frame 1, F2 is the frame 2, and so forth, and ⋆ is the cross-correlation operator, and the second left most image is F1 ⋆ F3 + F2 ⋆ F4 + ... The right most image shows the summation of first and seventh image, where it shows the peak has moved from its initial location.

Gaussian function is fitted to find the peak location.

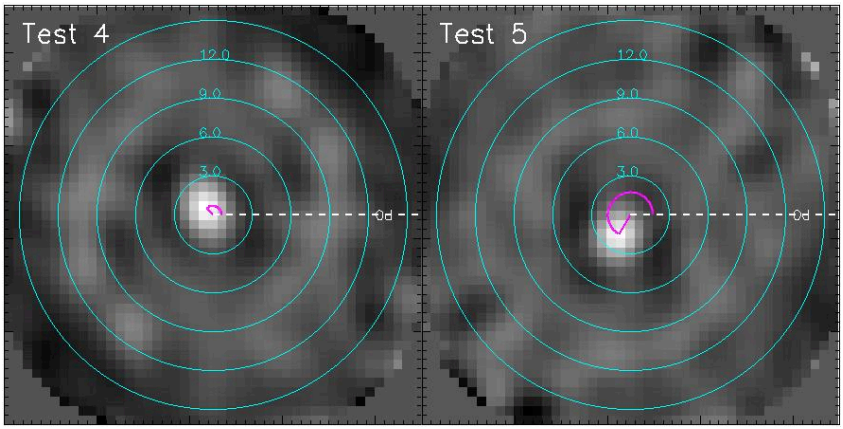

Figure 2.8 Total cross-correlation of the first and second images, second and third images, and so forth of Figure 2.7. The distance and the direction of the peak represent the rotation speed and direction of the atmosphere plate. A two dimensional Gaussian is fitted to find a peak location. The left figure shows the result for Test 4 (WS_{in} = 0.98 cm/s, WD_{in} = 129°). The difference between the measured and input wind speed is ΔWS = -0.14 cm/s, and the difference between the measured and input wind direction is ΔWD = +4°. The right figure shows the result for Test 5 (WS_{in} = 1.88 cm/s, WD_{in} = 233°) on the right. ΔWS = -0.14 cm/s, and ΔWD = +5°.

We successfully detected the rotation speed and direction of the dominant turbulence plate, but we could not detect those of the secondary turbulence plate (Test 7 and 8 in Table 2.3). The cross-correlation of the slopes in time, like in Figure 2.7, shows only one peak which corresponds to the dominant turbulence layer. It is possible that the correlation peaks are overlapping and they are not distinguishable by eye. To improve this, we need to increase the number of frames or to develop a more sophisticated wind speed extraction algorithm. The absolute C_n^2 value depends on the turbulence model, where as the wind speed, wind direction, and turbulent location are model independent.

We did not convert the relative turbulence strengths to the absolute values in the experiment, since the artificial turbulence plate likely does not follow the von Kármán turbulence model with $\mathcal{L}_0$ = 25 m. Using this particular model, as the altitude of the plate increases the absolute value of C_n^2 systematically decreases: the absolute inte-

grated C_n^2 decreases a factor of about 2.5 between test 1 (the atmosphere plate at third layer) and test 3 (the plate at 10th layer). The outer scale value we used to make the templates, $\mathcal{L}_0$ = 25 m, is a typical value for the major observing sites, but the artificial atmosphere plate is probably described by a very different $\mathcal{L}_0$ value. In the future, in order to correctly obtain the absolute C_n^2 values, we would need to characterize our turbulence plates and find which turbulence model is the most appropriate for our experiment.

2.6 Turbulence Measurements at Arctic Site

The details of actual site-testing at Canadian Arctic is described by Maire et al. (2014), but we briefly summarize the seeing and C_n^2 measurements here.

Our instrument was used to perform the SLODAR experiment at the Polar Environment Atmospheric Research Laboratory (PEARL; 80°N, 86°25'W) at 600-m elevation on October 25 to November 6, 2012. It was during the continuous winter dark night, and only interruption was a few hours of twilight per day. Due to the bad to poor weather condition, only the data on October 30 to November 2, 2012 were good enough to extract parameters. Combining four days of measurements, Figure 2.9 shows the histogram of seeing measurements. The seeing

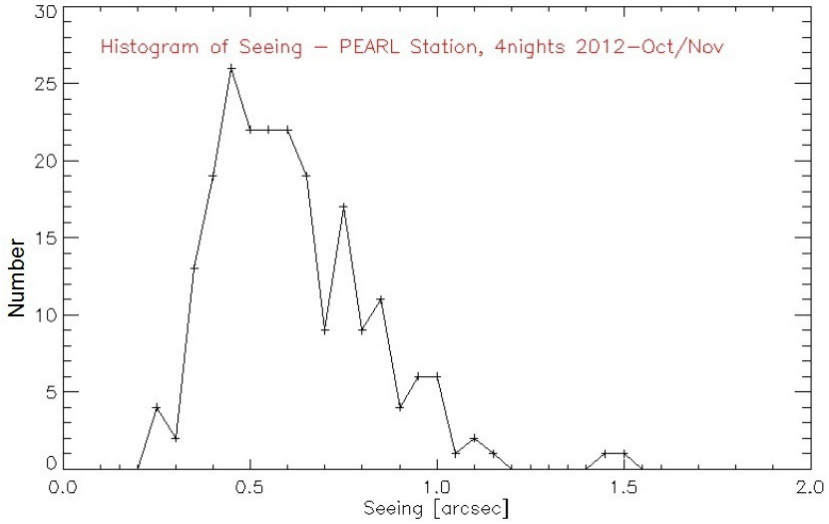

Figure 2.9 Distribution of combined seeing measurements at PEARL between October 30 to November 2, 2012. The seeing was measured from r_0 that was estimated from the residual error between the variance of measured phase and the Zernike fit. The median seeing is 0.65 arcsec.

was calculated from the Fried parameter, r_0, that was estimated using the mean-square residual error between the phase variance of the wavefront and the Zernike polynomial fit (Noll, 1976). The median seeing of four nights is 0.65 arcsec.

The average vertical profile of C_n^2 above PEARL for three nights (October 30, 31, and November 1, 2012) are shown in Figure 2.10. At this particular configuration, the height resolution is Δh = 0.6 km, maximum measurable height is h_{max} = 4.8 km, and number of layers (subapertures) is n = 8. Most of the turbulence resides near the ground, $\sim$ 50% at $\lesssim$ 1 km, and one layer at $\sim$ 2 km, and another at $\sim$ 4 km. Turbulence above h_{max} that is estimated by subtracting the turbulence up to h_{max} from the total turbulence measured from the single wavefront measurements of one of the binary star, consists about 25 % of total turbulence.

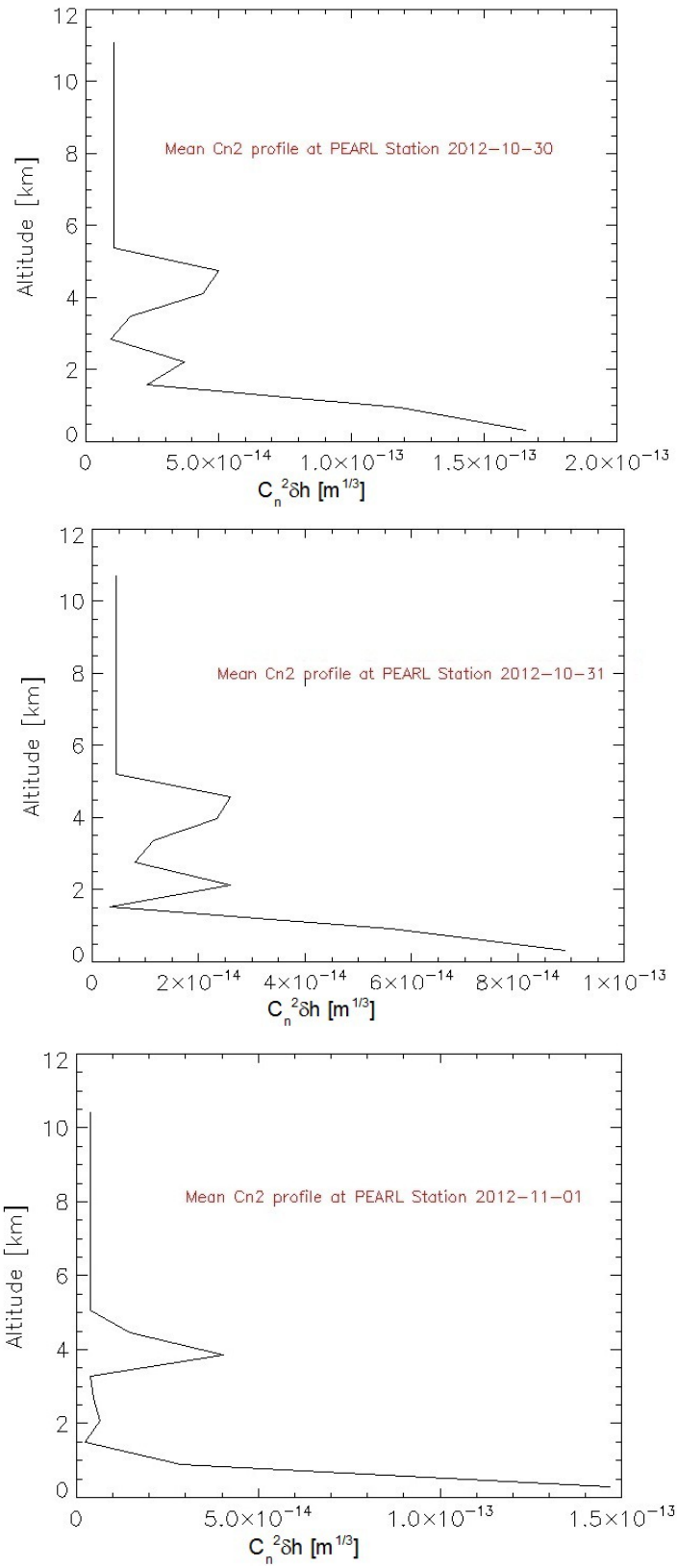

Figure 2.10 Average vertical profile of C_n^2 at PEARL on October 30 (top), 31 (midde), and November 1 (bottom), 2012. Roughly half (47 %) of the total turbulence resides below 1.2 km, two layers at ~ 2 and 4 km consists ~ 20 %, and about a quarter is distributed above 4.8 km.

2.7 Summary

We have presented the design and our testing of a prototype portable SLODAR instrument for atmospheric turbulence characterization. With this new instrument, we have successfully detected the locations, wind speed and direction of the dominant turbulence plate, and the relative strengths of the vertical C_n^2 profiles. Our instrument is simple, cost-effective, and easy to install to many different telescopes while it allows us to measure detailed profile of the atmospheric turbulence.

Our SLODAR instrument has been installed and operated on three different telescopes at three different sites. At Toronto and New Mexico, the installation of the instrument was quick ($\lesssim$ one hour), and we successfully observed several binary systems. Since these were test runs, we only briefly reduced and analyzed the data, and we are not reporting the results here. The results of atmosphere characterization at PEARL station on Ellesmere Island during a site testing campaign for the purpose of astronomical facility implementation at Arctic sites are presented in a separate paper by Maire et al. (2014).

Acknowledgements

The Dunlap Institute is funded through an endowment established by the David Dunlap family and the University of Toronto. We wish to thank Michael Williams for his technical support on the test observation at Toronto.

Chapter 3

Instrument Upgrade for the 10-m Keck I Telescope

A version of this chapter has been published in Publications of the Astronomical Society of the Pacific as "Efficiency Measurements and Installation of a New Grating for the OSIRIS Spectrograph at Keck Observatory", Mieda, E., Wright, S., A., Larkin, J., E., Graham, J., R., Adkins, S., M., Lyke, J., E., Campbell, R., D., Maire, J., Do, T., and Gordon, J., Vol. 126, No. 937, March 2014, pp. 250-263. Reproduced by permission of Astronomical Society of the Pacific.

3.1 Chapter Overview

OSIRIS is a near-infrared integral field spectrograph operating behind the adaptive optics system at W. M. Keck Observatory. While OSIRIS has been a scientifically productive instrument to date, its sensitivity has been limited by a grating efficiency that is less than half of what was expected. The spatially averaged efficiency of the old grating, weighted by error, is measured to be 39.5 ± 0.8 % at λ = 1.310 μm, with large field dependent variation of 11.7 % due to efficiency variation across the grating surface. Working with a new vendor, we developed a more efficient and uniform grating with a weighted average efficiency at λ = 1.310 μm of 78.0 ± 1.6 %, with field variation of only 2.2 %. This is close to double the average efficiency and five times less variation across the field. The new grating was installed in December 2012, and on-sky OSIRIS throughput shows an average factor of 1.83 improvement in sensitivity between 1 and 2.4 microns. We present the development history, testing, and implementation of this new near-infrared grating for OSIRIS and report the comparison with the predecessors. The higher sensitivities are already having a large impact on scientific studies with OSIRIS.

3.2 Introduction

In the last decade, the combination of a near-infrared integral field spectrograph (IFS) and adaptive optics (AO) has proven to be crucial in a range of astronomical studies from our solar system to galaxies in the early universe. Some example observations include the sulphur dioxide distribution on one of the Galilean moons, Io (Laver & de Pater, 2009), morphology of novae ejecta (Lyke & Campbell, 2009), the atmosphere of an extrasolar gas giant planets (e.g. Barman et al., 2011; Konopacky et al., 2013), the crowded stellar fields of the Galactic Center

(e.g. Trippe et al., 2008; Do et al., 2009, 2013), AGN (e.g. Davies et al., 2007; McConnell et al., 2011; Contini et al., 2012), and high redshift galaxies (e.g. Förster Schreiber et al., 2006; Law et al., 2009; Wright et al., 2009; Wisnioski et al., 2011). IFSs are also aimed to be the first light instruments for the next generation of extremely large telescopes, such as IRIS on TMT (Larkin et al., 2010), HARMONI on E-ELT (Thatte, 2010), and GMTIFS on GMT (McGregor et al., 2012).

OSIRIS (OH-Suppressing Infrared Imaging Spectrograph) (Larkin et al., 2003, 2006), a moderate spectral resolution (R ~ 3800) diffraction limited IFS for the AO system at W. M. Keck Observatory, is one of a handful of IFS instruments in use with AO systems worldwide today. It was the first diffraction limited IFS instrument to use a lenslet array as the sampling element on the sky and has plate scales ranging from 0.02" to 0.1" per spaxel[1]. OSIRIS' optics and lenslet array produce low non-common path error (<30 nm rms), a factor of approximately three times less than any other IFS, preserving the diffraction limited point spread function of the Keck AO system (Wizinowich et al., 2006).

OSIRIS was designed with a single fixed diffraction grating to ensure spectral stability and make data reduction possible with very dense spectral packing on the detector (only two pixel spacing between spectra). The grating is used in multiple orders (m) to cover traditional near-infrared wavebands: K ($\lambda_{cen} = 2.2\ \mu$m) is sampled in $m = -3$, H ($\lambda_{cen} = 1.6\ \mu$m) in $m = -4$, J ($\lambda_{cen} = 1.3\ \mu$m) in $m = -5$, and Z ($\lambda_{cen} = 1.1\ \mu$m) in $m = -6$.

While OSIRIS has been a productive instrument to date, its performance has been limited by sensitivity, which is approximately 50 % lower than its design prediction, particularly at shorter wavelengths (Z and J bands). Through our team's investigation, this performance limitation has been determined to be due to the quality of the spectrograph's diffraction grating. Since 2009 our team actively pursued acquiring a new grating for the OSIRIS spectrograph. In 2011, we began to work with the Bach Research Corporation, Boulder, CO, to fabricate a new, more efficient grating for OSIRIS. Our goal was to improve the grating performance sufficiently to double the signal to noise ratio for detector limited observations.

In this chapter, we describe our acquisition and testing of a new grating. In §3.3, we summarize the history of the OSIRIS spectrograph grating. In §3.4 we describe the laboratory setup used to measure the grating efficiency and the results of those measurements. In §3.5, we report on the December 2012 installation of the new grating. In §3.6, we discuss the on-sky performance of OSIRIS with the new grating. For those interested in equipment characterization, Appendix 3.4.1 and 3.4.1 describe camera and laser diode characterization processes in detail. For the user of OSIRIS or other IFS instruments, we introduce the OSIRIS data reduction pipeline and the modifications made after installation of the new grating in Appendix 3.7.

3.3 History of OSIRIS Grating

The OSIRIS spectrograph grating is a unique and unusual single fixed diffraction grating that has a coarse ruling of 27.93 grooves per mm at a shallow blaze angle of 5.76°. The specifications of the grating are listed in Table 3.1. The grating design was done by Richardson Gratings, Rochester, NY, in collaboration with SSG Precision Optronics, Inc., Wilmington, MA, the designers and fabricators of the OSIRIS collimator and camera three-mirror anastigmats. Over the time OSIRIS has been in service at Keck Observatory, we have installed three different gratings. They are summarized in Table 3.2. Originally, SSG manufactured two large aluminum grating blanks and provided these to Richardson Gratings for ruling. However, this first option for ruling was abandoned by them due to the large amount of tool pressure that would be required. A new vendor, Diffraction Products, Inc., Woodstock, IL, then agreed to take on the challenge of ruling this very coarse grating directly into a pure

[1] Spectrum of each spatial element.

Table 3.1. OSIRIS Grating Specification

Parameter	Value
Size	$275 \times 220 \times 50$ mm
Line Spacing	27.93 lines/mm
Blaze Angle	5.76°
Clear Aperture	205×230 mm (min.)
Surface Irregularity	150 nm RMS
Surface	Gold coating on aluminum substrate

Table 3.2. Summary of All Three OSIRIS Gratings

Grating	Manufacturer	Service Duration	*J* Efficiency
G1	Diffraction Products, Inc.	Feb 2005 - May 2005	~ 15 %
G2	Diffraction Products, Inc.	Jun 2005 - Dec 2012	39.5 %
G3	Bach Research Corporation	Jan 2013 - present	78.0 %

gold coating placed on the SSG aluminum blank. The resulting grating is identified as G1 in Table 3.2.

During laboratory testing of OSIRIS in October 2004, it was determined that G1 had a slightly varying, incorrect (6.2° instead of 5.76°) blaze angle. At high order, this puts the majority of the light into the wrong order and off the field of the detector. Efficiencies in the *Z* and *J* band were below 20% and even in the K-band was below 30%. Due to time constraints, OSIRIS was shipped to the telescope with this imperfect grating while a replacement was ordered. Diffraction products significantly improved their process and a replacement grating with the correct blaze angle (called G2) was installed in OSIRIS in June 2005.

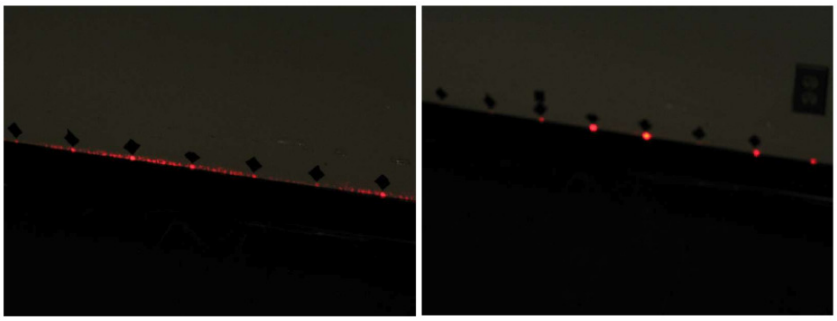

Figure 3.1 A photograph of diffraction spots at the Keck Observatory in June 2005. It shows a HeNe laser at 632.8 nm being diffracted by G1 (left) and G2 (right). The locations of diffraction spots were marked with black electrical tape above the spots. Note that G1 produces dramatic light loss between the orders compared to G2.

Figure 3.1 is a photograph of diffraction spots on a wall by G1 (left) and G2 (right) at the Keck Observatory in June 2005. The left image shows scattered light between the different orders due to incomplete ruling. This shows the improvement of the grating quality visually. The throughput measurement at the time of the servicing mission showed a gain of a factor of three to four in *J* band with a smaller gain at longer wavelengths.

Unfortunately, even with G2, the throughput was still ~ 50 % of what was expected. This was later confirmed by our team during an October 2009 servicing mission. G2 was removed from OSIRIS, and its efficiency was measured at Keck Observatory using a 1.310 μm laser (close to 5th order expected blaze wavelength) and an infrared camera. The resulting absolute efficiency measurements are shown in Figure 3.2. This was also verified

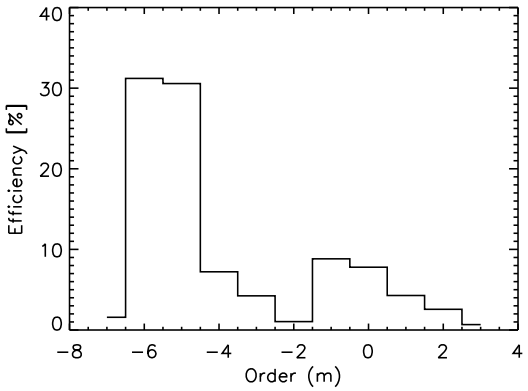

Figure 3.2 Measurements of absolute efficiency by order for G2 at the Keck summit in 2011. The blaze wavelength is 6.5 μm, so the 5^{th} order should have the maximum power at ~60 to 70 %.

with atomic force microscope (AFM) scans of G2. An AFM scan of one of the grating facets is shown in Figure 3.3. The grating facet shows a flat spot at the edge of the ruling, and the profile on the primary facet has at least two distinct angles. The effect of the curved profile on the steep side of the profile is to distribute some of the

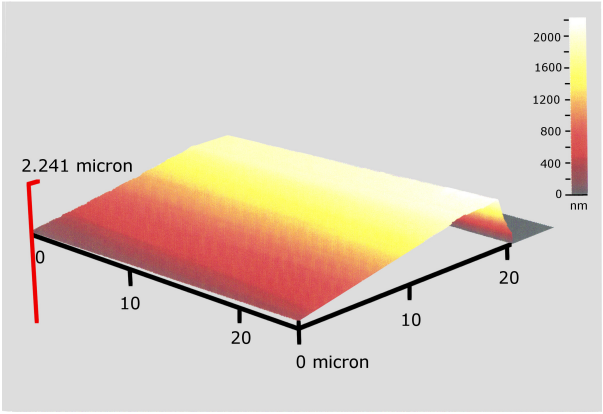

Figure 3.3 AFM scan of one of the facets of G2 made by Diffraction Products, illustrating the curved profile on the facet, which decreases the overall sensitivity in each order.

energy from the expected order into adjacent orders. The expected effect of the flat spot in the facets is that it causes some of the light to be scattered across all of the orders. We do not know if the same facet profile occurs throughout the grating, but both of these effects are clearly visible in our efficiency plot in Figure 3.2. Most likely, G2 has generally poor quality groove shapes like Figure 3.3. If all of the energy between orders -5 and -6 in Figure 3.2 were concentrated in the expected order (m = -5), the efficiency at 1.310 μm would be >60 % as expected from the specifications.

At this point, the OSIRIS team began a search for a new vendor to manufacture a better quality grating. Bach Research Corporation, formed by the founding members of the Hyperfine company, began making custom astronomical gratings, and we selected them in 2011 to begin the process of ruling a new grating on the original SSG blank.

The first and second OSIRIS gratings were directly ruled into a gold coating applied to a machined one piece aluminum grating substrate and grating mount. Rather than directly ruling into the grating substrate, Bach Research suggested that we replicate the grating onto the aluminum substrate and then coat the replica with gold. The one piece machined aluminum grating mount and substrate is an expensive component to machine, so we made use of the spare grating mount used during the first attempt of the grating by Diffraction Products. To produce the new grating, Bach Research removed the coating from G1 mount and re-polished it. This provided a new surface to apply a new ruling using a replication process. The fabrication was performed in two steps by Bach Research Corporation:

(1) A new master grating was ruled onto a Zerodur substrate (a glass-ceramic composite material produced by Schott AG).

(2) The new master was used for replication of the grating on a new coating on the spare substrate (called G3).

As part of the contract discussions for the new grating, Bach Research made a demonstration test ruling on a small 5 mm $\times$ 100 mm long substrate. A comparison of a diffraction of a HeNe laser at 632.8 nm with both this substrate and G1, taken at Bach Research is shown in Figure 3.4. The left image is the diffraction spots produced

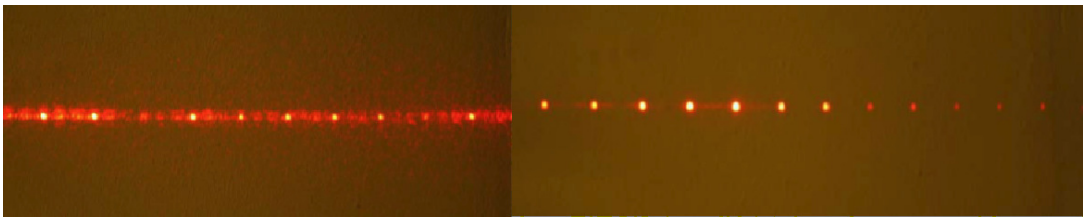

Figure 3.4 Diffraction of HeNe laser at 632.8 nm using G1 (left) and the test ruling made by Bach Research (right). The images were produced by Back Research.

by G1 and the right image is by the test ruling. The light diffracted by the test ruling is well concentrated in spots while G1 smears the light in the direction of dispersion.

One of the important challenges encountered in the manufacture of the previous gratings was that the grating maker could only evaluate the grating performance using a simple set up involving a HeNe laser with visual evaluation of the resulting dispersion and relative intensities in each order. The method used did not predict the grating's eventual performance at infrared wavelengths. Before installation of G3 we acquired an infrared laser source (1.310 μm) and infrared camera and created a set-up that allowed measurement of the grating efficiency in a reliable fashion. This allowed us to evaluate the test ruling as well as the final grating before it was installed in OSIRIS.

3.4 Grating Efficiency Measurement

To investigate the grating performance in a more robust manner, we measure the direct efficiency of the grating at λ = 1.310 μm, which corresponds to a wavelength in the J band. In this section, we describe the measurement

equipment, measurement setup, procedure, and discuss the measurement results.

3.4.1 Measurement Equipment and Stability

For the grating efficiency measurements in infrared, we used an InGaAs camera (Raptor Photonics OWL SW 1.7 CL-320) and a 1.310 μm laser diode coupled to a SMF-28 fiber (a single mode fiber with a core diameter of 8.2 μm operating at 1.310 μm to 1.625 μm). In the following section, the linearity of the camera and the stability of the laser are described. Some preliminary tests were done on a 5 $\times$ 100 mm test ruling that Bach Research fabricated in early 2012 before G3 manufacture. In summary, we find that 10 data number (DN) noise level in the camera, a 0.3 % fluctuation due to a 10°C camera temperature change, and a 3.5 % fluctuation in laser diode intensity over a one hour period.

Camera Linearity

We evaluated the linearity of the InGaAs camera, Raptor Photonics OWL SW 1.7 CL-320, by measuring the average dark counts on the detector as a function of exposure time. The 100 dark frames per grating order taken at the time of efficiency measurements were median combined to make the master dark, and the average of the master dark was plotted as a function of exposure time on Figure 3.5 left panel. All camera settings were kept

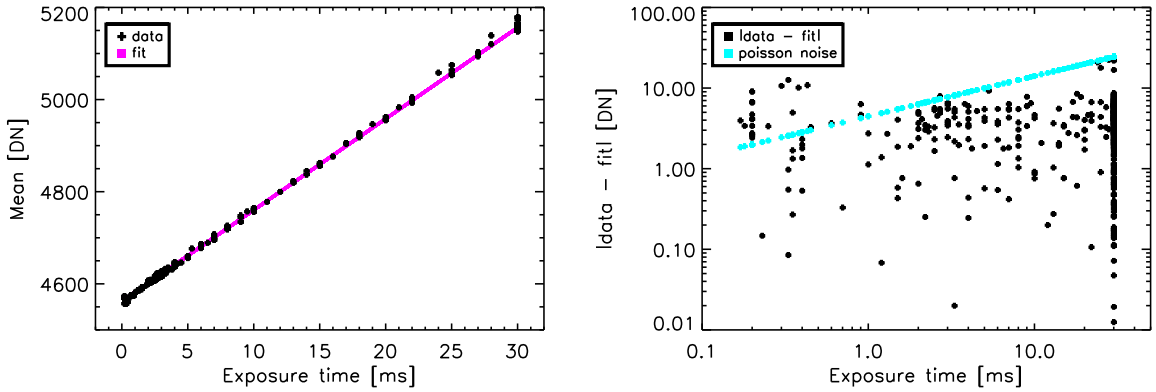

Figure 3.5 Left: Average dark counts vs. exposure time at the time of efficiency measurements. The data were fit by a straight line shown over plotted in magenta. Right: Absolute difference between the average dark count and the linear fit plotted as a function of exposure time, with the Poisson noise overplotted in cyan.

fixed for all times except for the exposure time. Figure 3.5 on the right shows the absolute difference between data points and the straight line fit, with the Poisson noise over plotted in cyan. The result shows that regardless of the exposure time, there are about 10 DN fluctuations until the Poisson noise takes over at around t_{exp} = 10 ms. Hence, we include 10 DN in the noise calculation.

We also looked at the effect of the camera temperature over an hour, which is the amount of time taken for an efficiency measurement of a single spatial position on the grating surface over a large range of orders. In this test, we took images of the laser spot at t_{exp} = 0.2 ms every 60 seconds for one hour and repeated the process twice. During the test, the camera and the laser were kept on all the time. The laser was imaged to include the effect of the laser heating up the image sensor in case that happened. Figure 3.6 shows the changes of two different camera temperatures over one hour period. Our input temperature (TEC temperature) was always 15°C, and the sensor

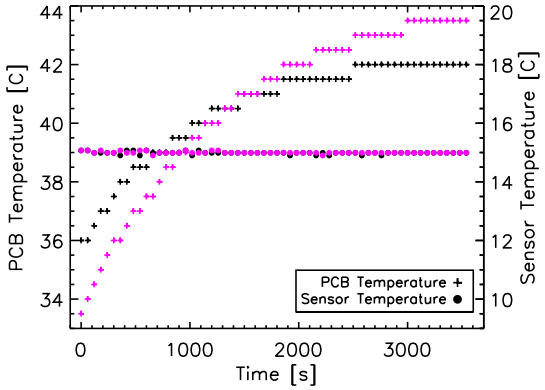

Figure 3.6 Sensor and PCB temperature changes over one hour. With the TEC temperature set to 15°C, the sensor temperature stayed almost constant while the PCB temperature increased 5 to 10°C. The magenta points are the measurements from the first test, and the black points are the measurements from the second test.

temperature was almost always constant around 15°C, but the printed circuit board (PCB) temperature increased about 10°C during the first test and about 6°C during the second test over a one hour period.

During G2 and G3 efficiency measurements combined, most samples were taken at t_{exp} = 30 ms. This is because G3 and G2 efficiency measurements were all taken with a frame rate of 25 Hz, and taking into account the trigger delay and data transfer, we set the maximum exposure time to be t_{max} = 30 ms. The exposure times for individual measurements were chosen to maximize signal level while maintaining the exposure below the saturation, but since we set a maximum exposure time threshold, many fainter spot images were taken with the maximum exposure time.

Figure 3.7 shows normalized average dark counts, as a function of the PCB temperature change. The flux

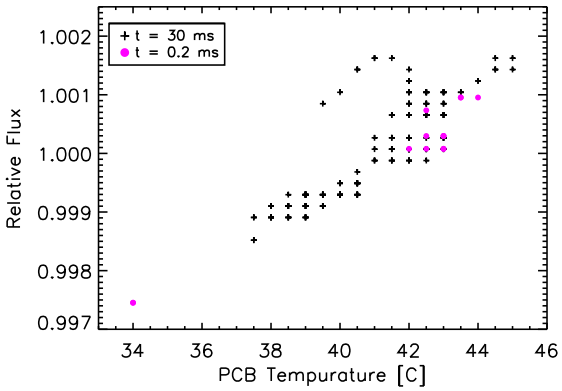

Figure 3.7 The relative flux change of t = 30 ms (black) and t = 0.2 ms (magenta) average dark counts due to the PCB temperature change.

increases about 0.6 % as the PCB temperature increases about 10°C. We do not have the information on how long the camera was turned on during the experiments, but we know that to measure the full efficiency at one location, it takes about one hour, and in one hour the PCB temperature changes about 10°C (Figure 3.6). Combining

this information and Figure 3.7, we take 0.3 % (a half of the full increase in flux) as noise due to camera PCB temperature changes during the efficiency measurements.

Infrared Laser Diode Stability Test

We used a 1.310 μm laser diode coupled to a SMF-28 fiber as a light source for infrared measurement. To ensure consistency in our measurements, we measured the stability of the laser by monitoring its intensity using the infrared camera tested above. First, we fixed the exposure time to t_{exp} = 0.2 ms and took a series of images separated by three time intervals: 5, 20, and 60 seconds (Figure 3.8). The camera and the laser were kept being

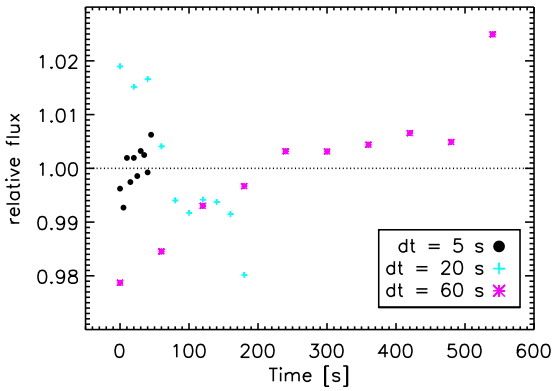

Figure 3.8 Relative flux of the 1.310 μm laser diode verses time for three time intervals: 5 (black circle), 20 (cyan cross), and 60 (magenta star) seconds.

on until all measurements in a particular sequence were completed. These measurements allowed us to search for any time dependent instabilities in the combined system of laser and camera. We found the fluctuation in the system seems independent of the time interval of data taken but dependent on the duration of the laser is on.

The polarization of stimulated emission is parallel to the diode junction plane, and thus laser diodes are usually linearly polarized. When a laser is used in a polarization dependent setup, intensity fluctuations can occur due to changing polarization states. Our laser diode is coupled to a SMF-28-J9 step-index fiber with a numerical aperture (NA) of 0.14 and an 8.2 μm diameter core. For this fiber, the dimensionless normalized frequency or normalized thickness of the guide (V) is,

$$V = kd(NA), \tag{3.1}$$

where k is the wave number, and d is the fiber core radius (e.g. Iizuka, 2002) of 2.75 at 1310 μm. The first critical frequency (cutoff V) for single mode operation is 2.405, and therefore our fiber supports four polarization modes. To understand the polarization characteristics of our laser, we tested the laser stability with and without a calcite polarizer in the optical path. We took a series of images of laser beam for an hour at 60 s intervals. We performed these measurements twice: once with a calcite polarizer in front of the laser and once without the polarizer. The polarizer was oriented so that the output beam had the maximum intensity (direction of the polarization of the laser is parallel to the direction of polarizer). After one hour of measurement, we verified that the peak intensity from the polarizer was still at the same angle. This means, over one hour, the polarization state of the laser did not change, and therefore we assume the laser polarization state does not change during the efficiency measurements.

Figure 3.9 shows that the laser flux fluctuates 3.5 % (one-half of (highest - lowest) flux) over one hour. The

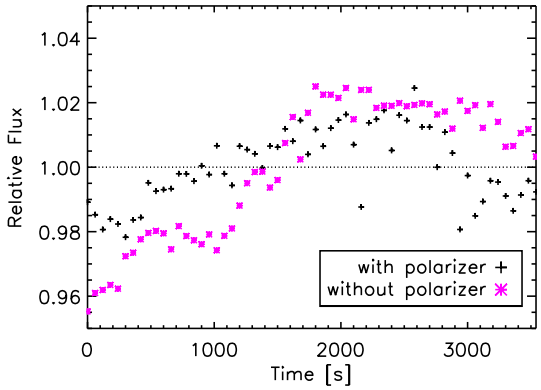

Figure 3.9 Relative flux of the 1.310 μm laser diode versus time for a 60 second interval with a polarizer (black) and without a polarizer (magenta).

initial discrepancy up to 1000 s between the measurements with and without the polarizer is probably due to room/detector temperature differences because the two measurements were taken on different days. Since the polarization state of the laser did not change over one hour, this variation is probably from the laser itself as shown in Figure 3.8. We take into account this 3.5 % laser flux variation in the noise calculation.

3.4.2 Measurement Setup and Procedure

To measure the efficiency of the grating at the same configuration as in OSIRIS, we set up an optical path on an optical bench, where the angle of incidence (α) is $\alpha = -30.2°$, and the angle of diffraction (β) for $m = -5$ at 1.310 μm is $\beta = 18.4°$. We define the sign conventions and orientation for the OSIRIS grating used throughout our measurements in Figure 3.10. In our setup, the incident angle is accurate within 1°, which is theoretically a <1

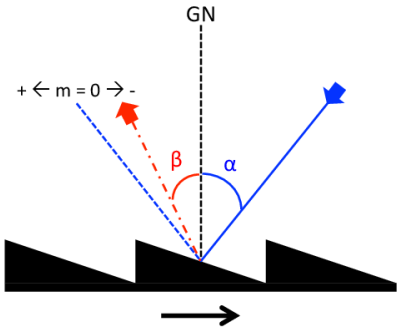

Figure 3.10 Orientation of OSIRIS grating blaze direction (black arrow), incident angle α (blue and negative), and outgoing angle β (red, dot-dash line and positive). Negative orders are defined to be in the direction towards the grating normal (GN) from $m = 0$ (pure reflection).

% change in $m = -5$ efficiency at 1.310 μm (Figure 3.11) using our Rigorous Coupled-Wave Analysis (RCWA)

(Moharam & Gaylord, 1981) code. RCWA is a semi-analytic computational method used to solve Maxwell's

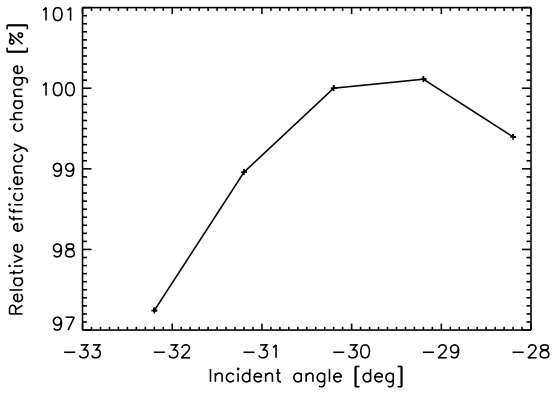

Figure 3.11 RCWA analysis prediction of the theoretical $m = -5$ efficiency change at $\lambda = 1.310$ μm due to the incident angle change. With a 1° change in the incident angle, the change in efficiency is less than 1%.

equations. Our code uses this method to calculate the portion of light being diffracted into different orders by a diffraction grating for the given grating specification (our grating specification can be found in Table 3.1) and the incident angle.

A 1.310 μm laser diode that is coupled to a SMF-28 fiber is connected to an attenuator and a collimator. The collimated laser beam goes through two neutral density (ND) filters and hits the grating surface, where it is diffracted into constituent orders. An achromatic lens pair focuses the beam on the InGaAs camera, which sits on a dovetail optical rail system. The beam's full-width-half-maximum at m = -5 is about 1.7 mm on the camera. The schematic of the configuration is shown in Figure 3.12 on the left, and a photo of the setup is on the right. An aluminum baffle box resides over the entire experiment to eliminate scattered background light. All

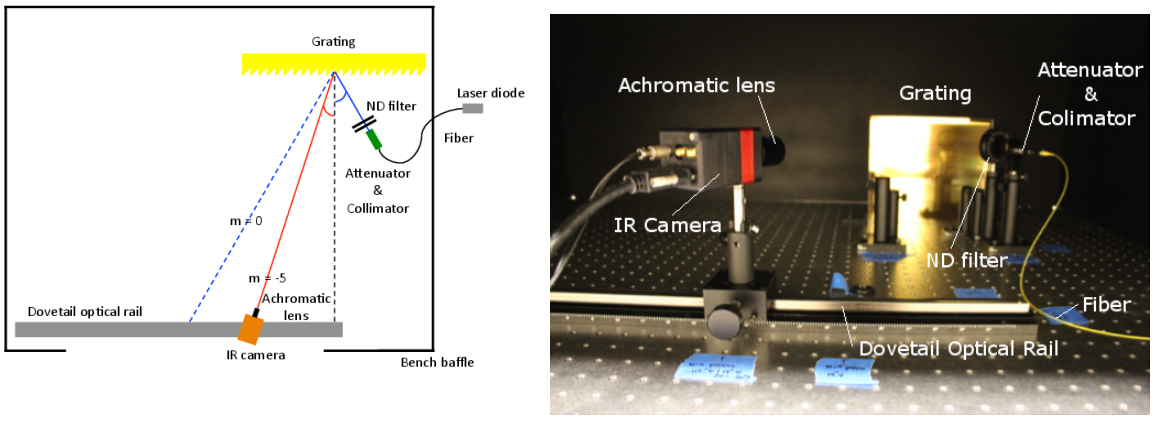

Figure 3.12 Left: Schematic of the efficiency measurement configuration in the lab (not to scale). The entire setting is covered up by an aluminum baffle box to control background and scattered light. Right: A photo of the efficiency measurement configuration in the lab.

the components, except the grating, were kept fixed onto the optical bench until all efficiency measurements were completed. Every time we left the lab, the grating was carefully packed and put away in a secured location.

The collimator focal length and the optical path length were determined by considering the divergence angle of the laser with the goal of keeping the final spot size well inside the detector field of view (FOV). The attenuator and combination of two ND filters are employed to ensure that the final spot on the detector is not saturated at a reasonable exposure time for the brightest order with good signal to noise ratio on the faintest orders. The achromatic camera lens pair is chosen so that only one spot falls on the camera's detector at a time.

The efficiency is defined as the flux of monochromatic light diffracted into the order being measured relative to the total flux. We measure the reflection of the same light source from an un-ruled area on the grating/test ruling (called pure reflection) and use this as the total flux. Since the un-ruled part of the grating/test ruling is outside of the clear aperture, and the quality of its surface is not guaranteed, we also use the total sum of all orders (called order sum) as a measure of the total flux as well. Efficiency measurements using both values for total flux are presented in this chapter.

A typical efficiency measurement procedure is as follows: 1) set up the grating for the pure reflection; 2) close the bench baffle; 3) find the best exposure time and measure the pure reflection with the laser on; 4) measure the pure reflection with the laser off; 5) open the baffle; 6) set up the grating to place the first order to be measured in the camera's FOV; 7) close the baffle; 8) find the best exposure time and measure the flux with laser on and off; 9) move the IR camera to the next order; and repeat step 8 and 9 until all orders are measured. In these tests, we measured $m = -13$ to $m = 8$. It takes about one hour to complete this procedure. Since we know that the polarization state of the fiber does not change in one hour (§3.4.1) but moving the fiber changes the polarization state of the beam, we were very careful not to touch the fiber during the entire procedure.

The ruled area of the OSIRIS grating is 205 × 230 mm. To assess the spatial dependence of the efficiency, measurements are made at nine locations (3 by 3 configuration) across the grating surface as illustrated in Figure 3.13.

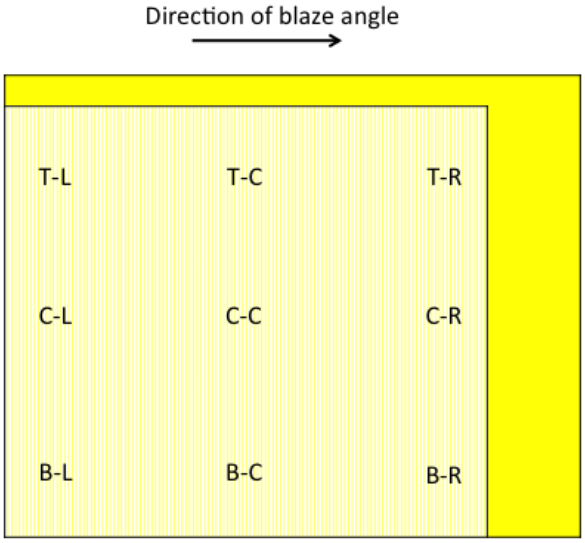

Figure 3.13 Diagram showing the location of the grating efficiency measurements. The light yellow area is the region of the ruled area, 205 × 230 mm. The bright yellow area is the overall area of the substrate. The arrow indicates the direction of blaze angle.

After the efficiency at one location is measured, we move the grating sideways or change the height of the stage, where the grating sits, to move to the next location. The grating surface is kept parallel to the dovetail

optical rail, and the optical path length is kept the same for all measurement. This allows us to keep the setup fixed as much as possible.

For each grating order, we acquire 100 frames with an additional 100 background frames. The 100 background frames are median combined to make a master background and subtracted from each science frame. Then 100 background subtracted frames are median combined and divided by the exposure time to make the final reduced image. To conserve the optical alignment, we do not take flat frames. A histogram of a normalized flat field taken during testing shows a normal distribution with a standard deviation of 0.024. Instead of applying flat fielding to the final reduced image, we include the flat field fluctuation of 2.4 % as a part of measurement uncertainties.

The grating efficiency is measured by summing up the flux in an individual spot at a particular order and dividing by the total flux. To confirm that we collect all flux in an individual spot, we tested two methods. One is by Gaussian fitting. A two dimensional Gaussian function is fitted to the final reduced image, and aperture photometry is applied to both the reduced image and the 2D Gaussian function. Figure 3.14 on the left shows

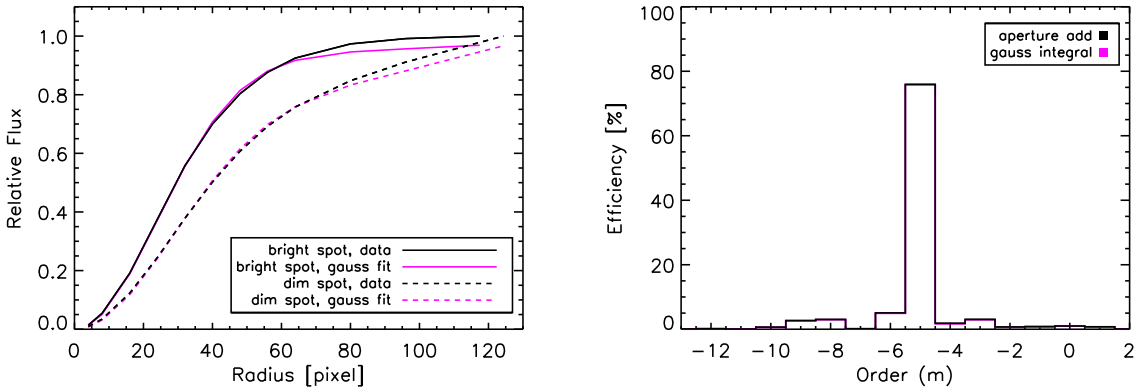

Figure 3.14 Left: Growth curves of the reduced image (black) and 2D Gaussian fit (magenta) for the test ruling. The solid lines are for the brightest spot, and the dashed lines are for a dim spot whose optical path is the longest whose size is therefore the biggest on the detector. Right: Efficiency of the test ruling with respect to the pure reflection. For the two cases, a circular aperture applied to the reduced image (black) and Gaussian fit integral (magenta), the efficiencies are almost on top of each other.

the growth curves of the reduced image (black) and the Gaussian (magenta) for the test ruling. They are both normalized to the reduced image total flux. The solid line is the growth curve of the brightest spot, and the dashed line is of a dimmer spot. The optical path of the dimmer spot is the longest and thus the spot size is biggest on the detector due to the divergence angle of the laser beam. The maximum radius on the plot is the radius of a biggest circle that can be fitted in the frame centered at the Gaussian fit center. For both bright and dim spots, two lines are quit similar. Figure 3.14 on the right shows the efficiency of the test ruling with respect to the pure reflection, using the aperture photometry of the reduced image (black) and the integrated sum of the Gaussian to infinity (magenta). Two plots are almost exactly the same.

The growth curve and efficiency comparisons illustrate that our experiment and optical setup is optimized with respect to the laser spot size at the detector and the detector plate scale. Since two cases give similar answers, we deploy the simple aperture photometry method to the reduced image to calculate the total counts in a spot.

There were two efficiency requirements defined by Keck Observatory and our team which the new grating (G3) had to meet in order to be eligible for installation in OSIRIS:

Table 3.3. G3 Peak Efficiency at 1.310 μm

Location	Left	Center	Right
Top	82.5 ± 5.1 %	76.8 ± 4.7 %	80.4 ± 5.0 %
	78.2[a] %	77.9 ± 4.2 %	79.2 ± 4.5 %
	1.05	0.99	1.01
Center	76.9 ± 4.8 %	76.7 ± 4.7 %	79.3 ± 4.9 %
	76.4 ± 4.3 %	76.3 ± 4.3 %	79.4 ± 4.4 %
	1.00	1.01	1.00
Bottom	77.6 ± 4.8 %	75.2 ± 4.6 %	77.9 ± 4.8 %
	77.6 ± 4.3 %	76.1 ± 4.1 %	79.3 ± 4.3 %
	1.00	0.99	0.98

NOTE At each location, there are three values. The first one is the efficiency with respect to the pure reflection, the second one is the efficiency with respect to the order sum, and the last one is the ratio of the order sum to the pure reflection. All values are shown with the associated measurement errors.

[a] After we reduced all data, one of the original data file (m = 6 at top-left) was corrupted before we calculated the random observation uncertainty. Thus, the efficiency value is reported here, but not the measurement uncertainty.

(A) Global efficiency requirement: On average, the new grating has to be at least 50 % more efficient than G2, which means >45 % in J-band (1.310 μm).

(B) Field dependent efficiency requirement: The efficiency of the new grating has to be better than G2 efficiency (<30 %) at all location across the grating.

In the next section, we report the results of the new grating efficiency measurements.

3.4.3 New (G3) and Old (G2) OSIRIS Grating Efficiencies

Before G3 was shipped to the Dunlap Institute for Astronomy & Astrophysics (Dunlap) in July 2012, Bach Research assessed the quality of the wavefront of G3 surface with a 4 inch aperture Zygo interferometer. Bach Research took wavefront measurements along the center of the grating and moved the aperture from start to the end of the ruling. They performed these measurements across several optical orders to yield an indication of wavefront error over the entire surface. The wavefront quality across the surface is roughly ± 0.5 wave at λ = 632.8 nm.

The peak efficiency ($m = -5$) of G3 with respect to the pure reflection at λ = 1.310 μm at nine spatial locations across the grating surface are summarized in Table 3.3, and Figures 3.15 shows detailed efficiency for -13 ≤ m ≤ 8. At all nine locations, the peak efficiencies are more than 75 %, and the average efficiency, weighted by error, is 78.0 ± 1.6 % with respect to the pure reflection, and the non-weighted average of 77.8 % with respect to the order sum (see footnotes in Table 3.3). This grating meets both global and field dependent efficiency requirements stated in §3.4.2, which led our team to install G3 in OSIRIS in December 2012.

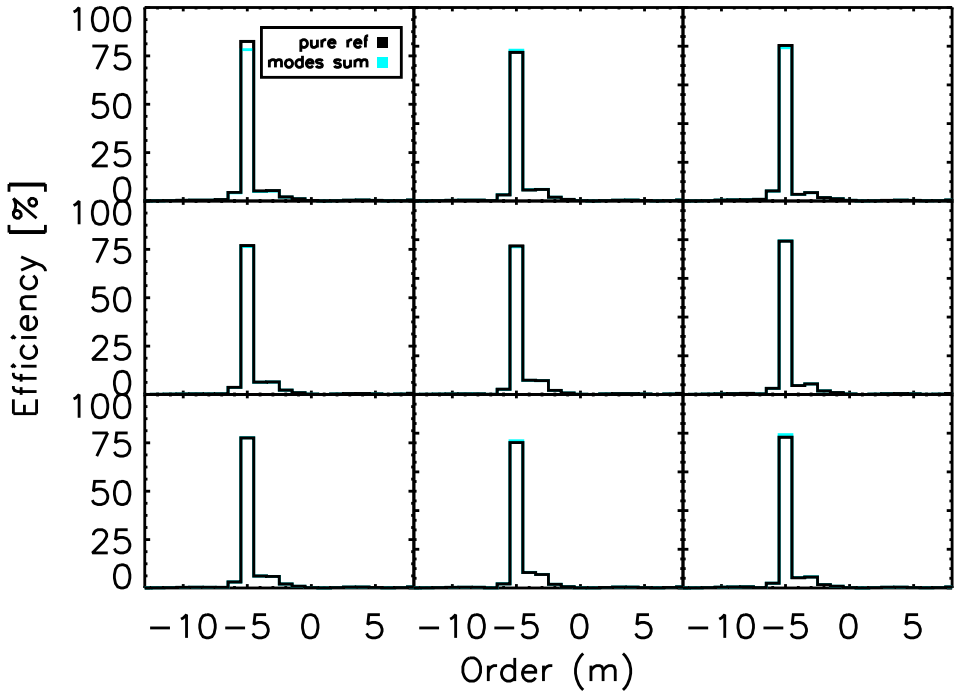

Figure 3.15 Efficiency of G3 by Bach Research with respect to the pure reflection (black) and with respect to the order sum (cyan) measured at -13 ≤ m ≤ 8.

After G3 was installed and its on-sky performance was confirmed through engineering observations, G2 was shipped to Dunlap, and its efficiency was measured using the same setup used for G3. Table 3.4 summarizes the peak efficiency at nine locations, and Figure 3.16 is the result of full efficiency measurements of G2. On average, G2 has a weighted efficiency of 39.5 ± 0.8 % with respect to the pure reflection and 35.8 ± 0.7 % with respect to the order sum.

On average, G3 has a factor of about two greater efficiency at 1310 μm. We also find that G3 has a close-to-uniform efficiency across the surface compared to G2. The field-dependent standard deviation of G3 peak efficiencies is 2.23 % whereas the field-dependent standard deviation of G2 is 11.68 %.

3.4.4 Measurement Uncertainties

To estimate the uncertainties in the efficiency measurement, we incorporate the configuration uncertainty of 1% and flat fielding uncertainty of 2.4 % (§3.4.2), random camera noise of ~ 10 DN (§3.4.1), flux fluctuation due to PCB temperature of 0.3 % (§3.4.1) and laser stability of 3.5% (§3.4.1). We also estimate the random observational error by calculating the pixel-wise standard deviation of the mean using 100 science frames and 100 dark frames per order. The random observational error is very small (<0.02 %) for all cases.

To confirm the repeatability of our measurements and the estimate of the error, we measured G2 efficiency at two locations, top-left and top-center, (see Figure 3.13 for the location) twice, the second measurement after about two weeks later than the first measurement. The peak efficiency ratio of the first time to the second time is 0.982 (pure reflection) and 0.995 (order sum) for the top-left location, and 1.005 (pure reflection) and 1.011 (order sum)

Table 3.4. G2 Peak Efficiency at 1.310 μm

Location	Left	Center	Right
Top	64.6 ± 4.0 %	30.6 ± 1.9 %	31.1 ± 1.9 %
	59.5 ± 3.4 %	28.7 ± 1.5 %	29.4 ± 1.5 %
	1.09	1.06	1.06
Center	54.8 ± 3.4 %	50.6 ± 3.1 %	34.9 ± 2.2 %
	45.3 ± 2.8 %	41.5 ± 2.6 %	32.9 ± 1.7 %
	1.21	1.22	1.06
Bottom	49.9 ± 3.1 %	47.0 ± 2.9 %	37.9 ± 2.3 %
	46.3 ± 2.5 %	43.4 ± 2.3 %	35.9 ± 1.8 %
	1.08	1.08	1.06

NOTE At each location, there are three values. The first one is the efficiency with respect to the pure reflection, the second one is the efficiency with respect to the order sum, and the last one is the ratio of the order sum to the pure reflection. All values are shown with the associated measurement errors.

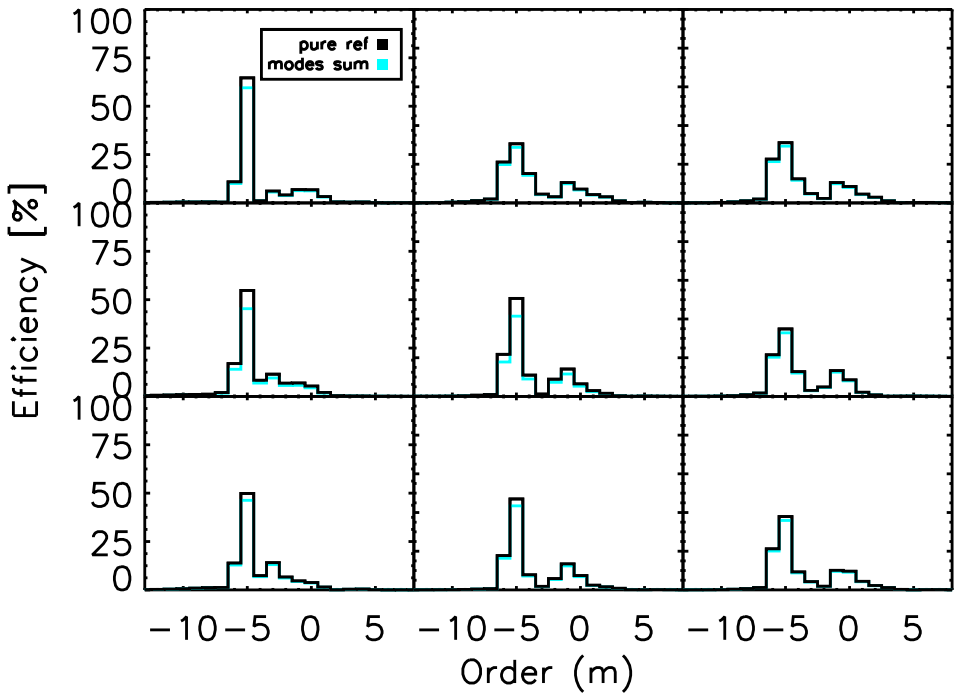

Figure 3.16 Efficiency of G2 by Diffraction Products with respect to the pure reflection (black) and with respect to the order sum (cyan) measured at -13 ≤ m ≤ 8.

for the top-center location. They are both within the measurement uncertainties.

3.4.5 Polarization Effect on Grating

The polarization state of the incident light can affect the efficiency of a diffraction grating in many cases. To understand the polarization dependence on the OSIRIS grating efficiency, we modelled the TE (polarized parallel to the groove) and TM (polarized perpendicular to the groove) efficiencies of the OSIRIS grating using RCWA. The RCWA model predicts that the peak TE to TM efficiency ratio for a 1.310 μm monochromatic light source at $m = -5$ is 1.041.

We conducted the polarized efficiency measurement experiments on the test ruling three times using: (1) the IR laser diode (no polarizer); (2) the IR laser diode in TE mode defined by the polarizer; and (3) the IR laser diode in TM mode defined by the polarizer. During the measurement, all the components, especially the fiber was fixed to keep the same polarization state throughout. Figure 3.17 shows these results where the total efficiency is defined either by the pure reflection (left) or the order sum (right). The peak TE to TM efficiency ratio at $m = -5$

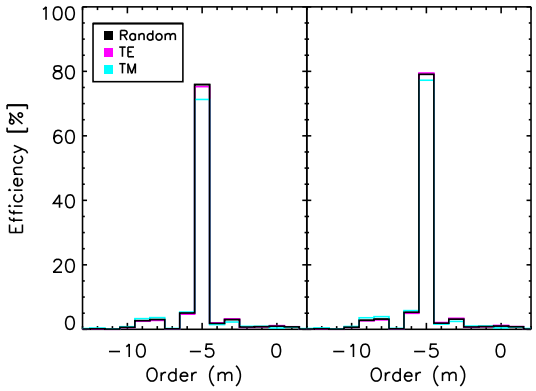

Figure 3.17 Efficiency of the test ruling made by Bach Research with respect to the pure reflection (left) and with respect to the order sum (right) measured (-13 $\leq m \leq$ 2) using TE/TM modes (magenta/cyan) and no polarizer (black).

is 1.056 ± 0.092 and 1.029 ± 0.074 for the pure reflection and the order sum, respectively. These measurements are in agreement with the theoretical predictions.

We confirmed that the polarization state of the laser does not change during the full efficiency measurement at one spatial location (§3.4.2 and Appendix 3.4.1), and thus individual orders and the pure reflection are measured with the same polarization. As the efficiency is calculated with respect to the pure reflection or the order sum, we do not take into account the effect of the polarization in the measurement uncertainty calculation. Between different spatial locations, maximum of 4% difference in efficiency due to TE and TM states can theoretically occur. This polarization effect can also affect the real scientific observation at OSIRIS; however, it is probably insignificant since other noise components, such as sky lines, would be the dominant source of uncertainty.

3.5 New Grating Installation and Commissioning

OSIRIS was slowly warmed up to ambient temperature over a one week period, and G3 installation was performed in December 2012 by our team. Figure 3.18 on the left shows our team at the Nasmyth platform of Keck-I. The

black dewar in the back is the AO bench, and the green dewar on the right is the OSIRIS cooling enclosure. G2

Figure 3.18 Left: OSIRIS team at the Nasmyth platform of Keck-I. The black dewar in the back is the Keck-I AO bench, and the green dewar on the right is the OSIRIS cooling enclosure. Right: Grating alignment with respect to the mounting plate in the lab at the Keck Observatory summit.

was removed from OSIRIS, and its alignment was measured and marked with respect to the mounting plate in the lab at the Keck Observatory summit facility (right panel of Figure 3.18). G2 was detached from the mounting plate, and G3 was aligned to the marks and installed on the mounting plate.

Figure 3.19 shows a HeNe laser at 632.8 nm being diffracted by G2 (top) and G3 (bottom) in the Keck summit lab prior to the installation of G3 in OSIRIS. The light is visibly more concentrated to one order for G3 while a higher fraction of light is diffracted to multiple orders by G2.

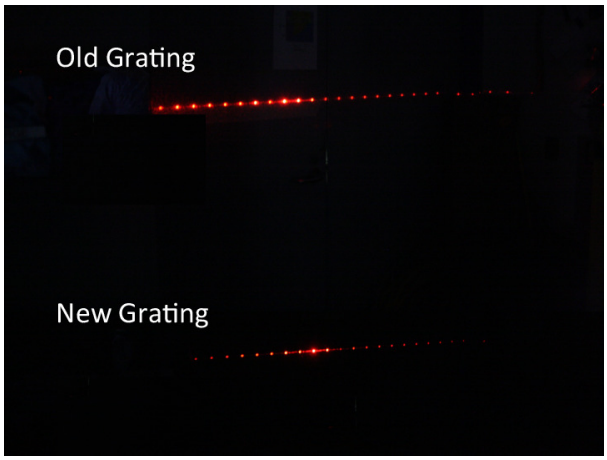

Figure 3.19 Diffraction of a HeNe laser at 632.8 nm using G2 (top) and G3 (bottom). Test performed in December 2012. The light is more concentrated in one order for G3 whereas high fraction of light is diffracted in multiple orders for G2.

On January 20 and 27, 2013, OSIRIS with G3 was commissioned on-sky using the Keck-I AO system. Both nights started with clear night, but unfortunately, within one or two hours, the weather conditions changed to thin/high cirrus with high wind. Some standard stars and blank sky were observed with the deformable mirror off. The resulting measurements are certainly affected by the varying weather conditions. The measurements of OSIRIS sensitivity with G3 in each spectrograph filter from these nights, as well as prior measurements with G2 are reported in §3.6.

Table 3.5. Zero Point Vega Magnitude and Factor of Improvement from G2 to G3

Filter	*Zbb*	*Jbb*	*Hbb*	*Kcb*	*Kbb*
λ_{cen} [μm]	1.090	1.325	1.637	2.174	2.174
G2 at Keck-II	23.70	23.80	24.45	23.19	23.67
G3 at Keck-I	24.19	24.22	24.84	24.16	24.54
Improvement	1.56	1.48	1.43	2.45	2.23

3.6 On Sky Performance and Throughput

In this section, we compare on-sky performance between G2 and G3. Our comparison is complicated by the fact that in early 2012 OSIRIS was moved from Keck-II to Keck-I to be the first dedicated science instrument for a new Laser Guide Star (LGS) AO capability on Keck-I that was installed in 2010. The LGS system on Keck-I uses a significantly improved laser system compared to the existing Keck-II laser system (Chin et al., 2010).

The final zero point magnitude at all broadband filters for OSIRIS are calculated using standard star observations. The data used to calculate G2 zero points were all taken on Keck-II, and G3 data were all taken on Keck-I. Although there are differences in throughput between the two telescopes and AO systems as well as differing weather condition between our limited observations, there is a general zero point improvement for G3 in comparison to G2.

We use as many standard star observations as we had access to, but the number of observations is fairly small in each particular band. For OSIRIS with G2 on Keck-II, HD105601, HD106965, HD201941, and HD18881 taken between April 2007 and January 2012 are used, and for OSIRIS with G3 on Keck-I, HD44612 and HD18881 observed on January 20 and 27, 2013 are used. The zero points are calculated by applying a large rectangular aperture on raw (non-reduced) image, over the entire spectrum. In all cases, approximately equal rectangles are used for the wavelength ranges. The resulting zero point magnitude and the factors of improvement are shown in Table 3.5.

3.7 Pipeline Modification

One unique aspect of OSIRIS is that over 3000 spectra are all partially overlapped on the detector at staggered wavelength, and hence special reduction and calibration steps are required. The OSIRIS Data Reduction Pipeline (DRP) reduces the science data to the level where a user can begin their custom scientific analysis. After OSIRIS was moved to Keck-I, and G3 was installed, the DRP had to be modified to account for the new AO system and the new grating.

On Keck-I, the AO system optical path to OSIRIS has one less mirror than the Keck-II system. This produces a flipping of image in the y-direction. This axis flip is fixed in the DPR "Assemble Data Cubes" module. The Keck-I AO system uses a different IR/visible splitting dichroic from that used on Keck-II, and white light measurements using the AO fiber calibration source showed that the Keck-I AO system dichroic produces essentially no instrumental dispersion. The "Correct Dispersion" module in the DRP that corrects for atmospheric dispersion and instrumental dispersion was appropriately modified for the Keck-I AO path.

We determined a new wavelength solution using arc lamp and OH lines in each broadband filter, and we found about four spectral channels of shift from the previous (G2) version. The field dependent wavelength solution per

spaxel was calculated using the cross correlation of OH lines using the Kn3 filter with the 35mas spaxel scale. Figure 3.20 shows relative/absolute pixel and wavelength offsets in angstroms between 2006 with G2 (top) and 2013 with G3 (bottom). It is a residual offsets after using the "Assemble Data Cubes" and a new wavelength

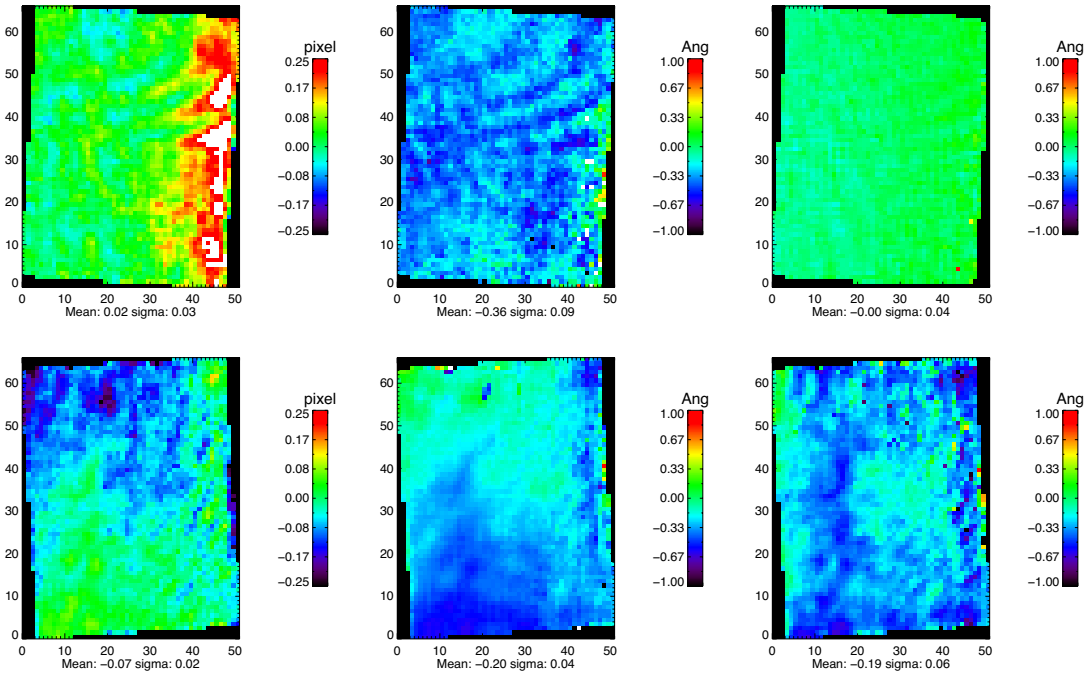

Figure 3.20 Uncorrected relative pixel shift (left), uncorrected absolute wavelength offsets in angstroms (middle), and corrected absolute wavelength shift in angstroms (right) for Kn3 35 mas in 2006 with G2 (top) and in 2013 with G3 (bottom).

solution. The comparison of two confirms that the quality of the ruling on the new grating is more uniform across the surface. The field dependent and global wavelength solution is now implemented in the new pipeline.

A problem had been observed prior to commissioning of G3 that affected the lower right quadrant of the reduced data cube with varying shifts in measured intensity and shifts in the detector channel offsets. During the modification of the DRP, we found that there appeared to be a bad column on the detector, and this was biasing the wavelength solution. This problem started on September 17, 2011 when one of the spectrograph Hawaii-II detector Leach-ARC detector read-out video boards was swapped. In the end, it is just one pixel shift that skews the timing of the entire channel. This channel offset is now fixed in the new pipeline within the "Subtract Frame" module.

All these modifications are implemented in the new version of the DRP, and the DRP full package is now available to download at the OSIRIS instrument webpage[2].

3.8 Conclusion

OSIRIS at W. M. Keck Observatory is a particularly unique IFS instrument among other IFSs with AO capability today in use of a single fixed exceptionally coarse ruling (27.93 grooves per mm) diffraction grating, which uses $m = -3$, -4, -5, and -6 to cover K, H, J, and Z bands. While OSIRIS has delivered a number of important

[2]http://www2.keck.hawaii.edu/inst/osiris/

scientific results, its sensitivity was limited by the performance of its spectrograph grating. Our team has worked with a new grating vendor, Bach Research Corporation, to produce a better quality grating for OSIRIS.

Bach Research manufactured a test ruling and the new grating (G3) in 2012, and we have carefully measured the direct efficiencies of both at 1.310 μm in the lab. The weighted field-averaged peak efficiency of G3 is 78.0 ± 1.6 % (pure reflection) and 77.8 % (order sum) (see footnotes in Table 3.3) with a field standard deviation 2.23 % (pure reflection) and 1.32 % (order sum). After the G3 efficiency was confirmed to be high and close to uniform over the surface, G3 was installed to OSIRIS in December 2012. G2 was shipped to Dunlap after G3 performance was tested and confirmed on-sky in January 2013. G2 efficiency was as well measured using the same lab setup used for the G3 measurement. For G2, the weighted field-averaged peak efficiency is 39.5 ± 0.8 % (pure reflection) and 35.8 ± 0.7 % (order sum) with a field standard deviation is 11.68 % (pure reflection) and 9.82 % (order sum).

The new OSIRIS grating gives a factor of about two times increase in average efficiency at 1.310 μm with less field-dependent efficiency change across the surface. The final sensitivity improvement was difficult to assess because OSIRIS was moved from Keck-II to Keck-I in early 2012; however, we were able to determine the zero point magnitudes and factors of improvement for each broadband filter. On average, on-sky throughput is 1.83 times better than when it was at Keck-II with G2. This enables us to observe fainter objects and to use observing time more efficiently.

A single fixed diffraction grating with a coarse ruling can reach high efficiency and perform well on OSIRIS, but it is very difficult to fabricate such a grating today. For the next generations of IFS instrumentation, the more usual approach of using finer ruling grating with $m = 1$ order would have less risk and would be cheaper. For example, IRIS on TMT, an IFS with some characteristics and design elements similar to OSIRIS, will instead have several gratings with finer groove densities of $\sim$ 150 to 900 per mm (Moore et al., 2010; Larkin et al., 2010).

Acknowledgements

We particularly want to thank the Bach Research Corporation for all of their efforts and support during the selection and fabrication of the OSIRIS grating. We enjoyed working with the Bach Research Corp. team during this entire process. We also thank the Keck Observatory staff who helped with the planning and installation work for the new grating in OSIRIS. We would also like to thank the referee for their thorough read and valuable suggestions. The new OSIRIS grating was graciously funded by the Dunlap Institute for Astronomy & Astrophysics at University of Toronto. Funding for this project was also provided by the NSERC Discovery grant (RGPIN 419376) and the Canada Foundation for Innovation grant (31773). Our on-sky data presented herein were obtained at the W.M. Keck Observatory, which is operated as a scientific partnership among the California Institute of Technology, the University of California, and the National Aeronautics and Space Administration. The Observatory was made possible by the generous financial support of the W.M. Keck Foundation. The authors wish to recognize and acknowledge the very significant cultural role and reverence that the summit of Mauna Kea has always had within the indigenous Hawaiian community. We are most fortunate to have the opportunity to conduct observations from this mountain.

Chapter 4

IROCKS: Kinematics of $z \sim 1$ star-forming galaxies

4.1 Chapter Outline

We present the first IROCKS (Intermediate Redshift OSIRIS Chemo-Kinematic Survey) results for sixteen z ∼1 (and one z ∼1.4) star-forming galaxies. All galaxies were observed with an integral field spectrograph, OSIRIS, equipped with laser guide star adaptive optics at the Keck Observatory. Our $z \sim 1$ sample spans a redshift range of $0.79 \leq z \leq 1.03$ ($< z > = 0.93$) and a stellar mass range of $9.6 \leq \log(M_*/M_\odot) \leq 11.2$ ($< \log(M_*/M_\odot) > = 10.4$). We use rest-frame optical nebular Hα lines to trace the morphologies and kinematics of ionized gas in $z \sim 1$ star-forming galaxies that are spatially resolved at sub-kiloparsec scales. After separating galaxies into sub-components with unique redshifts using integrated 1D spectra, we find all components to have line-of-sight velocity dispersions $\gtrsim 50$ km/s. Four galaxies in the sample are well-fitted with an inclined disk model. We investigate individual clumps in each galaxy, and are able to resolve a total of 26 clumps whose sizes are $r_{1/2} \gtrsim 0.5$ kpc in the entire sample. In this Chapter, I outline the overall survey approach, target sample, resolved kinematics of the system, and individual clumps in each galaxy.

4.2 Introduction

Over the past decade, it has become clear that "feedback" from star formation and AGN plays a crucial, but poorly understood, role in regulating the growth of galaxies over a wide range of mass scales (e.g., Governato et al., 2007; Hopkins et al., 2012; Wurster & Thacker, 2013; Agertz et al., 2013). Directly observing feedback to quench star formation is challenging at high redshift since high signal-to-noise observations are needed to register outflows and energetics in the interstellar medium. However, high velocity dispersions observed in high redshift galaxies are suggestive of feedback and may imply large turbulence, which may be driven by radiation pressure (e.g., Murray et al., 2010), cold flow (e.g., Genel et al., 2010), and/or supernovae (Joung & Mac Low, 2006). While we are rapidly compiling values for the global parameters (e.g., luminosity, color, star formation rate, gas and dust content, and stellar mass) of high redshift galaxies, there is still a gap in our knowledge of the processes that regulate galaxy growth and evolution even at modest redshifts of $z \sim 1$ to 2. This is an extremely important epoch in the lives of normal galaxies, mirrored in the precipitous drop in the cosmic star formation rate density

below $z \sim 2$.

Ground-breaking observations with integral field spectrographs (IFSs) coupled to adaptive optics (AO) (e.g., OSIRIS at Keck and SINFONI at VLT) have probed the dynamical processes of individual high-redshift (z >1.5) star-forming galaxies on kiloparsec scales (see review by Glazebrook, 2013). IFS studies at z $\sim$ 2 have shown mounting evidence that a large fraction (between 1/3 and 1/2) of high-z star-forming galaxies (>10 $M_\odot$ yr^{-1}) are in rotating disk systems with large kiloparsec-scale clumps of star formation (Förster Schreiber et al., 2011a,b), while the rest are irregular or interacting. In general, the velocity dispersions seen in the gas of early disk candidates are much higher than expected and may imply strong feedback in the form of energy being injected into the interstellar gas (Newman et al., 2014). However, IFS+AO observations of $z \sim 1.5$ galaxies have found systems with lower star formation rates which are consistent with rotationally stable disks with lower intrinsic velocity dispersions (e.g., Wright et al., 2009; Wisnioski et al., 2011), which may indicate an evolution in the settling of disks. Seeing-limited slit-based spectroscopic observations have also shown that most galaxies have large V/σ values at $z \sim 1$ while only a small fraction of galaxies have high V/σ values at $z \sim 2$, implying a rapid evolution of disks in this 5 Gyr period. These lower redshift seeing-limited slit-based spectroscopic studies are excellent for investigating global trends, but they struggle to accurately probe galactic dynamics, since observations are limited by slit orientation and seeing (typically comparable to the size of the galaxy).

With the addition of slitless grism observations using WFC3, the true sizes of the star- forming regions in $z \sim 1$ galaxies have been measured, and indeed there seems to be a population of disk galaxies with very large Hα sizes and fluxes. This indicates a large variation in the Hα sizes within the population (half light radii of 1-15 kpc; Nelson et al., 2012, 2013; Wuyts et al., 2012; Lang et al., 2014). The CANDELS 3D survey has also shown that the optical continuum emission corresponds spatially to the resolved Hα emission, implying a resolved main sequence of star formation. Clearly, investigating $z \sim 1$ star-forming galaxies are prime candidates for high angular resolution and moderate spectral resolution resolved studies, as they seem to be in a stage of building both their bulges and their stellar disks.

In 2010, a new, powerful, and center-launching laser guide star (LGS) AO was installed on Keck-I (Chin et al., 2010, 2012). In 2012, our team successfully installed a new grating on OSIRIS and increased its sensitivity by a factor of 1.5 to 2 (Chapter 3). With these factors combined, we are now capable of observing $z \sim 1$ galaxies with an IFS + AO. The selection of targets are still limited by available tip-tilt stars, but this criterion does not bias our sample selection. In this chapter, we present the first result of the Intermediate Redshift OSIRIS Chemo-Kinematic Survey (IROCKS), an AO enhanced IFS study of $z \sim 1$ star-forming galaxy using OSIRIS at the Keck-I telescope. We focus on the kinematics and morphological properties of our sample, traced by Hα emission.

This chapter is organized as follows. In Section 4.3, we detail our sample selection, OSIRIS observations, and data reduction. We present our morphology, kinematics, and disk fitting results in Sections 4.4, 4.5, and 4.6, respectively. Gas and dynamical mass estimates are described in Section 4.7. In Section 4.8, we introduce our definition of clumps, and describe their properties. Finally, we summarize our survey in Section 4.9.

Throughout this chapter, we adopt a the concurrent cosmology with $\Omega_m = 0.306$, $\Omega_\Lambda = 0.692$, and $H_0 = 67.8$ km/s/Mpc (Planck Collaboration et al., 2014). With this cosmology, 1" is $\sim$ 8.2 kpc at z = 1. For comparisons with other cosmologies used in other IFS high redshift galaxy studies, comoving distances are different from the Planck cosmology by <3%.

4.3 Observation and data reduction

4.3.1 Sample selection

We select $z \sim 1$ galaxies in several well-studied fields using four surveys: the Team Keck Treasury Redshift Survey (TKRS) in the Great Observatories Origins Deep Survey (GOODS)-North; the European Southern Observatory-GOODS (ESO-GOODS) spectroscopic program in GOODS-South; DEEP2 (RA = 02h, 14h, and 23h); and the Cosmic Assembly Near-infrared Deep Extragalactic Legacy Survey (CANDELS)-Ultra Deep Survey (UDS). We target rest-frame Hα and [NII] emission lines in J-band, which corresponds to a redshift range of 0.8 to 1.1. We also target a few $z \sim 1.5$ galaxies, which are specified by Hα in H-band (1.2 <z <1.8). Objects are ranked in observational priority based on several criteria: 1) the galaxy must have an accurate spectroscopic redshift; 2) the target's shifted Hα line must be located in regions of the J/H-band free from strong OH sky emission lines; 3) filter and atmosphere transmissions need to be high ($\gtrsim$0.7); 4) there must be a nearby tip-tilt (TT) star with an R-band magnitude below 17 mag within 50" from the galaxy; and 5) a higher inferred Hα flux, and hence star formation rate (SFR), is preferred. To estimate SFR, we infer Hα spectroscopic flux from previous Hβ or [OII] detections. For recombination-B star formation, intrinsic flux ratios are estimated as Hα/Hβ= 2.8, and Hα/[OII] = 1.77 (Osterbrock, 1989; Mouhcine et al., 2005), not including extinction. Using these relations, we infer the Hα fluxes for objects in the TKRS (Hβ for $z \sim 1$ and [OII] for $z \sim 1.5$ sources), ESO-GOODS ([OII]), and DEEP2 ([OII]) fields. Objects in the UDS field do not have Hβ or [OII] measurements; therefore, we instead use their K-band magnitudes, which has been shown to correlate with SFR (Reddy et al., 2005; Erb et al., 2006a), to rank those objects. Lastly, we prioritized sources that have complementary Hubble Space Telescope (HST) imaging, since it provides accurate offsets between the galaxies and their tip-tilt (TT) stars, and can aid in morphological comparisons between UV and optical line emissions. There are two fields, DEEP2 2d and 23d, that do not have HST imaging available, but these fields are still desirable since they contain key spectroscopic information along with seeing-limited imaging from the Canada France Hawaii Telescope (CFHT) and Sloan Digital Sky Survey (SDSS).

TKRS sample

TKRS (Wirth et al., 2004) is a deep spectroscopic survey in GOODS-North undertaken with a visible, multi-slit spectrograph, the DEep Imaging Multi-Object Spectrograph (DEIMOS; Faber et al., 2003), on the Keck II telescope. It provides accurate redshift measurements of more than 1500 magnitude-limited objects to R_{AB} = 24.4 mag. To estimate Hα fluxes, we use Hβ and [OII] emission line fluxes for $z \sim 1$ and $z \sim 1.5$ galaxies, respectively. The GOODS-North field has a wealth of optical HST imaging data available, particularly in rest-frame UV, but also in wide J-band (F125W). We use HST images to choose galaxies that are not too diffuse nor unresolved to increase expected signal detection. We observed nine $z \sim 1$ and two $z \sim 1.5$ sources from TKRS and successfully detected three $z \sim 1$ (7187, 9727, and 7615) and one $z \sim 1.4$ (11169) sources (Table 4.1). 11169 is the only $z \sim 1.5$ source in our sample.

ESO-GOODS sample

We select our GOODS-South targets from the spectroscopic campaign of Vanzella et al. (2008). The data was taken by the UV FOcal Reducer and low dispersion Spectrograph (FORS2; Appenzeller et al., 1998) on UT2 at VLT. Their spectroscopic sample was selected by photometric colors and redshifts. The final ESO-GOODS catalog provides more than 850 redshift measurements. We use [OII] fluxes to estimate SFR and Hα fluxes for

these $z \sim 1$ galaxies. In the GOODS-South field, HST optical observations are available, and we use them to eliminate diffuse sources. We observe and detect only one source, J033249.73, in ESO-G (Table 4.1).

DEEP2 sample

DEEP2 is a redshift survey to study the universe at $z \sim 1$ (Newman et al., 2013a, and references therein) . The observations were done by the visible wavelength Low Resolution Imaging Spectrograph (LRIS; Oke et al., 1995; Rockosi et al., 2010) at Keck-I and DEIMOS at Keck-II. It provides more than 38,000 reliable redshift measurements. We select sources in 02h (SDSS deep strip), 14h (EGS – Extended Groth Strip), and 23h (SDSS deep strip) and use [OII] fluxes to estimate Hα fluxes. Multiple optical HST data are available for the EGS field, but not the 02h and 23h fields. We eliminate diffuse sources from EGS using HST images, but sources in 02h and 23h fields are only selected from their expected Hα flux. We observe six sources in EGS, four in 23h, and two in 02h field, and detecte five (11026194, 12008898, 12019627, 13017973, 13043023) in EGS, all four (32040603, 32016379, 32036760, 22009979) in 23h, and one (42042481) in 02h (Table 4.1).

UDS sample

CANDELS at UDS provides the multi-wavelength (UV to mid-IR) catalog. Among about 36,000 F160W-selected sources, 210 sources have spectroscopic redshift measurements (Galametz et al., 2013). At the time of observation, star formation rate estimates were not available, so we use existing K-magnitude measurements to prioritize our samples with predicted signal-to-noise ratios (Erb et al., 2006a). UDS field has both optical and near infrared HST imaging data, and we use them to select the most detectable sources. We observe three sources in UDS, and detect two (11655 and 10633) sources (Table 4.1).

4.3.2 OSIRIS Observations

IROCKS galaxies are observed with OSIRIS (Larkin et al., 2006) at the W. M. Keck Observatory in Mauna Kea in Jun 2012, May/Aug 2013, and May/Jun/Sep 2014. OSIRIS is a diffraction-limited IFS with a moderate spectral resolution (R $\sim$ 3800). It uses a lenslet array as the sampling element on the sky to achieve low noncommon path error (<30 nm rms). OSIRIS was originally installed at the Keck-II telescope, but it was transferred to Keck-I in early 2012 to be the first dedicated science instrument for a new laser guide star AO capability on Keck-I (Chin et al., 2010). In December 2012, the OSIRIS grating was upgraded, and the final throughput was improved by a factor of 1.83 on average between the old grating at Keck-II and the new grating at Keck-I between 1 and 2.4 μm (Chapter 3 and Mieda et al., 2014). All IROCKS observations are made after OSIRIS has been transferred to Keck-I. Only one target, DEEP2-13017973, was observed with OSIRIS before the grating upgrade.

Our observations use OSIRIS LGS-AO in the coarsest plate scale, 0.1", corresponding to $\sim$ 800 pc at $z \sim 1$, which gives the highest sensitivity to low surface brightness emission. All observations are made in one of the narrowband J and H filters (5% bandpasses) in order to observe both Hα and [NII] simultaneously. This combination of plate scale and filter width produces a field of view of roughly 4.8" $\times$ 6.4", which is sufficient to encompass the entire galaxy and support small $\sim$2" dithers between exposures on source. For each galaxy we also observe at least one pure sky pointing to ensure proper sky subtraction.

The standard observation procedure is as follows: We acquire a TT star at the optimal position angle (PA) and take a pair 30 s integrations (center and $\sim$ 1.5" offset) to check the centering and measure the PSF. Once the telescope pointing matches with the sky, we apply a blind offset and move to the target galaxy. After the AO loop is closed, we take three 900 s exposures in up, down, and center positions. Typically, the up and down positions

are separated by 2.2 arcsec. While taking the third frame, the second frame is subtracted from the first. When Hα is detected in the first frame, we stay on the target for 1.5h - 2.5h to achieve a high signal-to-noise ratio (SNR). A different dither offset is used in each exposure to avoid any bad pixel contamination. At the end of each night, we observe an Elias standard star with all filters used that night.

We successfully detect Hα in sixteen $z \sim 1$ sources and one $z \sim 1.5$ sources. Table 4.1 summarizes IROCKS observations.

4.3.3 OSIRIS Data reduction

Data reduction is performed using the OSIRIS data reduction pipeline (DRP) version 3.2 and custom IDL routines. Before we run DRP, we use our own custom IDL code to correct the rectification matrices. The rectification matrices are maps of lenslet point spread functions and are required to extract spectra by DRP. Since the upgrade of the OSIRIS grating and calibration unit, the newly taken matrices have created artificial bad pixels in the reduced cube as they iteratively extract spectra. To resolve this issue, we replace any matrix entry >0.8 with its neighbor mean. With the corrected rectification matrices, we first combine several dark frames of that night by DRP to make a master-dark. We then run DRP again to subtract the master-dark; adjust channel levels; remove crosstalk, detector glitches, and cosmic rays; extract spectra using the corrected rectification matrices; assemble data cube; and finally, correct for atmospheric dispersion. After this, we run our own cleaning code on the cube, which, for a given channel, iteratively replaces pixel values with the median of its neighboring pixels, if its original value is more than 15 σ_λ (standard deviation per channel) away from the spatial median.

After we obtain the cleaned, dark-subtracted cubes, we experiment with two sky subtraction methods, *simple subtraction* and *scale subtraction*, using both *pure sky* and *pair sky*. Pair sky is another science frame where the galaxy's location on the detector does not overlap with the current science frame. Simple subtraction, as its name implies, is a simple subtraction of a sky cube from a science cube. Scale sky subtraction, on the other hand, uses an algorithm from Davies et al. (2007) that scales OH sky emission lines between adjacent frames to reduce sky subtraction residuals. The final choice of sky and subtraction method is determined by examining the resultant standard deviation in spectral space; a lower standard deviation, (i.e., less noisy), was deemed better. Furthermore, we additionally subtract a channel-dependent constant to the sky-subtracted cube that ensures the median value in the regions away from the source is zero. We then mosaic the reduced cubes using the DRP with the "meanclip" combine method and LGS offset method. The effect of sky subtraction can be seen clearly in Figure 4.1, where the magneta line is one example spaxel from the galaxy DEEP2 12008898 before sky subtraction, and black is after. We are able to largely remove contamination from sky emission lines and recover a well-defined Hα emission line from the galaxy. In the end, an additional bad-pixel-removal algorithm is used to replace single, isolated, high-value (6 or 7 σ above the spatial median) pixels that are outside of the expected galaxy vicinity, with the spatial median of the given channel. To increase SNR, the cleaned mosaic-ed cube is spatially smoothed by a Gaussian function of FWHM = 1.5 to 3.0 pixel (0.15" to 0.3"). The smoothing FWHM is chosen by our custom "adaptive smoothing" code. The detail of this method is documented in Appendix A. Finally, flux calibration is done using the Elias telluric standard stars observed on each night.

The error, or uncertainty, in our data is defined by the spatial standard deviation within the region where all mosaiced frames are overlapped, for a given channel. Therefore our error is wavelength-dependent, and spatially invariant. The only exception is where not all frames are overlapped. There we scale the error by $\sqrt{n_{\max}/n}$, where n is the number of frames used at that spaxel, and $n_{\max}$ is the maximum number of frames used in the cube.

Table 4.1. IROCKS observations

Survey	ID	z_0[a]	RA J2000.0	Dec J2000.0	date yy/mm	t_{exp}[b]	Filter	θ_{TT}[c] ["]	R_{TT}[d]	θ_{sm}[e] [pixel]	θ_{PSF}[f] ["]
Detected											
UDS	11655	0.8960	02 16 58.0	-05 12 42.6	13/08	9	Jn2	18.0	16.0	2.0	0.24/0.49
UDS	10633	1.0300	02 17 15.6	-05 13 07.6	13/08	4	Jn3	21.4	16.5	2.0	0.23/0.48
DEEP2	42042481	0.7934	02 31 16.4	+00 43 50.6	14/11	10	Jn1	23.2	15.4	2.0	0.26/0.52
ESO-G	J033249.73	0.9810	03 32 49.7	-27 55 17.4	14/09	5	Jn3	23.6	15.5	3.0	0.24/0.52
TKRS	11169	1.43249	12 36 45.8	+62 07 54.3	13/01	6	Hn2	33.7	16.4	2.0	0.37/0.55
TKRS	7187	0.84022	12 37 20.6	+62 16 29.7	13/05	8	Jn1	48.3	14.4	2.5	0.23/0.48
TKRS	9727	0.90316	12 37 05.9	+62 11 53.6	13/05	6	Jn2	46.9	14.0	2.5	0.53/0.68
TKRS	7615	1.01268	12 37 31.1	+62 17 14.7	13/01	6	Jn3	34.3	15.4	2.5	0.48/0.68
DEEP2	11026194	0.9198	14 15 43.0	+52 09 07.6	14/06	7	Jn2	15.1	13.5	2.5	0.33/0.57
DEEP2	12008898	0.9359	14 16 55.5	+52 27 51.3	13/05	10	Jn2	20.6	16.0	1.5	0.28/0.39
DEEP2	12019627	0.9040	14 18 49.8	+52 38 08.3	13/05	9	Jn2	49.7	16.4	2.0	0.23/0.37
DEEP2	13017973	1.0303	14 20 13.1	+52 56 13.7	12/06[g]	9	Jn3	28.8	15.3	2.5	0.39/0.71
DEEP2	13043023	0.9715	14 20 15.8	+53 06 43.2	14/06	6	Jn3	35.6	13.7	2.5	0.42/0.59
DEEP2	32040603	1.0327	23 28 28.3	+00 21 55.9	14/11	5	Jn3	37.9	14.7	2.5	0.23/0.54
DEEP2	32016379	0.8335	23 29 36.6	+00 06 12.8	13/08	9	Jn1	18.8	16.8	2.0	0.27/0.42
DEEP2	32036760	0.8534	23 30 32.8	+00 20 06.9	13/08	7	Jn1	36.7	15.5	2.5	0.34/0.63
DEEP2	33009979	0.9797	23 31 56.3	-00 02 32.0	13/08	6	Jn3	41.1	13.0	2.0	0.20/0.42
Nondetection											
UDS	11557	0.9180	02 17 24.4	-05 12 52.2	14/11	4	Jn2	29.3	12.6		0.18
DEEP2	42042017	0.8070	02 28 38.0	+00 40 14.0	14/11	3	Jn1	33.1	14.2		0.14
TKRS	3447	0.83457	12 36 02.9	+62 12 01.4	12/06[g]	5	Jn1	21.3	13.6		0.26
TKRS	4512	0.84047	12 36 08.6	+62 11 24.4	14/05	3	Jn1	37.0	13.6		0.24
TKRS	9867	0.85652	12 37 09.0	+62 12 02.0	14/06	2	Jn1	31.2	14.0		0.15
TKRS	9725	1.52079	12 37 18.6	+62 13 15.1	13/05	2	Hn3	33.2	15.8		0.31
TKRS	10137	0.90890	12 37 19.6	+62 12 56.2	13/05	3	Jn2	14.5	15.8		0.31
TKRS	3811	0.87026	12 37 22.6	+62 20 46.5	13/05	3	Jn1	17.9	13.2		0.22
TKRS	7078	0.95492	12 37 40.4	+62 18 53.4	14/06	3	Jn2	19.8	12.8		0.22
DEEP2	12027936	1.0385	14 19 26.5	+52 46 09.5	13/05	3	Jn4	42.3	16.7		···

[a]Spectroscopic redshift from the original selected survey.

[b]Exposure time, multiple of 900 s.

[c]Angular separation to the tip-tilt star.

[d]R magnitude of the tip-tilt star.

[e]FWHM of spatial smoothing Gaussian in pixel unit. 1 pixel = 0.1 arcsecond.

[f]FWHM of PSF during on-axis TT star observation before/after spatial smoothing in arcsecond.

[g]Observation made before OSIRIS grating upgrade.

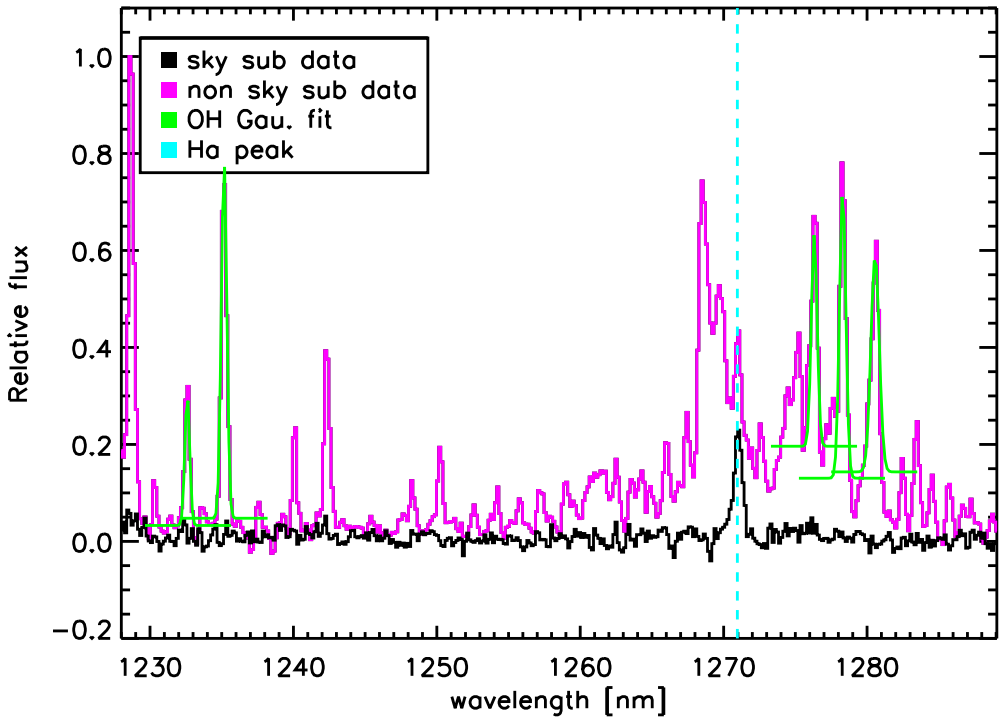

Figure 4.1 An example of unsmoothed non-sky-subtracted (magenta) and fully reduced (black) spectra at a single, bright spaxel of 12008898. The location of Hα emission line peak is shown by a cyan vertical line. Brighter OH lines that are well separated were fitted by a Gaussian profile (green) to obtain the instrumental width at that spaxel. We do not see a width trend in wavelengths, and thus we only obtain spatially but not spectrally varying instrumental width.

Table 4.2. IROCKS: Fluxes

ID	z_{sys} [a]	$f_{H\alpha}$ [b]	$f_{[NII]}$ [c]	$\log\left(\frac{[NII]}{H\alpha}\right)$
11655	0.8962	20.1 ± 5.0	4.9 ± 4.4	-0.61 ± 0.40
10633	1.0318	4.1 ± 2.3	···	···
42042481	0.7940	43.0 ± 7.8	15.2 ± 6.8	-0.45 ± 0.21
J033249.73	0.9813	10.8 ± 4.3	3.8 ± 6.1	-0.45 ± 0.71
11169E	1.4344	14.8 ± 3.4	2.3 ± 4.2	-0.80 ± 0.79
11169W	1.4330	21.5 ± 3.6	···	···
7187E	0.8404	7.1 ± 2.9	2.3 ± 4.0	-0.49 ± 0.78
7187W	0.8409	6.0 ± 2.9	1.4 ± 5.2	-0.62 ± 1.59
9727	0.9038	28.2 ± 6.2	13.3 ± 6.0	-0.33 ± 0.22
7615	1.0130	15.4 ± 5.1	3.4 ± 3.6	-0.66 ± 0.48
11026194	0.9205	14.3 ± 4.0	2.6 ± 3.5	-0.74 ± 0.59
12008898N	0.9362	5.5 ± 4.3	0.6 ± 2.4	-0.94 ± 1.68
12008898S	0.9364	55.0 ± 9.4	22.2 ± 44.2	-0.39 ± 0.87
12019627N	0.9037	8.8 ± 3.5	1.8 ± 4.4	-0.69 ± 1.08
12019627SE	0.9045	15.3 ± 4.8	···	···
12019627SW	0.9059	9.7 ± 3.5	<0.2	<-1.70
13017973	1.0309	71.8 ± 19.6	9.9 ± 16.0	-0.86 ± 0.71
13043023	0.9716	27.1 ± 8.2	7.6 ± 8.0	-0.55 ± 0.47
32040603	1.0338	10.8 ± 3.4	<0.1	<-2.04
32016379	0.8339	20.0 ± 5.2	4.7 ± 4.0	-0.62 ± 0.38
32036760	0.8519	16.7 ± 3.7	5.0 ± 2.8	-0.52 ± 0.26
33009979N	0.9817	12.0 ± 4.2	3.5 ± 4.3	-0.53 ± 0.55
33009979S	0.9799	44.2 ± 9.5	8.3 ± 6.9	-0.73 ± 0.37

[a]Redshift measured from OSIRIS Hα detected emission line.

[b]Hα emission line flux in units of 10^{-17} erg/s/cm^2.

[c][NII] line emission line flux in units of 10^{-17} erg/s/cm^2.

Hα maps

Hα flux maps are created by cross-correlating a normalized Gaussian profile of a typical Hα width with the spectrum at each spaxel to find a correlation peak. We then sum up five channels around this peak to represent Hα flux. The noise map is made by adding the error in the same 5 channels in quadrature. Since [NII] detection is significantly weaker than Hα, we do not cross-correlate our spectra to locate it. Rather, we infer its location from the detected Hα line, and calculate its flux and associated error by summing up 5 channels around that inferred offset in the spectral dimension. When the correlation peak does not coincide with the peak of Gaussian fitting (see §4.5 for Gaussian profile fitting to Hα lines), we instead use five channels around the redshift from the original surveys, z_0 (shown in Table 4.1). In this case, we consider it a non-detection, and the calculated flux reflects the background level. HST images (if available) and the resultant Hα flux maps are shown in Fig. 4.5 on the left and second left panels, respectively.

1D spectra

We define an Hα segmentation map for each galaxy using the SNR. Spaxels whose $SNR_{H\alpha}$ <3 or Gaussian fitted $SNR^{G}_{H\alpha}$ (integration of Gaussian parameters with propagated error) <1.5 are masked out. Here, we apply final visual inspection to mask out bad spaxels. The integrated 1D spectra of IROCKS samples (top panel of Fig. 4.2) are created by summing up all spaxels in the Hα segmentation map. A single Gaussian profile is fitted to the Hα emission line in each 1D spectrum to obtain the peak wavelength and integrated width. From the peak

wavelength, we measure a systematic redshift, and from the width, corrected for the instrumental resolution, the global 1D velocity dispersion, σ_{1D}, was obtained. This 1D dispersion σ_{1D} (sometimes called σ_{net} or σ_{global}; Law et al., 2009; Wisnioski et al., 2011; Wright et al., 2009) is not decoupled from the global velocity gradient and any feedback features (e.g., wider Gaussian wing). In §4.5, we discuss another velocity dispersion value, σ_{ave}, which more accurately measures the line-of-sight velocity dispersion

We note that instrumental resolution in fact varies across the field of view, and for σ_{1D}, we use a spatial average. To calculate the spatially varying instrumental width, we measure the widths of OH lines in non-sky-subtracted data (see example of OH lines in Figure 4.1). The procedure is as follows: we first smooth the non-sky-subtracted data with a Gaussian function of the same width as the one used for the science data. Using a Gaussian fit, we then measure the widths of brightest OH lines that are well separated (>5 channel) from other OH lines. This resulted in a few width measurements per spaxial in an individual sky data cube. Since the final science frame is "mosaicked" together at different dither patterns, the instrumental width per spaxel is an average of all the frames combined. We find that the typical instrumental width corresponds to ~ 45 km/s.

Multiple components in each galaxy

When there is only a single Hα peak in the spectrum, the object is classified as a single component source: 11655, 10633, 42042481, J033249.73, 9727, 7615, 11026194, 13017973, 13043023, 32040603, 32016379, and 32036760. When there are more than one peak, we spatially separate them and treat them as different components, and the galaxy is classified as a multiple Hα source: 11169 (East and West), 7187 (East and West), 12019627(North, South-East, and South-West), and 33009979 (North and South). There are two special cases: first, the spectrum of 12008898 only has one peak, but on both HST and Hα maps, its north and south components are spatially separated by $\theta \sim 2$" (~ 3 kpc), so we categorize it as multiple (North and South); and second, the west component of 7187 has more than one peak even after it has been separated from the east component, but the peaks cannot be spatially separated, and hence we treat it as a single component. Due to multiple peaks, σ_{1D} and other parameters for the west component of 7187 are not well measured.

Global fluxes and star formation rates

Like the top panels of Figure 4.2, the bottom panels are integrated spectra from the segmentation maps, where each spaxel spectrum has been shifted such that all Hα lines from the same map coincide at the same wavelength. This technique is useful for increasing the SNR of the emission lines, which is especially important for [NII] detection. We obtain the global Hα and [NII] fluxes by fitting Gaussian profiles to these shifted integrated 1D spectra, and computing the integral of the fitted Gaussian curves. We also obtain the flux uncertainties through error propagation using the errors in the fitted parameters.

To convert Hα fluxes into luminosities, we use a standard cosmological model (see §4.2), and account for extinction, assuming a spatially constant optical depth derived from stellar population models (§4.3.4). These Hα luminosities are then converted to SFR using the Kennicutt-Schmidt law (Kennicutt, 1998), modified by the initial mass function of Chabrier (2003):

$$\mathrm{SFR}\ [M_\odot/\mathrm{yr}] = \frac{L_{H\alpha}}{2.23 \times 10^{41} [\mathrm{erg/s}]}. \tag{4.1}$$

The systematic redshift, non-extinction-corrected integrated fluxes of Hα and [NII], and [NII] to Hα line ratio of each components are summarized in Table 4.2. The extinction-corrected/non-corrected Hα luminosity and SFR

are in Table 4.3. In this chapter, we report the global [NII]/Hα ratio, but not its spatial variation. We defer the discussion on spatially resolved [NII]/Hα to future work; see §5.4.

4.3.4 Stellar population modelling

We make use of publicly available photometric catalogs for each source to construct a consistent spectral energy distribution (SED) and stellar population fit. For the four TKRS galaxies in GOODS-North, we use the photometric catalog from version 4.1 3D-HST release (Skelton et al., 2014). This catalog contains 22 bands: seven HST, four Spitzer, and nine ground-based, ranging from 0.3 μm to 8.0 μm. For our single ESO-GOODS source, we use the GOODS/ISAAC final data release, version 2.0 (Retzlaff et al., 2010) for J, H, and K photometry, and GOODS/FOR2 final data release version 3.0 for $i - z$, $V - i$, and $B - V$ (Vanzella et al., 2008). For the ten DEEP2 sources in our sample, we use the extended photometry catalog of DEEP2 Galaxy Redshift Survey data release 4 (Matthews et al., 2013), containing *ugriz* photometry. For the two UDS sources, we use the CANDELS UDS Multiwavelength catalog (Galametz et al., 2013), which contains 19 bands: four HST, four Spitzer, and ten ground-based, ranging from 0.3 to 8.0 μm. For consistency, the SED fitting uses only ground-based photometry in the 0.3–2.3 μm range.

The SED fitting method used in this study is further described in Salim et al. (2007, 2009). In short, the method uses the stellar population synthesis models of Bruzual & Charlot (2003), with an exponentially declining continuous SFR with random stochastic bursts super-imposed, a range of metallicity (0.1 to 2 $Z_{\odot}$), and a Chabrier IMF. Each model is attenuated according to a two-component prescription of Charlot & Fall (2000), whose extinction curve is age-dependent and typically steeper than the Calzetti (2001) curve. The model assumes attenuation toward HII region, where young stars are embedded within dense clouds as well as the interstellar medium (ISM) in the galaxy. We use a total optical depth, τ_V, to indicate attenuation from both HII and ISM, and $\mu\tau_V$ for ISM only attenuation. The coefficient μ is determined from SED fitting, and in our sample,the average μ is ~ 0.48.

Individual values for stellar mass (M_*), τ_V, μ, and SFR ($\mathrm{SFR_{SED}}$) obtained by SED fitting are tabulated in Table 4.3. The table also contains uncorrected, ISM corrected, and HII+ISM corrected Hα luminosities ($L_{\mathrm{H}\alpha}$, $L^{0}_{\mathrm{H}\alpha}$, and $L^{00}_{\mathrm{H}\alpha}$), and the SFRs estimated from these luminosities ($\mathrm{SFR_{H}}\alpha$, $\mathrm{SFR}^{0}_{\mathrm{H}\alpha}$, and $\mathrm{SFR}^{00}_{\mathrm{H}\alpha}$). The comparison of these three versions of $\mathrm{SFR_{H}}\alpha$ with respect to $\mathrm{SFR_{SED}}$ is shown in Figure 4.3. HII+ISM corrected $\mathrm{SFR_{H}}\alpha$ best agrees with $\mathrm{SFR_{SED}}$, as shown by the black best-fit line in Figure 4.3, which has a power of 0.81, mean $\mathrm{SFR_{H}}\alpha/\mathrm{SFR_{SED}}$ = 0.86, and $\tilde{\chi}^2$= 1.24.

Figure 4.4 shows the instantaneous SFR estimated from Hα luminosity as a function of redshift. Most IFS studies of high redshift galaxies use ISM-only extinction correction (e.g., Law et al., 2009; Wright et al., 2009; Wisnioski et al., 2011; Queyrel et al., 2012), and thus we are showing ISM-only corrected SFR here. The SINS survey (Förster Schreiber et al., 2009) used $A_{V,\mathrm{neb}} = A_{V,\mathrm{SED}}/0.44$ (Calzetti, 2001) and found that extra nebular correction brings Hα- and UV-continuum-estimated SFR of z $\sim$ 2 galaxies into better agreement. This is consistent with our results. Even though extra attenuation toward HII region may be more appropriate, in this chapter, we use ISM-only extinction corrected values, unless specified, to be consistent with other IFS studies.

4.4 Morphologies

We quantify the morphologies of star-forming regions by examining the Hα maps with the same segmentation criteria in §4.3.2 applied. These maps can be seen in Figure 4.8. We measure a size scale and three morphological parameters for each galaxy. We define a radius of gyration, r_g as a size scale. It yields a typical distance for a

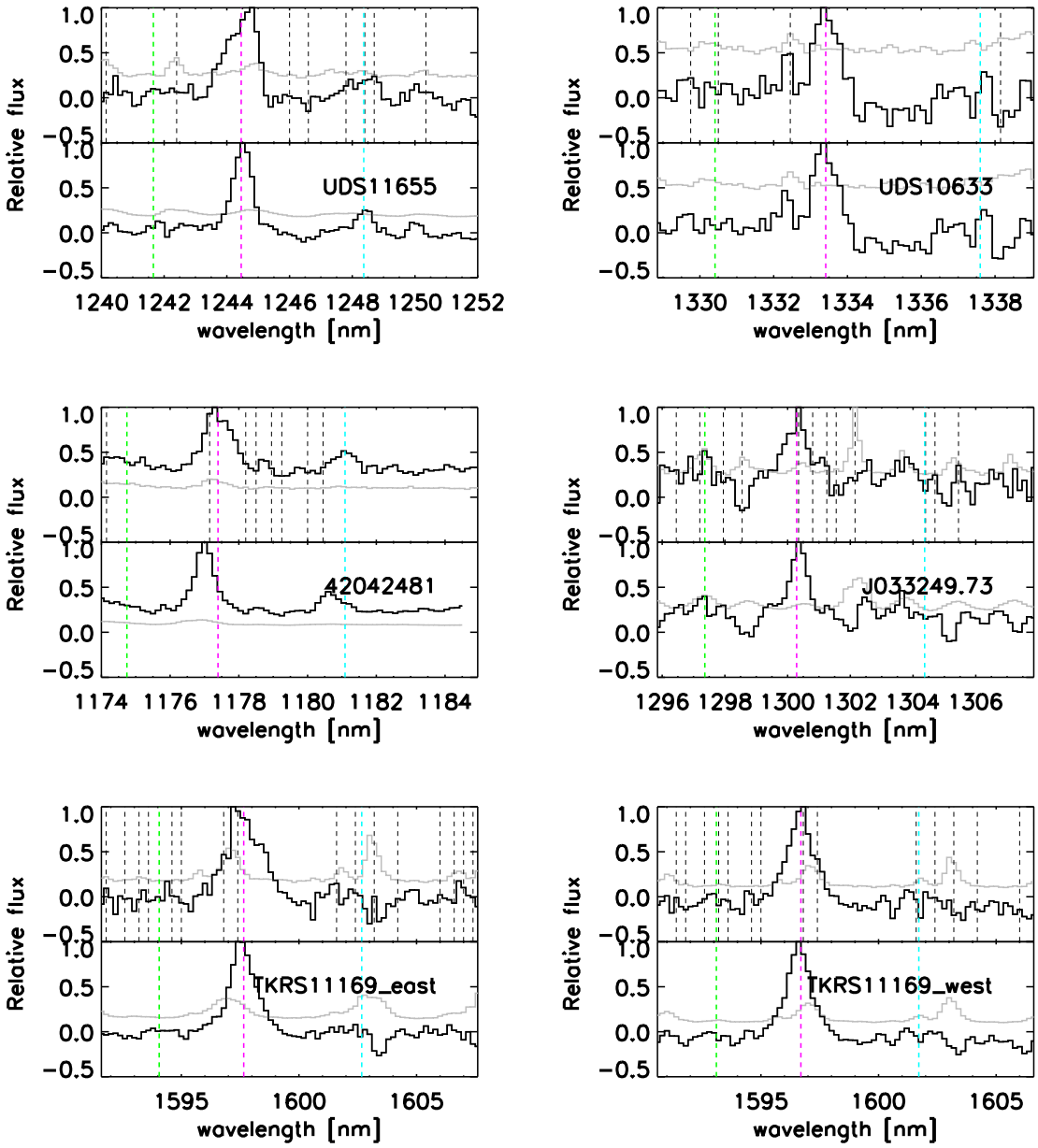

Figure 4.2 Spatially integrated 1D spectra of each component in IROCKS, ranging around Hα emission line. When the integrated spectrum has only one Hα peak, the source has only one component and is classified as a single source. When the integrated spectrum has more than one Hα peak, the source is classified as multiple, and components are spatially separated. The west component of 7187 still has more than one peaks, but different components are difficult to spatially separate, thus it is treated as one component. One σ noise is plotted in gray. The magenta dashed line is the location of Hα peak, and green and cyan lines are location of [NII]6548 and [NII]6583 calculated from Hα peak. Top: spectra in the segmentation map are summed up. Dashed black vertical lines are location of theoretical sky OH lines. Bottom: spatially integrated spectra in the segmentation map, but individual spectrum is shifted to a single redshift to increase the line signal.

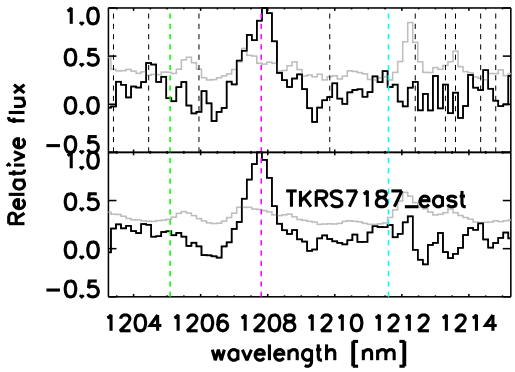
Relative flux
1.0
0.5
0.0
−0.5
TKRS7187_east
1204 1206 1208 1210 1212 1214
wavelength [nm]

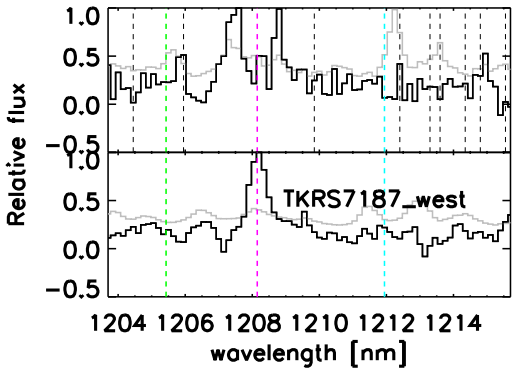
Relative flux
1.0
0.5
0.0
−0.5
TKRS7187_west
1204 1206 1208 1210 1212 1214
wavelength [nm]

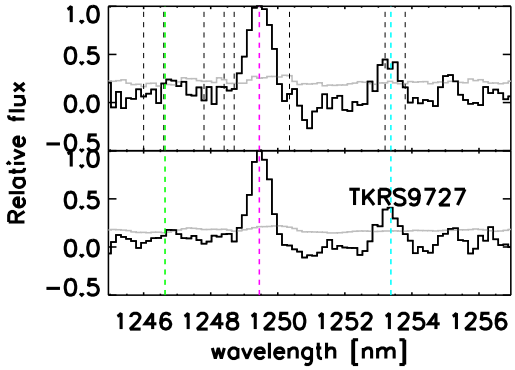
Relative flux
1.0
0.5
0.0
−0.5
TKRS9727
1246 1248 1250 1252 1254 1256
wavelength [nm]

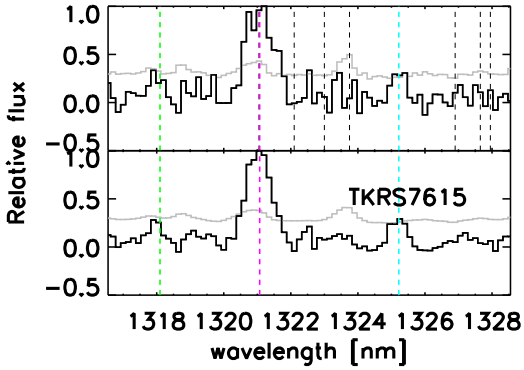
Relative flux
1.0
0.5
0.0
−0.5
TKRS7615
1318 1320 1322 1324 1326 1328
wavelength [nm]

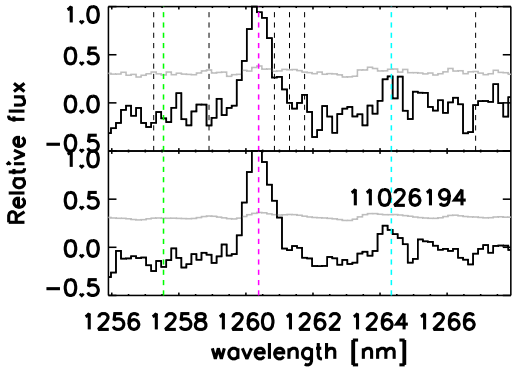
Relative flux
1.0
0.5
0.0
−0.5
11026194
1256 1258 1260 1262 1264 1266
wavelength [nm]

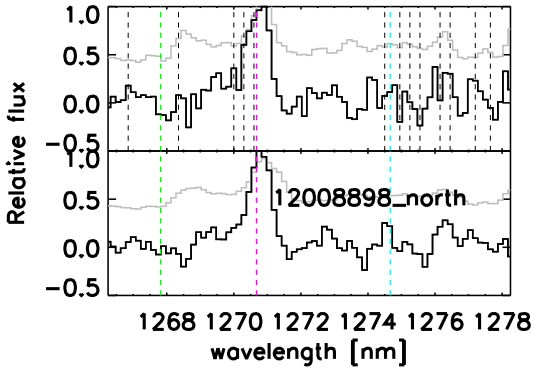
Relative flux
1.0
0.5
0.0
−0.5
12008898_north
1268 1270 1272 1274 1276 1278
wavelength [nm]

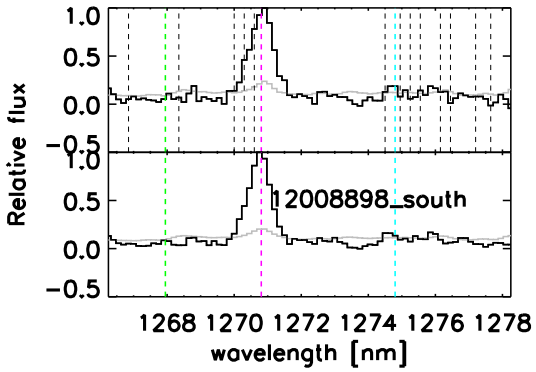
Relative flux
1.0
0.5
0.0
−0.5
12008898_south
1268 1270 1272 1274 1276 1278
wavelength [nm]

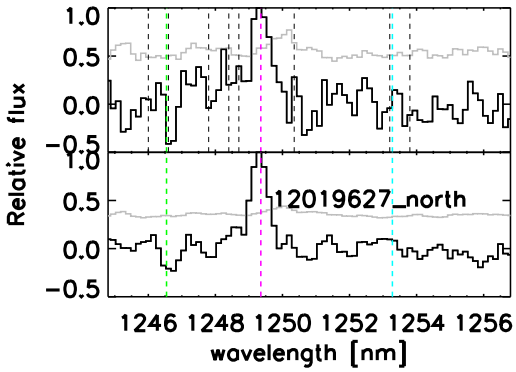
Relative flux
1.0
0.5
0.0
−0.5
12019627_north
1246 1248 1250 1252 1254 1256
wavelength [nm]

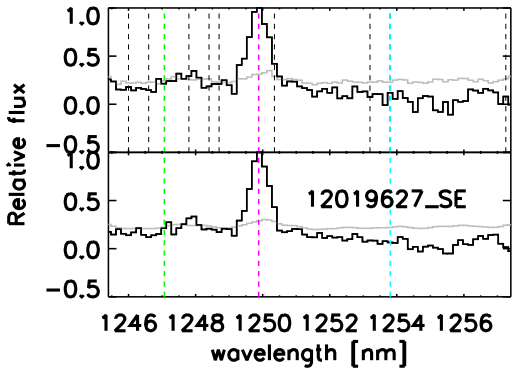
Relative flux
1.0
0.5
0.0
−0.5
12019627_SE
1246 1248 1250 1252 1254 1256
wavelength [nm]

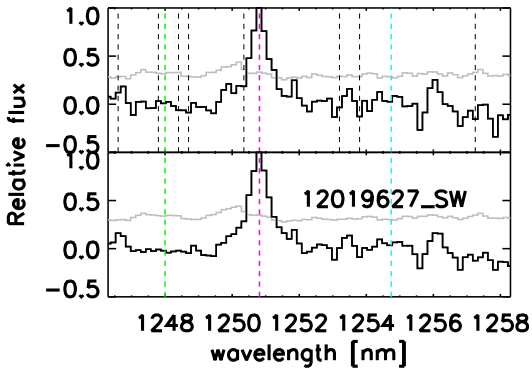
Relative flux
1.0
0.5
0.0
−0.5
12019627_SW
1248 1250 1252 1254 1256 1258
wavelength [nm]

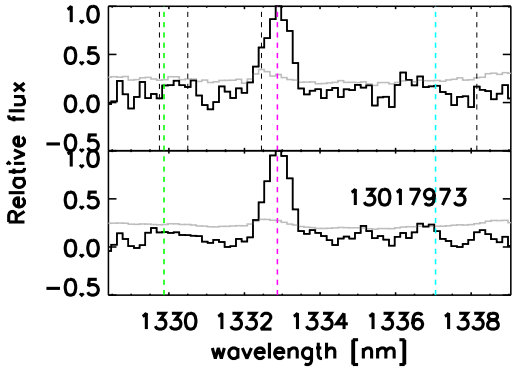
Relative flux
1.0
0.5
0.0
−0.5
13017973
1330 1332 1334 1336 1338
wavelength [nm]

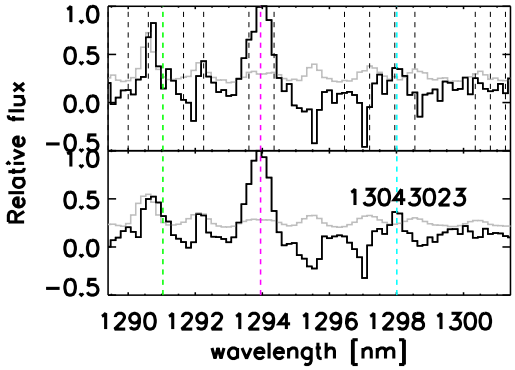
Relative flux
1.0
0.5
0.0
−0.5
13043023
1290 1292 1294 1296 1298 1300
wavelength [nm]

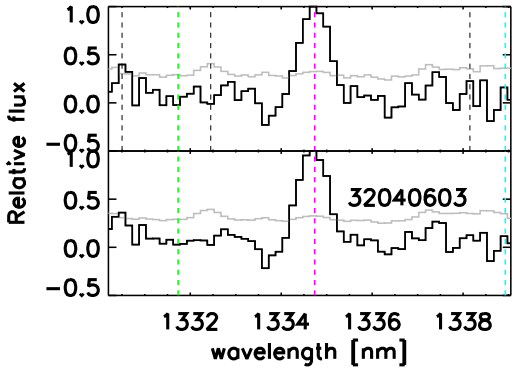
Relative flux
1.0
0.5
0.0
−0.5
32040603
1332 1334 1336 1338
wavelength [nm]

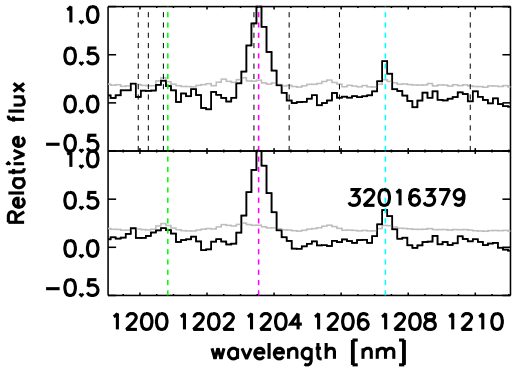
Relative flux
1.0
0.5
0.0
−0.5
32016379
1200 1202 1204 1206 1208 1210
wavelength [nm]

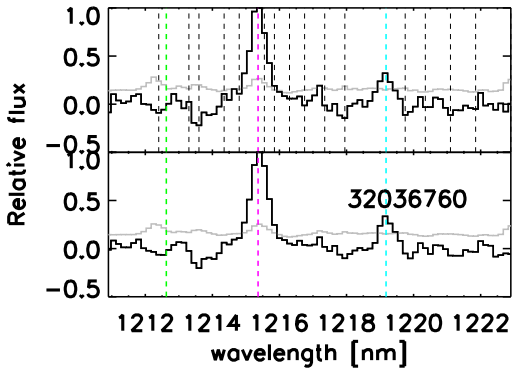
Relative flux
1.0
0.5
0.0
−0.5
32036760
1212 1214 1216 1218 1220 1222
wavelength [nm]

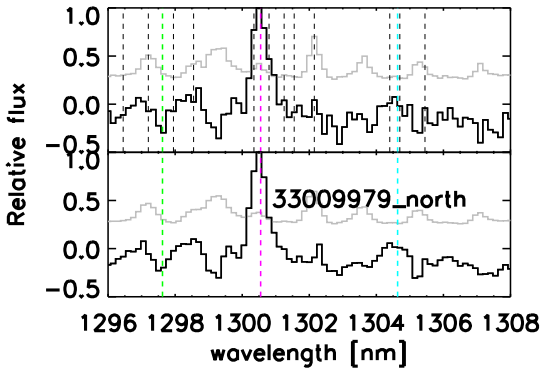
Relative flux
1.0
0.5
0.0
−0.5
33009979_north
1296 1298 1300 1302 1304 1306 1308
wavelength [nm]

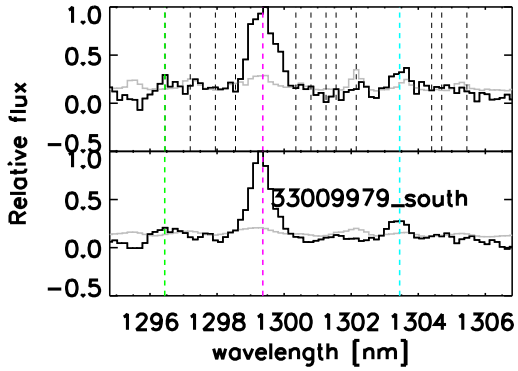

Table 4.3. IROCKS: Stellar population parameters

ID	$\log(M_*[M_\odot])$[a]	τ_V[b]	μ[c]	$L_{H\alpha}$[d] [10^{41} erg/s]	$L^0_{H\alpha}$[e] [10^{41} erg/s]	$L^{00}_{H\alpha}$[f] [10^{41} erg/s]	$SFR_{H\alpha}$[g] [$M_\odot$/yr]	$SFR^0_{H\alpha}$[h] [$M_\odot$/yr]	$SFR^{00}_{H\alpha}$[i] [$M_\odot$/yr]	SFR_{SED}[j] [$M_\odot$/yr]
11655	10.2 ± 0.1	2.07 ± 0.21	0.72	8.5 ± 2.1	28.7 ± 7.9	46.0 ± 13.8	3.8	12.9	20.6	67.6
10633	11.2 ± 0.0	3.43 ± 0.40	0.62	2.4 ± 1.3	13.9 ± 8.2	40.3 ± 25.8	1.1	6.2	18.1	39.8
42042481	10.6 ± 0.2	0.75 ± 0.48	0.42	13.5 ± 2.5	17.4 ± 4.3	24.9 ± 10.8	6.0	7.8	11.1	16.6
J033249.73	10.5 ± 0.1	0.88 ± 0.37	0.60	5.7 ± 2.3	8.8 ± 3.8	11.7 ± 5.8	2.6	3.9	5.2	4.0
11169E	10.8 ± 0.1	1.02 ± 0.84	0.21	19.9 ± 4.6	23.7 ± 6.4	45.8 ± 33.1	8.9	10.6	20.5	6.2
11169W	10.1 ± 0.0	1.06 ± 0.41	0.32	28.8 ± 4.8	38.0 ± 7.5	68.5 ± 25.6	12.9	17.0	30.7	22.9
7187	10.3 ± 0.1	1.25 ± 0.78	0.33	4.7 ± 1.5	6.6 ± 2.5	13.1 ± 9.3	2.1	3.0	5.9	7.8
7187E	···	···	···	2.5 ± 1.1	3.6 ± 1.7	7.1 ± 5.4	1.1	1.6	3.2	···
7187W	···	···	···	2.2 ± 1.0	3.0 ± 1.6	6.0 ± 4.8	1.0	1.4	2.7	···
9727	11.0 ± 0.0	3.66 ± 0.41	0.47	12.1 ± 2.7	49.5 ± 13.4	241.7 ± 96.9	5.4	22.2	108.4	158.5
7615	10.7 ± 0.1	1.29 ± 0.62	0.35	8.8 ± 2.9	12.7 ± 4.8	25.2 ± 15.3	3.9	5.7	11.3	3.8
11026194	10.2 ± 0.2	1.86 ± 0.89	0.60	6.5 ± 1.8	16.1 ± 8.3	29.5 ± 23.0	2.9	7.2	13.2	70.8
12008898N	···	···	···	2.6 ± 2.0	4.7 ± 3.9	7.0 ± 6.1	1.2	2.1	3.1	···
12008898S	9.9 ± 0.1	1.21 ± 0.49	0.60	25.8 ± 4.4	46.7 ± 13.8	69.4 ± 30.2	11.6	21.0	31.1	53.7
12019627N	···	···	···	3.8 ± 1.5	5.9 ± 2.8	9.1 ± 5.8	1.7	2.7	4.1	···
12019627S	10.0 ± 0.1	1.08 ± 0.60	0.51							32.4
12019627SE	···	···	···	0.3 ± 0.1	0.4 ± 0.2	0.7 ± 0.4	0.1	0.2	0.3	···
12019627SW	···	···	···	4.2 ± 1.5	6.6 ± 2.9	10.1 ± 6.2	1.9	2.9	4.5	···
13017973	10.6 ± 0.2	1.51 ± 0.64	0.65	42.7 ± 11.7	95.3 ± 41.5	146.8 ± 86.6	19.2	42.7	65.8	72.4
13043023	10.4 ± 0.1	1.96 ± 0.53	0.57	13.9 ± 4.2	34.8 ± 13.6	69.2 ± 36.6	6.3	15.6	31.0	85.1
32040603	9.6 ± 0.3	0.34 ± 0.37	0.37	2.0 ± 0.4	2.3 ± 0.5	2.7 ± 1.0	0.9	1.0	1.2	11.5
32016379	10.4 ± 0.2	0.71 ± 0.74	0.43	7.1 ± 1.8	9.1 ± 3.3	12.6 ± 8.3	3.2	4.1	5.7	17.0
32036760	10.7 ± 0.2	1.29 ± 0.73	0.52	6.2 ± 1.4	10.7 ± 4.1	17.8 ± 11.3	2.8	4.8	8.0	43.7
33009979N	···	···	···	6.3 ± 2.2	9.0 ± 4.1	15.0 ± 11.8	2.8	4.0	6.7	···
33009979S	10.3 ± 0.2	1.06 ± 0.86	0.41	23.2 ± 5.0	33.1 ± 11.9	55.1 ± 40.5	10.4	14.8	24.7	33.9

[a]Stellar mass.

[b]Total optical depth for HII+ISM extinction

[c]Correction to the optical depth for ISM only extinction

[d]Hα luminosity.

[e]Hα luminosity corrected for ISM only extinction.

[f]Hα luminosity corrected for HII+ISM only extinction.

[g]SFR estimated from uncorrected Hα.

[h]SFR estimated from ISM only corrected Hα.

[i]SFR estimated from HII+ISM corrected Hα.

[j]SFR estimated from SED fitting.

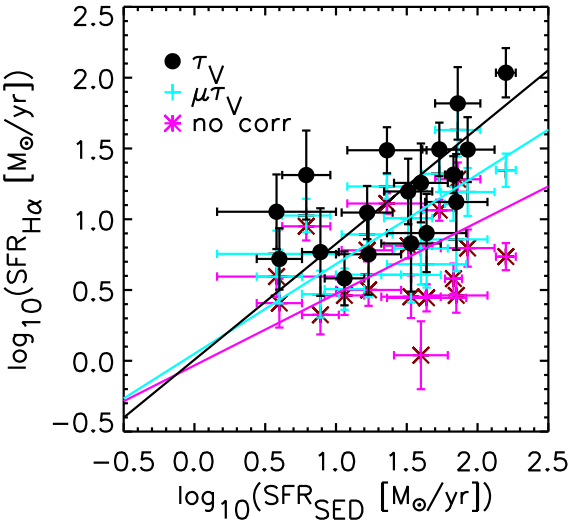

Figure 4.3 HII+ISM dust corrected ($SFR^{00}_{H\alpha}$, black circle), ISM dust only corrected ($SFR^{0}_{H\alpha}$, cyan plus), and uncorrected ($SFR_{H\alpha}$, magenta asterisk) SFR estimated from Hα luminosity using Kennicutt (1998) and Chabrier (2003) vs. SFR estimated from SED fitting. Correcting for the dust attenuation in HII region and ISM yields the best match between the derived $SFR_{H\alpha}$ and SFR_{SED}, with a best-fit line of $\log SFR_{SED} = 0.01 + 0.81 \log SFR^{00}_{H\alpha}$ and has mean $SFR^{00}_{H\alpha}/SFR_{SED} = 0.86$.

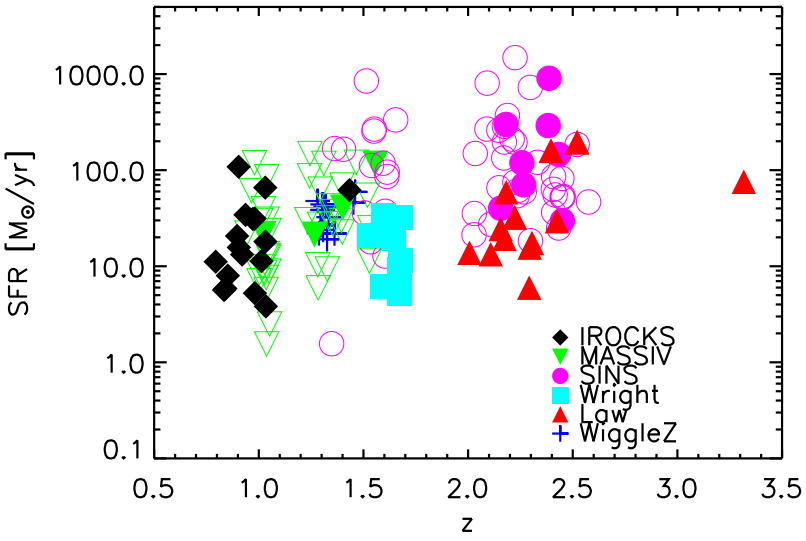

Figure 4.4 SFR of IROCKS previous high redshift IFS surveys (Wright et al., 2009; Law et al., 2009; Förster Schreiber et al., 2009; Wisnioski et al., 2011; Queyrel et al., 2012) as a function of redshift. Same symbol and color but filled/open are AO/non-AO observation. The SFRs shown here are estimated from Hα or [OIII] fluxes using Plank cosmology (see §4.2) and are corrected for ISM-only extinction.

given origin using the second moment of flux:

$$r_g = \sqrt{\frac{\sum_i d_i^2 f_i}{\sum_i f_i}}, \tag{4.2}$$

where d_i is the distance between the given origin to the i^{th} pixel whose flux value is f_i. Our choice of origin is the flux-weighted centroid. This is a mathematically robust way to define a galaxy size, especially for systems with asymmetric and clumpy flux distributions, since it does not assume a specific galaxy model (e.g., Sersic index). Since many of our Hα maps exhibit clumpy morphologies, r_g has the additional advantage of being largely insensitive to PSF and spatial smoothing, since it gives the typical distance between each clump center.

When the source has more than one distinct components (TKRS11169, DEEP2-12008898, DEEP2-12019627, and DEEP2-33009979), we also report their separation. In §4.8, we measure the individual sizes (half light radii) of clumps in galaxies. While the radius of gyration and the component separation distance describe the whole extent of the galaxy, the clump size describes the scale of local star-forming region.

We also calculate three morphological parameters for our Hα maps: the Gini coefficient (G; Abraham et al., 2003), M_{20} (Lotz et al., 2004), and multiplicity (Ψ; Law et al., 2007c). The Gini coefficient is commonly used in econometrics, and when applied to galaxy morphology, it quantifies the relative distribution of galaxy flux among its constituent pixels. M_{20} is the normalized second-order moment of the brightest 20% of the galaxy's flux, and is more sensitive to merger signatures and multiple nuclei than a concentration index. Ψ is designed to measure how multiple the source appears by measuring the projected potential energy of the light distribution, normalized by the most compact arrangement of the flux pixels. The Radii of gyration, component separations, G, M_{20}, and Ψ are listed in Table 4.4.

In our sample, the smallest source, UDS 10633, is smaller than the smoothing width and hence not resolved. However, its spectrum has good signal at the expected redshift, so we keep it in our analysis. The biggest galaxy, DEEP2 13017973, has r_g =7.6 kpc, but the most extended one is DEEP2 12019627, whose separation between the different components spans 24 kpc.

As discussed by Law et al. (2009), OSIRIS Hα morphologies are difficult to compare to high resolution rest-UV HST morphologies. IFS data typically has high background levels, and the special background reduction techniques employed by the OSIRIS pipeline results in highly customized segmentation maps (see §4.3.3). These segmentation maps are different from the ones commonly used for imaging data, such as a quasi-Petrosian isophotal cut (Abraham et al., 2007). Even with all these techniques, we still are unable to achieve the same level of low brightness sensitivity as narrow band data, and as a result, our G values are systematically lower than the rest-frame UV imaging data (e.g., Lotz et al., 2004; Law et al., 2007a, 2009). Because of the extremely narrow field of view of OSIRIS, there are no reference stars that can be used for astrometry calibration between HST and OSIRIS data. This is another uncertainty for morphological comparisons, but we included HST images in Figure 4.5 when available. Their final alignments are done by visual inspection.

4.5 Kinematics

We create kinematic velocity maps of star-forming regions by fitting a Gaussian profile to the Hα emission line in each spaxel. Intensity, width, center position, and constant offset are obtained as fitted parameters, which are then converted to physical quantities of interest. The radial velocity map is obtained from the peak position with respect to Hα at the systematic redshift (Table 4.2). The velocity dispersion map is calculated from the width of

Table 4.4. IROCKS Morphologies

ID	r_g[a] [kpc]	d[b] [kpc]	G[c]	$M20$[d]	Ψ[e]
11655	2.79	···	0.22	-1.29	2.25
10633	<0.88	···	0.14	-0.88	0.32
42042481	5.88	···	0.19	-1.18	5.16
J033249.73	4.68	···	0.11	-0.74	13.78
11169	···	8.97	0.18	-0.86	10.11
11169E	2.60	···	0.11	-0.86	3.34
11169W	2.55	···	0.21	-1.30	2.30
7187	···	9.19	0.14	-0.90	12.98
7187E	2.33	···	0.16	-1.42	3.71
7187W	3.55	···	0.10	-0.61	13.34
9727	4.82	···	0.12	-0.96	6.10
7615	5.00	···	0.11	-0.69	13.11
11026194	3.07	···	0.14	-0.85	4.95
12008898	···	17.35	0.29	-1.47	7.50
12008898N	1.04	···	0.22	-1.07	1.05
12008898S	2.88	···	0.29	-1.23	3.61
12019627	···	24.20	0.18	-1.08	17.42
12019627N	4.41	···	0.17	-1.15	14.61
12019627SE	2.66	···	0.18	-1.29	4.56
12019627SW	1.87	···	0.15	-0.94	1.72
13017973	7.59	···	0.09	-0.67	16.31
13043023	4.72	···	0.11	-0.87	9.80
32040603	1.96	···	0.21	-1.33	0.53
32016379	4.32	···	0.17	-0.76	8.62
32036760	3.09	···	0.16	-1.21	0.79
33009979	···	16.37	0.31	-1.37	7.66
33009979N	2.04	···	0.16	-1.06	2.80
33009979S	2.83	···	0.31	-1.58	1.58

[a]Radius of gyration by flux with respect to the flux weighted centroid.

[b]Distance between two components. When there are more than two components, it is the distance between the two farthest components.

[c]Gini parameter on a segmentation map.

[d]Second-order moment on a segmentation map.

[e]Multiplicity parameter on a segmentation map.

the Gaussian function, corrected for the spatially varying instrumental resolution (see §4.3.3). The third and last panels of Figure 4.5 show our radial velocity and velocity dispersion maps. For these kinematics maps, we apply the same segmentation criteria as those specified in §4.3.2.

We measure the SNR weighted averages of velocity dispersion, $\sigma_{\rm ave}$ (sometimes referred as $\sigma_{\rm mean}$; Law et al., 2009; Wisnioski et al., 2011), in our segmented kinematics maps. Since it excludes the global velocity gradient, it represents a more accurate measurement of the line-of-0sight velocity dispersion comparing to $\sigma_{\rm 1D}$. However, the gradient within a pixel scale, 0.1", beam smearing, and weighting method can still potentially bias the value. As a quick check, we apply a local velocity gradient correction to the dispersion. Half of the biggest velocity difference between vertical or horizontal immediate neighbor pixels, $\Delta v = 0.5 max(|v_{i+1,j} - v_{i-1,j}|, |v_{i,j+1} - v_{i,j-1}|)$, is subtracted from the local dispersion in quadrature, $\sigma^{\rm corr} = \sqrt{\sigma^2 - \Delta v^2}$. The SNR weighted average of $\sigma^{\rm corr}$ in our sample is typically $\sim$ 60 km/s, compared to $\sim$ 64 km/s for the non-corrected $\sigma_{\rm ave}$, which indicates the local velocity gradient within a pixel is small compared to the line-of-sight dispersion.

We also investigate thee effects of beam smearing on the observed velocities. Using one of the highest SNR sources in the sample, we find the un-smoothed data to have a dispersion lower ~4 km/s compared the smoothed data set. When the additional local gradient correction is applied to the un-smoothed data, the dispersion is lowered further by ~5 km/s. This confirms our other analysis in what we have seen globally in the other smoothed data sets.

Overall the line-of-sight velocity dispersion measurements are resolved, and after the local gradient corrections have been applied, they are found to be $\gtrsim$ 55 km/s across our sample. As shown in previous studies, this is significantly higher than velocity dispersions found in local galaxies. We note that our method for removing the local velocity gradient is not rigorous, and we have only included it as a convenient check. For the rest of our analysis, we will not apply this correction, which as we have shown has a $\lesssim$ 10% effect on our results.

In addition to velocity dispersion, we also measure the velocity shear, $v_{\rm shear}$, which is defined as a half of the maximum difference in rotational velocity, $0.5(v_{\rm max}$ - $v_{\rm min})$, in a galaxy. Because the axis of rotation is not well defined in most of our galaxies, instead of v_{max} and v_{min} being maximum and minimum velocities along the kinematic major axis (e.g, Förster Schreiber et al., 2006; Law et al., 2009), we use velocities in the main bodies of the galaxies. In order to avoid possible outliers and artifacts, we use a modified version of the method by Gonçalves et al. (2010), which calculates v_{max} and v_{min} as the mean of the highest and lowest 3 values. Given that the inclinations of the galaxies are not well constrained, and that the depth of observation is not sufficient to detect the full spatial extent, some galaxies do not show obvious disk-like velocity gradients. For these galaxies, $v_{\rm shear}$ represents the best possible unbiased rotation measurement. $v_{\rm shear}$, $\sigma_{\rm ave}$, the ratio v_{shear}/σ_{ave}, and $\sigma_{\rm 1D}$ are listed in Table 4.5.

In Table 4.5, we also report a combined velocity scale, S_K. This is a velocity indicator for tracing galaxy potential well depths proposed by Weiner et al. (2006), and defined as $S_K \equiv \sqrt{K v_{shear}^2 + \sigma_{ave}^2}$. We adopted $K = 0.5$ for a flat rotation curve whose density profile is $\propto r^{-2}$. Both $S_{0.5}$ and $\sigma_{\rm 1D}$ describe the total kinematic/potential energy of the galaxy and should have similar values, and they can serve an independent verification. Most sources have similar values between their multiple components. For a few cases when they are significantly different, those sources with high $v_{\rm shear}$ are likely dominated by low SNR regions in the data.

Figure 4.6 shows how $\sigma_{\rm 1D}$ and $\sigma_{\rm ave}$ change in different parameter spaces. Measurements of Wright et al. (2009), Law et al. (2009), Förster Schreiber et al. (2009), Wisnioski et al. (2011), Epinat et al. (2012), and ours are combined. While our $\sigma_{\rm 1D}$ spans a similar, wide range of 49 $<\sigma_{\rm 1D}<$150 km/s, as other surveys, our $\sigma_{\rm ave}$ spans very narrow range at lower values than other surveys. Interestingly, our only z $\sim$ 1.5 source (TKRS11169) shows a higher dispersion, $\sigma_{\rm ave} \sim$ 90 km/s, on both east and west components, which is consistent with the higher

Table 4.5. IROCKS: Kinematics

ID	σ_{1D}[a] [km/s]	σ_{ave}[b] [km/s]	v_{shear}[c] [km/s]	v_{shear}/σ_{ave}	$S_{0.5}$[d]
11655	100.8 ± 25.5	54.7 ± 3.0	125.9 ± 8.6	2.30 ± 0.20	104.5 ± 5.4
10633	58.4 ± 36.5	54.5 ± 4.0	7.8 ± 5.7	0.14 ± 0.11	54.8 ± 4.0
42042481	86.9 ± 15.6	66.6 ± 1.4	179.4 ± 15.7	2.70 ± 0.24	143.2 ± 9.9
J033249.73	88.0 ± 33.2	71.0 ± 2.9	97.0 ± 14.1	1.37 ± 0.21	98.7 ± 7.2
11169E	140.5 ± 23.0	96.5 ± 3.4	125.5 ± 14.0	1.30 ± 0.15	131.1 ± 7.1
11169W	110.4 ± 13.7	88.0 ± 2.1	57.4 ± 9.8	0.65 ± 0.11	96.9 ± 3.5
7187E	85.9 ± 35.2	80.5 ± 2.5	130.3 ± 12.6	1.62 ± 0.16	122.3 ± 6.9
7187W	190.6[e]± 107.5	62.0 ± 3.5	239.8 ± 13.4	3.87 ± 0.31	180.5 ± 9.0
9727	65.6 ± 17.4	64.8 ± 2.5	89.1 ± 11.3	1.37 ± 0.18	90.4 ± 5.9
7615	75.1 ± 24.6	66.1 ± 2.3	89.0 ± 12.7	1.35 ± 0.20	91.3 ± 6.4
11026194	72.1 ± 21.7	64.0 ± 2.9	71.9 ± 9.7	1.12 ± 0.16	81.7 ± 4.8
12008898N	65.1 ± 52.0	61.5 ± 6.8	62.6 ± 12.6	1.02 ± 0.23	75.8 ± 7.5
12008898S	68.2 ± 11.4	61.6 ± 1.2	73.6 ± 7.6	1.19 ± 0.12	80.7 ± 3.6
12019627N	72.8 ± 44.2	55.8 ± 5.0	191.9 ± 14.3	3.44 ± 0.40	146.7 ± 9.6
12019627SE	65.4 ± 23.4	48.0 ± 2.9	71.2 ± 14.6	1.48 ± 0.32	69.5 ± 7.7
12019627SW	51.9 ± 27.3	59.5 ± 4.0	68.3 ± 11.9	1.15 ± 0.21	76.6 ± 6.1
13017973	62.6 ± 19.1	65.3 ± 1.9	117.7 ± 15.6	1.80 ± 0.25	105.8 ± 8.8
13043023	59.5 ± 20.4	63.9 ± 1.9	65.4 ± 9.2	1.02 ± 0.15	78.8 ± 4.1
32040603	49.7 ± 19.4	55.1 ± 1.9	40.5 ± 8.4	0.73 ± 0.15	62.1 ± 3.2
32016379	54.0 ± 18.3	63.3 ± 2.0	64.0 ± 12.7	1.01 ± 0.20	77.8 ± 5.5
32036760	53.1 ± 13.2	55.0 ± 1.9	60.3 ± 12.7	1.10 ± 0.23	69.6 ± 5.7
33009979N	49.7 ± 19.2	49.9 ± 2.3	43.0 ± 8.2	0.86 ± 0.17	58.4 ± 3.6
33009979S	79.8 ± 16.8	61.0 ± 2.1	128.9 ± 15.3	2.11 ± 0.26	109.7 ± 9.1

[a]Gaussian width of 1D spectrum.

[b]SNR weighted average of dispersion map.

[c]$v_{shear} = 1/2(v_{max} - v_{min})$

[d]$S_{0.5} = \sqrt{0.5 v_{shear}^2 + \sigma_{ave}^2}$

[e]This component has double peak that cannot be separated spatially. See §4.3.3 and Appendix.

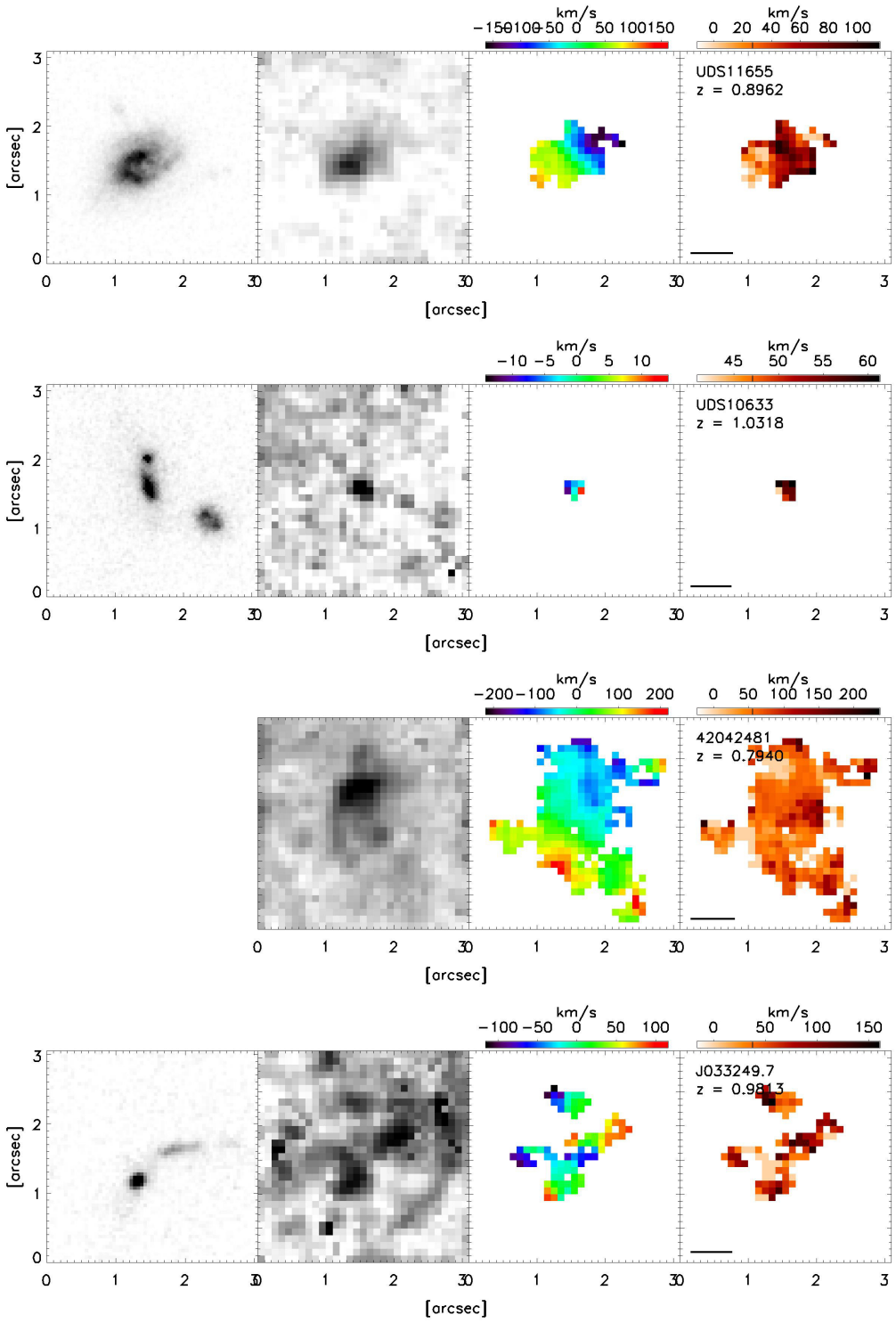

Figure 4.5 From the left, HST (if available), Hα flux, radial velocity, and velocity dispersion maps. The orientation of the images are fixed to be north up. On the right panel, the name of the source and its redshift are shown in the top, and the length of the black line on the left bottom corner represents 5kpc distance at that redshift.

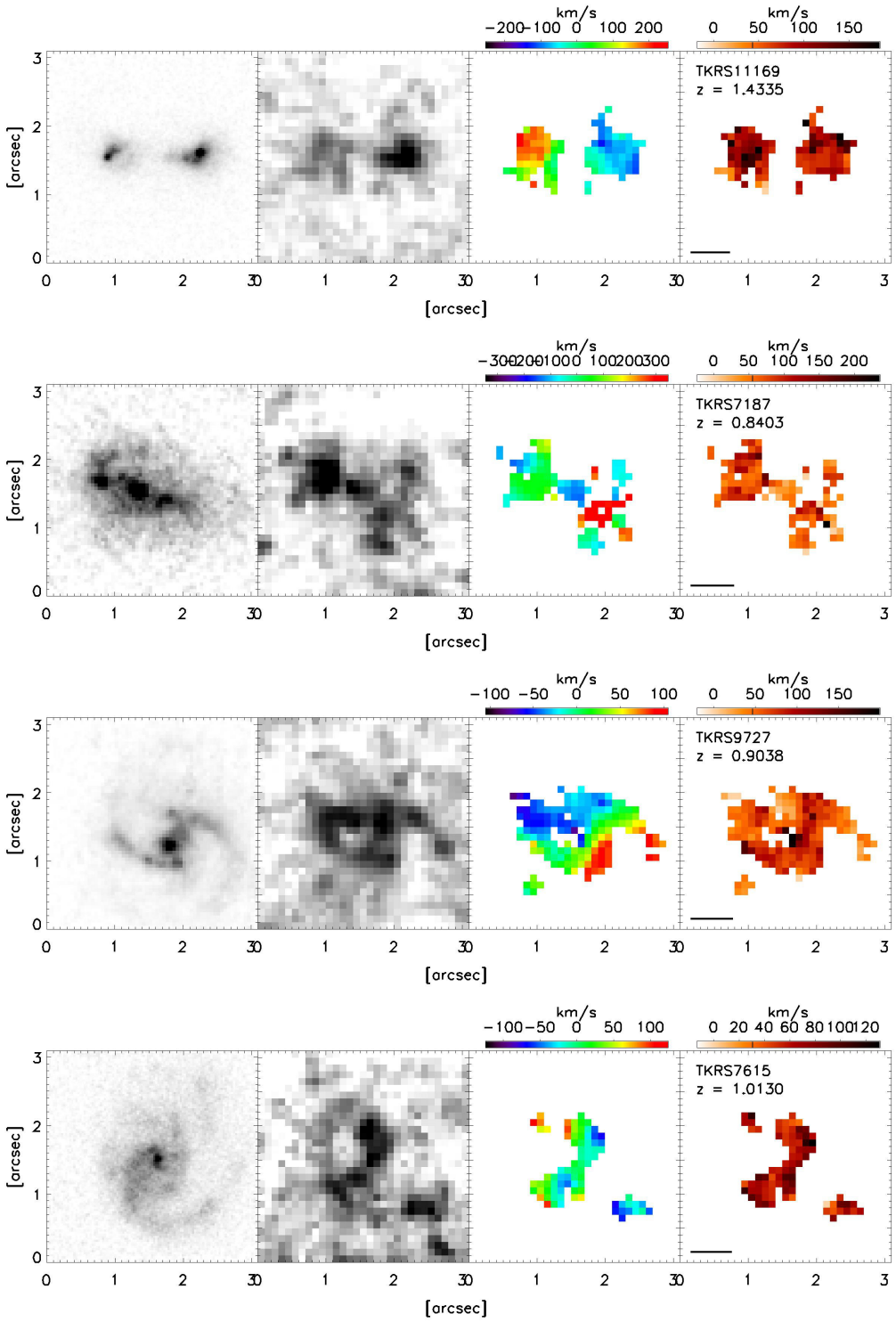
km/s
−200 −100 0 100 200
km/s
0 50 100 150
TKRS11169
z = 1.4335
[arcsec]
km/s
−300 −200 −100 0 100 200 300
km/s
0 50 100 150 200
TKRS7187
z = 0.8403
[arcsec]
km/s
−100 −50 0 50 100
km/s
0 50 100 150
TKRS9727
z = 0.9038
[arcsec]
km/s
−100 −50 0 50 100
km/s
0 20 40 60 80 100 120
TKRS7615
z = 1.0130
[arcsec]

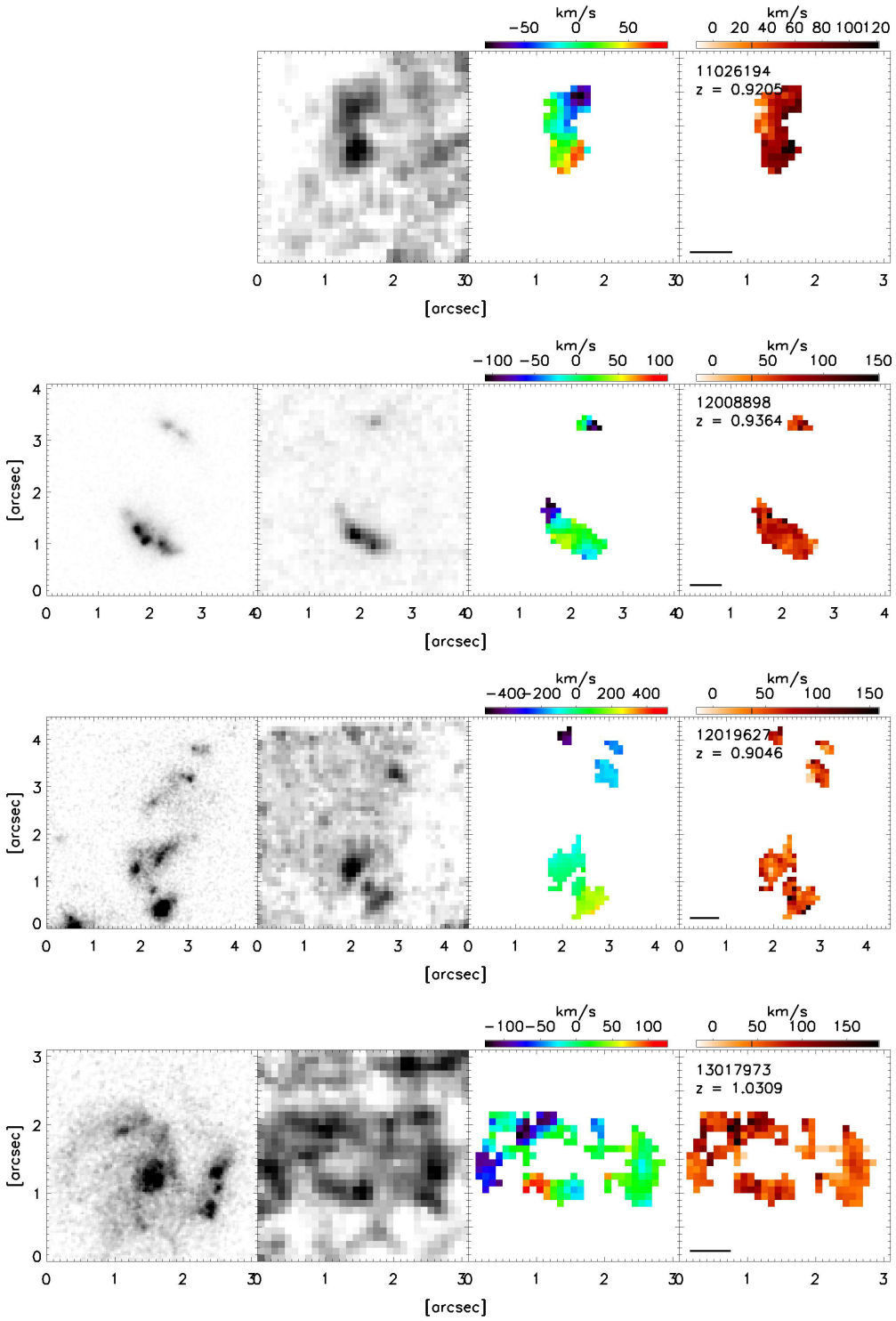
km/s
−50 0 50
km/s
0 20 40 60 80 100120
11026194
z = 0.9205
[arcsec]
km/s
−100 −50 0 50 100
km/s
0 50 100 150
12008898
z = 0.9364
[arcsec]
km/s
−400 −200 0 200 400
km/s
0 50 100 150
12019627
z = 0.9046
[arcsec]
km/s
−100 −50 0 50 100
km/s
0 50 100 150
13017973
z = 1.0309
[arcsec]

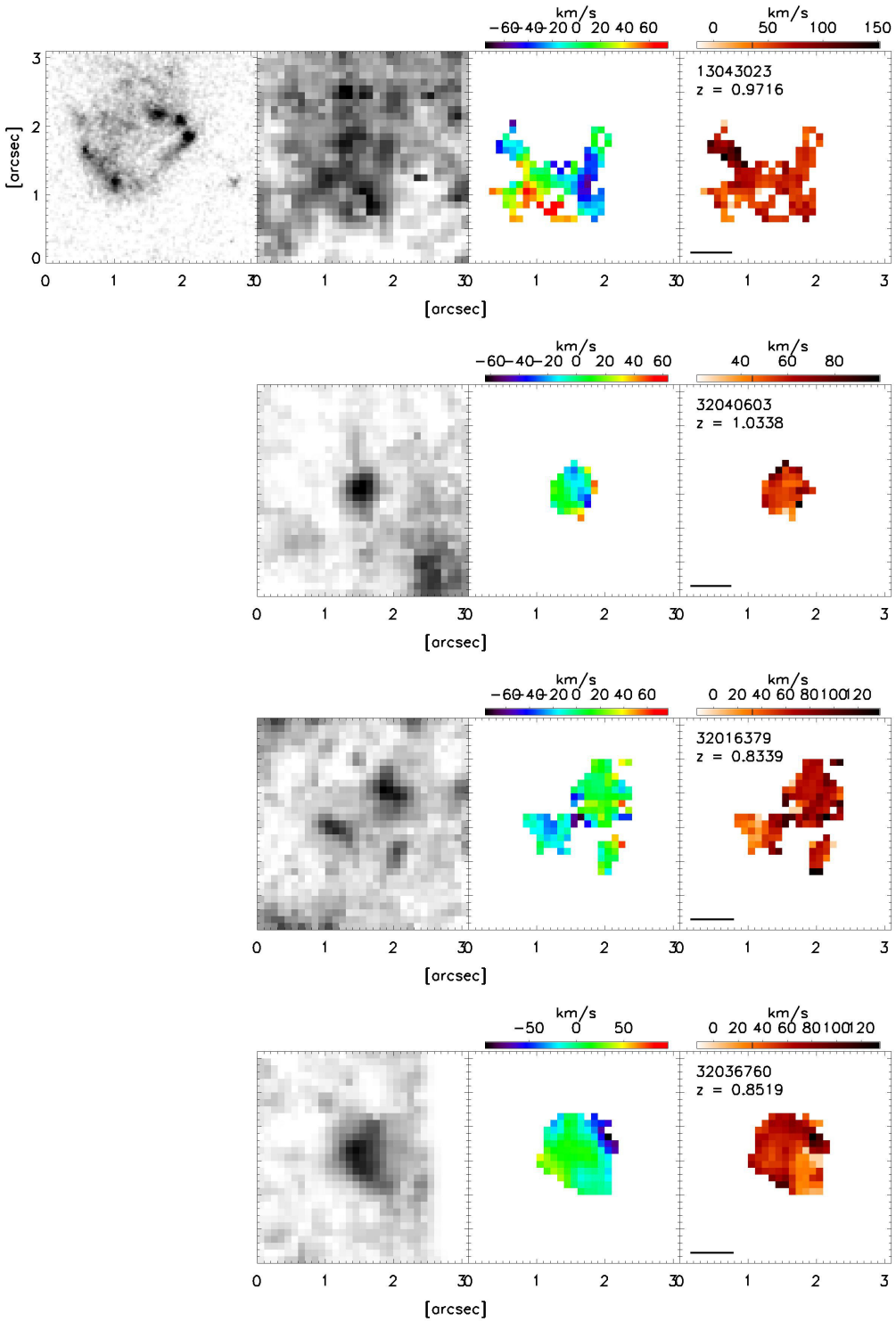
km/s
−60 −40 −20 0 20 40 60
km/s
0 50 100 150
13043023
z = 0.9716
[arcsec]
km/s
−60 −40 −20 0 20 40 60
km/s
40 60 80
32040603
z = 1.0338
[arcsec]
km/s
−60 −40 −20 0 20 40 60
km/s
0 20 40 60 80 100 120
32016379
z = 0.8339
[arcsec]
km/s
−50 0 50
km/s
0 20 40 60 80 100 120
32036760
z = 0.8519
[arcsec]

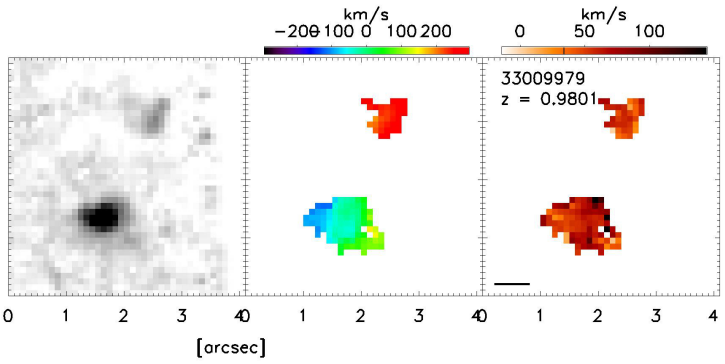

Table 4.6. IROCKS: Kinematic Models

ID	$P.A.$[a] [deg]	R_{peak}[b] [kpc]	V_p[c] [km/s]	$<\Delta>$[d] [km/s]	$\tilde{\chi}^{2}$[e]
11655	125.1	1.2	140.7	13.4	0.1
42042481	152.6	3.2	151.7	23.6	0.4
9727	223.8	0.5	109.9	13.2	0.1
33009979S[f]	249.9	0.5	81.7	30.8	0.7

[a]Position angle

[b]Radius where the rotational velocity reaches its peak

[c]Plateau velocity, $V_p = m_v R_p$.

[d]Average residual of |observed - model| kinematics.

[e]Reduced χ^2 between observed and model velocity field.

[f]Dynamical center is forced to be the Hα peak.

dispersion at higher redshift seen in the other surveys.

The $z \sim 1$ sample spans line-of-sight velocity dispersions of $48 \lesssim \sigma_{\rm ave} \lesssim 80$ km/s, velocity shears of $40 \lesssim v_{\rm shear} \lesssim 192$ km/s, and combined velocity scales of $58 \lesssim S_{0.5} \lesssim 147$ km/s (excluding 10633 and 7187W, see §4.3.3 and 4.4). Interestingly, only $z \sim 1.5$ source, 11169, has higher line-of-sight velocity dispersion ($\sigma_{\rm ave} \sim 90$ km/s) on both components. We will further discuss kinematic properties, in particular, disk settling using $v_{\rm shear}/\sigma_{\rm ave}$ values in §5.2.

4.6 Disk fits

We fit an inclined disk model to all galaxy's radial velocity map to determine if it is consistent with a disk galaxy. The disk model we use is a tilted ring algorithm for a symmetrically rotating disk (Begeman, 1987), which contains seven parameters; the center of rotation in the sky coordinates (x_0, y_0), position angle (PA) of the major axis (ϕ),

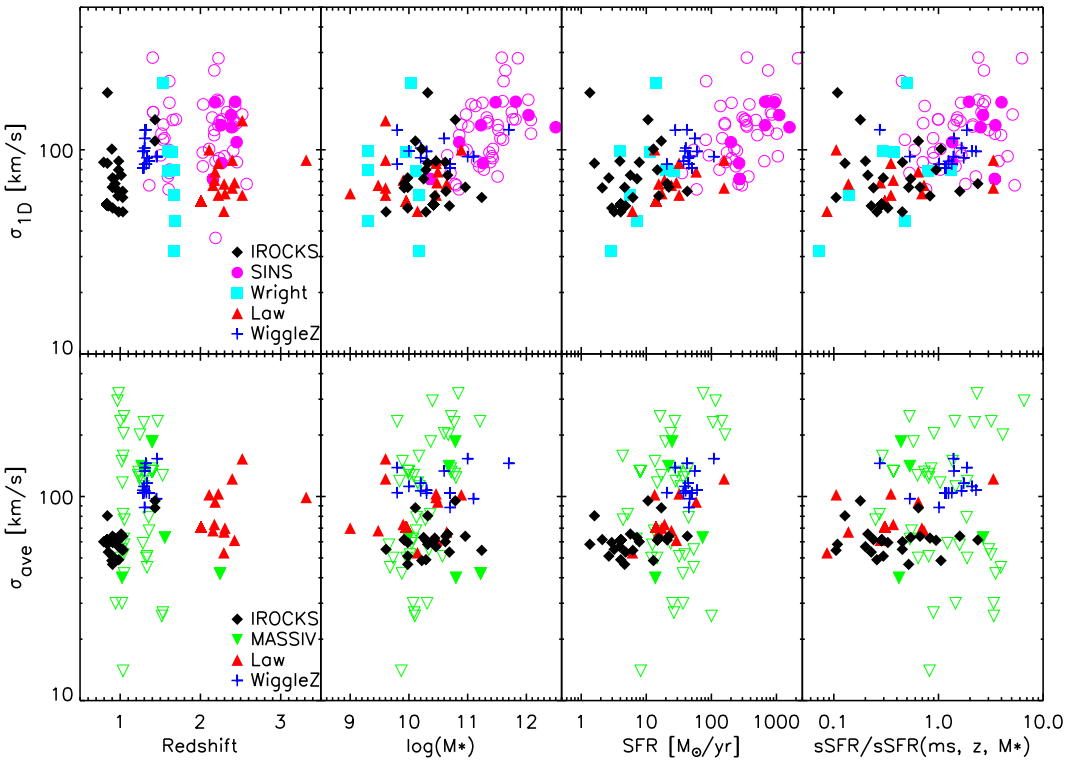

Figure 4.6 From the left, the relation of σ_{1D} (top) and σ_{ave} (bottom) to redshift, stellar mass, star formation, and normalized specific star formation. The symbols whose colors and shapes are the same but are open/filled are the difference between non-AO/AO within the same survey.

inclination angle (i), velocity slope (m_v), radius at which the plateau velocity is achieved in the plane of the disk (R_p), and systemic velocity offset (v_0). The observed radial velocity in the sky coordinates is described by:

$$v(x, y) = v_0 + V_c(R) \sin(i) \cos(\Theta), \tag{4.3}$$

where R and Θ are the polar coordinates in the plane of the galaxy, and V_c is the azimuthally symmetric circular velocity. Θ is related to the other parameters as follows:

$$\cos(\Theta) = \frac{-(x - x_0)\sin(\phi) + (y - y_0)\cos(\phi)}{R} \tag{4.4}$$

$$\sin(\Theta) = \frac{-(x - x_0)\cos(\phi) - (y - y_0)\sin(\phi)}{R\cos(i)}. \tag{4.5}$$

This model defines for a given radius, R, from the center in the plane, the velocity profile is increasing linearly, until it reaches the plateau velocity, V_p, at a plateau radius,R_p:

$$V_c = \begin{cases} m_v R & \text{if } R < R_p, \\ V_p = m_v R_p & \text{if } R \geq R_p. \end{cases} \tag{4.6}$$

Since the observed velocity map is a velocity field convolved with a PSF, we also convolve our model with a Gaussian profile whose FWHM is the summation in quadrature of the un-smoothed TT star FWHM and smoothing FWHM used in the science data (Table 4.1).

Since Hα detections only represent the regions of on-going star formation and not the entire extent of the galaxy, we cannot satisfactorily set a constraint on the inclination angle from the Hα morphology alone. Instead, we fix the inclination angle to be an expectation value, $< i >$, of 57.3° (e.g., Law et al., 2009). The best fit model is determined by the least-square method, weighted by error. Among the 23 components in our 17 IROCKS sources, four are well fitted by a disk model. We note that one of the four, 33009979S, has a velocity field that behaves differently near the center of the system comparing to the rest of the main body. Our simple model does not fully capture its complex velocity pattern, and our fitting algorithm does not easily converge. To aid with numerical convergence, we enforce the dynamical center to be at the Hα flux peak. The observed velocity maps, best fit models, residuals, and the rotation curves across the projected major kinematic axis are shown in Fig. 4.7, and the resultant disk parameters, average residuals, and reduced χ^2 values are listed in Table 4.6.

4.7 Derived Masses

§4.3.4 has already described how we obtained the stellar masses of our sources. We now move on to the estimates of the their gas, virial, dark matter halo, and enclosed masses, all (but gas masses) derived using the kinematics of the galaxies.

4.7.1 Gas mass

We estimate gas masses for the sample by using the relationship between gas depletion timescale (t_{dep}) and specific star formation rate (sSFR) normalized to the star-formation main sequence (SFMS) (Genzel et al., 2015). This

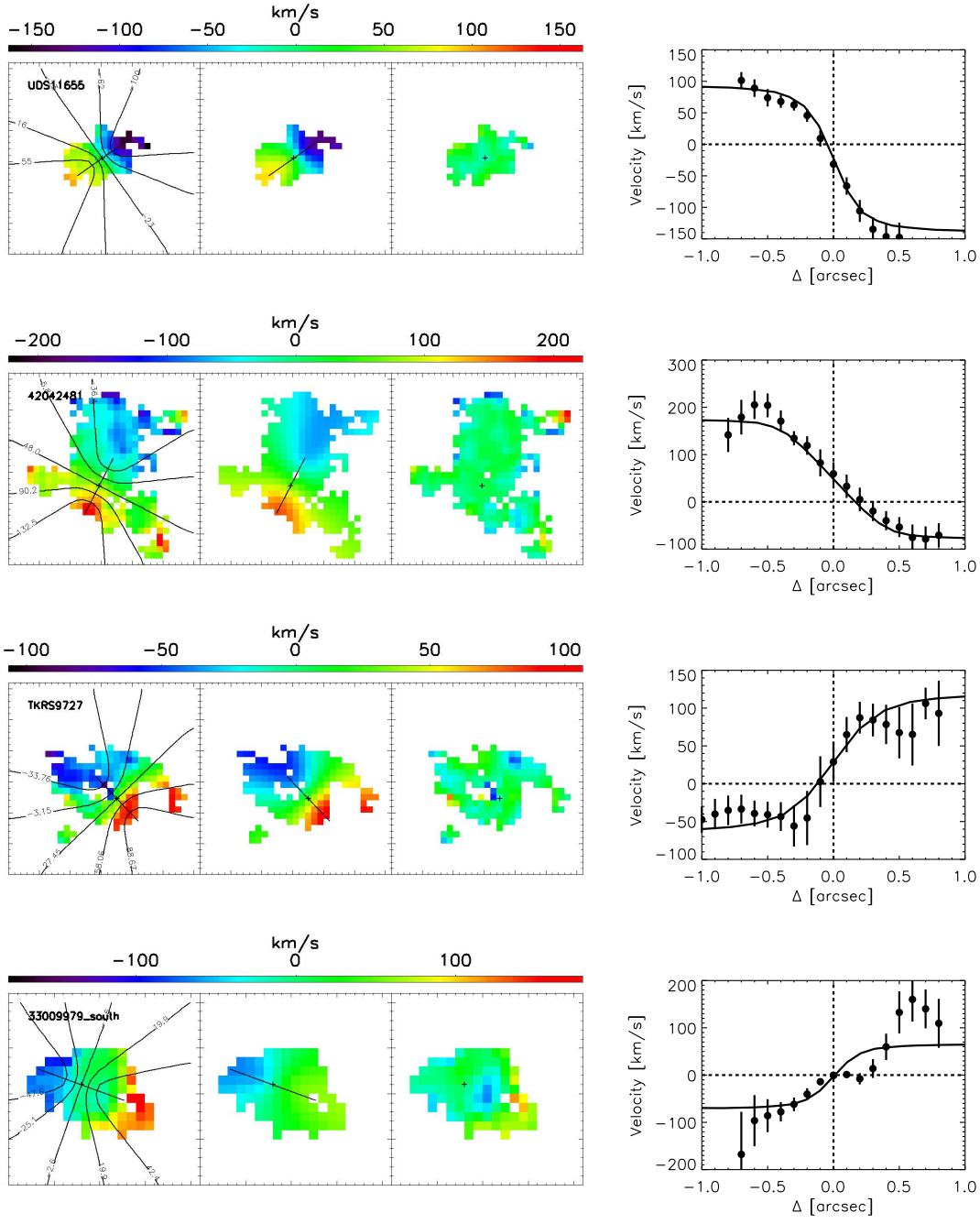

Figure 4.7 Kinematic inclined-disk best fit to four z∼ galaxies in our sample. Shown here are the observed radial velocity (left), fitted inclined disk model (middle), and the residual between observed and model radial velocities (right). Plus sign (+) shows the dynamical center, and the line shows the direction of velocity gradient.

employs the analytic fitting function of Whitaker et al. (2012) for the SFMS:

$$\log(\mathrm{sSFR}(\mathrm{ms}, z, M_*)) = -1.12 + 1.14z - 0.19z^2 - (0.3 + 0.13z)(\log M_* - 10.5), \tag{4.7}$$

where sSFR in [Gyr^{-1}] is the ratio of SFR in [$M_\odot/yr$] to the stellar mass M_* in [$M_\odot$], and ms denotes main sequence. The depletion timescale is defined as:

$$\begin{aligned} t_{\mathrm{dep}} &= M_{\mathrm{gas}}/\mathrm{SFR} \text{ or,} \\ t_{\mathrm{dep}} &= \Sigma_{\mathrm{gas}}/\Sigma_{\mathrm{SFR}}, \end{aligned} \tag{4.8}$$

where M_{gas}, Σ_{gas}, and Σ_{SFR} are the gas mass, gas surface density, and star formation rate per area, respectively. The depletion timescale in [Gyr^{-1}] is then related to z, sSFR, and M_* by the following empirical relation (Genzel et al., 2015):

$$\begin{aligned} &\log(t_{\mathrm{dep}}(z, \mathrm{sSFR}, M_*)|_{\alpha=\alpha_{\mathrm{MW}}}) \\ &= \alpha_f + \xi_f \log(1+z) + \xi_g \log(\mathrm{sSFR}/\mathrm{sSFR}(\mathrm{ms}, z, M_*)) + \xi_h(\log(M_*) - 10.5). \end{aligned} \tag{4.9}$$

We use the global fit values of +0.1, -0.34, -0.49, and +0.01 for α_{f1}, ξ_{f1}, ξ_{g1}, and ξ_{h1} (Genzel et al., 2015, Table 3). Multiplying SFR to the depletion time in Equation 4.9 gives the gas mass. These gas mass estimates ($M_{gas,1}$) are listed in Table 4.7.

For comparison, we also estimate gas masses using the relationship between Σ_{gas} and Σ_{SFR} (Kennicutt et al., 2007), modified for a Chabrier IMF:

$$\log\left(\frac{\Sigma_{gas}}{\mathrm{M}_\odot/pc^2}\right) = 0.73 \log\left(\frac{\Sigma_{SFR}}{\mathrm{M}_\odot/yr/kpc^2}\right) + 2.91. \tag{4.10}$$

Replacing SFR for the observed Hα luminosity using Equation 4.1, the gas mass is:

$$M_{gas,2} = 5.3 \times 10^{-22} L_{\mathrm{H}\alpha}^{0.73} \tag{4.11}$$

The values of $M_{gas,2}$ are listed in Table 4.7. Since we do not have the spatial distribution of stellar mass, Equation 4.11 can be applied locally to estimate spatial gas distribution and a total gass mass of each system.

4.7.2 Virial mass

Since σ_{1D} includes both global rotation and line-of-sight velocity dispersion, the virial mass within a radius, r_{vir}, can be estimated with an assumption of symmetric gravitational potential, if we assume the galaxy is virialized using the formula:

$$M_{vir} = \frac{C\sigma_{1D}^2 r_{vir}}{G}, \tag{4.12}$$

where G is the gravitational constant. The constant factor, C, represents the shape of the potential with respect to our viewing angle. For instance, $C = 5$ if the mass is uniformly distributed in a simple sphere, and $C = 3.4$ for a uniform thin disk with an average inclination (e.g. Erb et al., 2006b). We use $C = 3.4$ for our four disk candidate galaxies (UDS11655, 42042481, TKRS9727, and 33009979S), and $C = 5$ for the rest of the sample. Since it is difficult to define a clear size of the galaxy (see §4.4), we use the radius of gyration, r_g, as r_{vir}, although it is most likely an underestimate because r_g decreases for more centrally concentrated galaxies.

4.7.3 Masses for disk galaxies

For four galaxies that are well fitted by disk models, we estimate their dark matter halo masses and enclosed masses using the plateau velocities, V_p.

Dark matter halo mass

Assuming the halos to be spherical and virialized, then the circular velocity is expressed as $V_c = [GM(r)/r]^{1/2}$, where $M(r)$ is the total mass enclosed within r. As in common practice, we consider a dark halo within a radius r_{200}, where the mean enclosed density is 200 times the mean cosmic value $\overline{\rho}$:

$$r_{200} = \left[\frac{GM(r_{200})}{100\Omega_m(z)H^2(z)}\right]^{1/3}, \tag{4.13}$$

where Hubble's parameter H and matter density parameter Ω_m are related to their present values by $H(z) = H_0E(z)$, $\Omega_m(z) = \Omega_{m,0}(1+z)^3/E^2(z)$, and $E(z) = [\Omega_{\Lambda,0} + (1-\Omega_0)(1+z)^2 + \Omega_{m,0}(1+z)^3]^{1/2}$. The halo mass is then written as:

$$M_{halo} = \frac{0.1V_c^3}{H_0G\Omega_m^{0.5}(1+z)^{1.5}}. \tag{4.14}$$

We use the plateau velocity for V_c and show the halo mass estimates in Table 4.7.

Enclosed mass

The enclosed mass, which is often called a dynamical mass, refers to the mass residing in the disk-like component of the galaxy. It is calculated by assuming circular motion in a highly flattened spheroid described by the following equation:

$$M_{enclosed} = \frac{2V_c^2 r}{\pi G}. \tag{4.15}$$

Again, we use the plateau velocity, V_p for V_c. For r, we use the farthest distance from the dynamical center to the edge of the galaxy in the segmentation map. The resultant enclosed masses are listed in Table 4.7.

4.7.4 Mass Summary

In this section, we have estimated the gas masses, by two independent methods(Genzel et al., 2015; Kennicutt et al., 2007), and virial masses for our sources. For our four disk candidates, we have also estimated their halo masses and enclosed (dynamical) masses. While stellar mass ranges from $\log M_*/\mathrm{M}_\odot = 9.61$ to $\log M_*/\mathrm{M}_\odot = 11.24$, the first gas mass spans $9.10 \lesssim \log M_{\mathrm{gas,\,1}}/\mathrm{M}_\odot \lesssim 11.36$, and the gas fraction, $f_{\mathrm{mol\ gas}} = M_{\mathrm{gas}}/(M_{\mathrm{gas}} + M_*)$, spans $0.14 \lesssim f_{\mathrm{mol\ gas}} \lesssim 0.80$. Virial mass spans $9.54 \lesssim \log M_{vir}/\mathrm{M}_\odot \lesssim 10.62$ (excluding 7187W; see §4.3.3), which is in order-of-magnitude agreement with M_* and $M_{\mathrm{gas,1}}$. In particular, the masses of 10633 are not in good agreement between stellar mass ($\log \mathrm{M}_*/\mathrm{M}_\odot = 11.24$), gas mass ($\log \mathrm{M}_{\mathrm{gas}}/\mathrm{M}_\odot = 10.26$), and virial mass ($\log \mathrm{M}_{\mathrm{vir}}/\mathrm{M}_\odot = 9.54$). This source also has a Hα morphology that differs from the HST image, suggesting the Hα emission is not well detected. For the four disk candidates, their enclosed masses are in good agreement with their virial masses. For these four, halo masses are calculated, and these spans $11.08 \lesssim \log \mathrm{M}_{\mathrm{halo}}/\mathrm{M}_\odot \lesssim 11.95$.

There are uncertainties in the mass calculations that we will note here. Two gas mass estimates, $M_{\mathrm{gas,\,1}}$ and $M_{\mathrm{gas,\,2}}$, have a discrepancy of up to 1.5 order of magnitude ($M_{\mathrm{gas,\,2}}$ is always lower). $M_{\mathrm{gas,\,2}}$ is estimated solely from the Hα luminosity using the Kennicutt-Schmidt law (Hα luminosity to SFR then to gas mass), and there can be large uncertainties at each step. $M_{\mathrm{gas,\,1}}$ uses redshift, SFR, and stellar mass to estimate gas mass, and this

Table 4.7. IROCKS: Masses

ID	$\log M_*$[a]	$\log M_{gas,\,1}$[b]	$f_{mol\ gas}$[c]	$\log M_{gas,\,2}$[d]	$\log M_{vir}$[e]	$\log M_{halo}$[f]	$\log M_{enc}$[g]
11655	10.22	10.32	0.56	9.33	10.35	11.80	10.49
10633	11.24	10.26	0.09	8.94	9.54	···	···
42042481	10.62	10.06	0.22	9.48	10.55	11.95	10.79
J033249.73	10.46	9.72	0.15	9.21	10.62	···	···
11169E	10.79	10.28	0.24	9.60	10.78	···	···
11169W	10.11	10.45	0.69	9.72	10.56	···	···
7187	10.32	9.78	0.22	9.15	···	···	···
7187E	···	···	···	8.95	10.30	···	···
7187W	···	···	···	8.90	11.18	···	···
9727	10.96	11.04	0.55	9.45	10.22	11.50	10.28
7615	10.66	10.05	0.20	9.34	10.52	···	···
11026194	10.25	10.12	0.43	9.25	10.27	···	···
12008898N	···	···	···	8.96	9.71	···	···
12008898S	9.92	10.49	0.79	9.69	10.19	···	···
12019627	9.98	11.36	0.96	9.00	···	···	···
12019627N	···	···	···	9.08	10.43	···	···
12019627SE	···	···	···	9.00	10.12	···	···
12019627SW	···	···	···	9.11	9.77	···	···
13017973	10.63	10.82	0.60	9.84	10.54	···	···
13043023	10.44	10.49	0.53	9.49	10.29	···	···
32040603	9.61	9.10	0.24	8.88	9.75	···	···
32016379	10.42	9.76	0.18	9.27	10.17	···	···
32036760	10.69	9.91	0.14	9.23	10.01	···	···
33009979N	···	···	···	9.24	9.77	···	···
33009979S	10.29	10.39	0.56	9.65	10.15	11.08	10.40

[a]Stellar mass from SED model

[b]Total gas mass derived by the method of Genzel et al. (2015)

[c]Gas mass fraction by the method of Genzel et al. (2015)

[d]Total gas mass derived by the method of Kennicutt (1998)

[e]Virial mass estimate, $C = 3.4$ for disk candidates and $C = 5$ for non disks.

[f]Dark matter halo mass

[g]Enclosed (dynamical) mass

method likely gives a more reliable gas mass estimate (Genzel et al., 2015). However, the limitation is that the gas mass spatial distribution is not available, in contrast to $M_{\mathrm{gas,\,2}}$. For virial mass estimates, we use $C = 3.4$ (a uniform thin disk with an average inclination) for four disk candidates and $C = 5$ (uniformly distributed simple sphere) for the rest of the sample. Our four disk candidates are determined from the disk model fitting, which may be biased to galaxies that have larger IFS coverage. When the galaxy is small (under-sampled), the result of fitting has a higher uncertainty and is less reliable. We observe velocity gradients in small galaxies, such as 11026194, 12008898N, 33009979N, and they can potentially be disk candidates, but do not have enough spatial coverage. Therefore, the choice of C in the virial mass calculation may be a crude estimate. For enclosed mass estimates, we use the farthest distance from the dynamical center to the edge of the galaxy in the segmentation map as a radius. This radius estimate can be a under-estimation since the edges of a galaxy have low surface brightness, and AO observations are less sensitive to low surface brightness components (see §1.4).

4.8 Clumps

Observations of star-forming galaxies at high redshift show irregular morphologies, dominated by kpc-scale star-forming clumps (e.g., Förster Schreiber et al., 2009; Livermore et al., 2012). These clumps are likely a result of gravitational instability in the disk. They are speculated to migrate toward the galactic center through dynamical friction and form the galactic bulge (Bournaud, 2015, and reference therein); and/or be disrupted by stellar feedback and recycle its gas back to the ISM (Hopkins et al., 2012). In this section, we define the observed z∼1 clumps and present their properties.

There have been many definitions of "clumps" in the literature. For imaging studies, the definition ranges from visual inspection (e.g., Cowie et al., 1995b; Elmegreen et al., 2007), which is difficult to reproduce, to automated definitions based on the intensity contrast between the peak and the local background in galaxy images (Guo et al., 2012; Wuyts et al., 2012). For example, Guo et al. (2015) suggested UV-bright clumps as discrete regions that individually contribute more than 8 % of the rest frame UV light of their galaxies. In IFS studies, Genzel et al. (2011) required a clump to be local maxima in at least two separate velocity channels; while Wisnioski et al. (2012) identified their clumps solely from local Hα peaks in 2D Hα maps.

We define a clump as a local Hα flux peak that is separated by more than two pixels from other peaks in Hα maps (second panels in Figure 4.5). When the galaxy has only one concentrated peak, the "clump" is the whole galaxy itself. It is technically *not* a clump, but we include them in our analysis for completeness. Under this definition, we identify 68 isolated Hα peaks and 26 resolved resolved "clumps" in all 17 sources. We use the 68 isolated Hα peaks to investigate their Hα flux and velocity dispersion, and where we resolve the clumps we are able to measure their physical size.

For resolved clumps we measure the half-light radius through the following procedure: 1) we make an azimuthally averaged surface brightness profile centered at the peak, 2) compute the derivative of the surface brightness profile, 3) set the background to be the radius at which the derivative crosses 0 or reach less than 0.3, 4) subtract the background from the Hα map, and 5) apply aperture photometry to generate a growth curve. This method is robust when the surface brightness profile is steep. When the profile is shallow (i.e., size is large), the derivative slowly plateaus to 0, and the choice of 0.3 is not necessarily the best; however, a shallow profile also means the background value is not sensitive to the choice of the background location, so we do not expect this uncertainty to have a significant effect on our measurements.

After correcting for the smoothing width, we obtain our final clump sizes, denoted as $r_{1/2}$ in Table 4.8. Some clumps are smaller than beam sizes, and are considered unresolved. The number of resolved clumps are 26 in 15

sources (no clumps in 10633 and 13043023). The sizes of identified clumps are shown in Figure 4.8 as circles centered at the peaks. Figures are ordered from the highest to the lowest stellar mass estimated by SED fitting §4.3.4

The total Hα flux for each clump is measured by summing up the spectra inside the aperture radius, r_{ap}, the half-light radius before the smoothing width correction, and fitting a Gaussian profile to the Hα emission line. We assume a spatially uniform, ISM-only extinction to compare with other surveys (see §4.3.4 for HII and ISM extinction) when we convert Hα fluxes into SFRs. We also obtain each clump's σ_{1D}, measured from the width of the Gaussian function, and corrected for an average instrumental width within the aperture radius. The values of r_{ap}, SFR, and σ_{1D} are listed in Table 4.8. When the clump is unresolved, its SFR and dispersion values are still valid within the aperture, and we include them in our analysis. The clumps are marked as A, B, and so forth in a descending order of brightness in Figure 4.8.

We find that the $z \sim 1$ sample, star-forming clumps have a half-light radius between 0.43 to 4.27 kpc, σ_{1D} between 13 to 160 km/s, and SFR between 0.1 to 26 $M_\odot$ yr^{-1}. In §5.3, we will compare our clump parameters to other surveys such as those of Genzel et al. (2011); Wisnioski et al. (2012); Livermore et al. (2015).

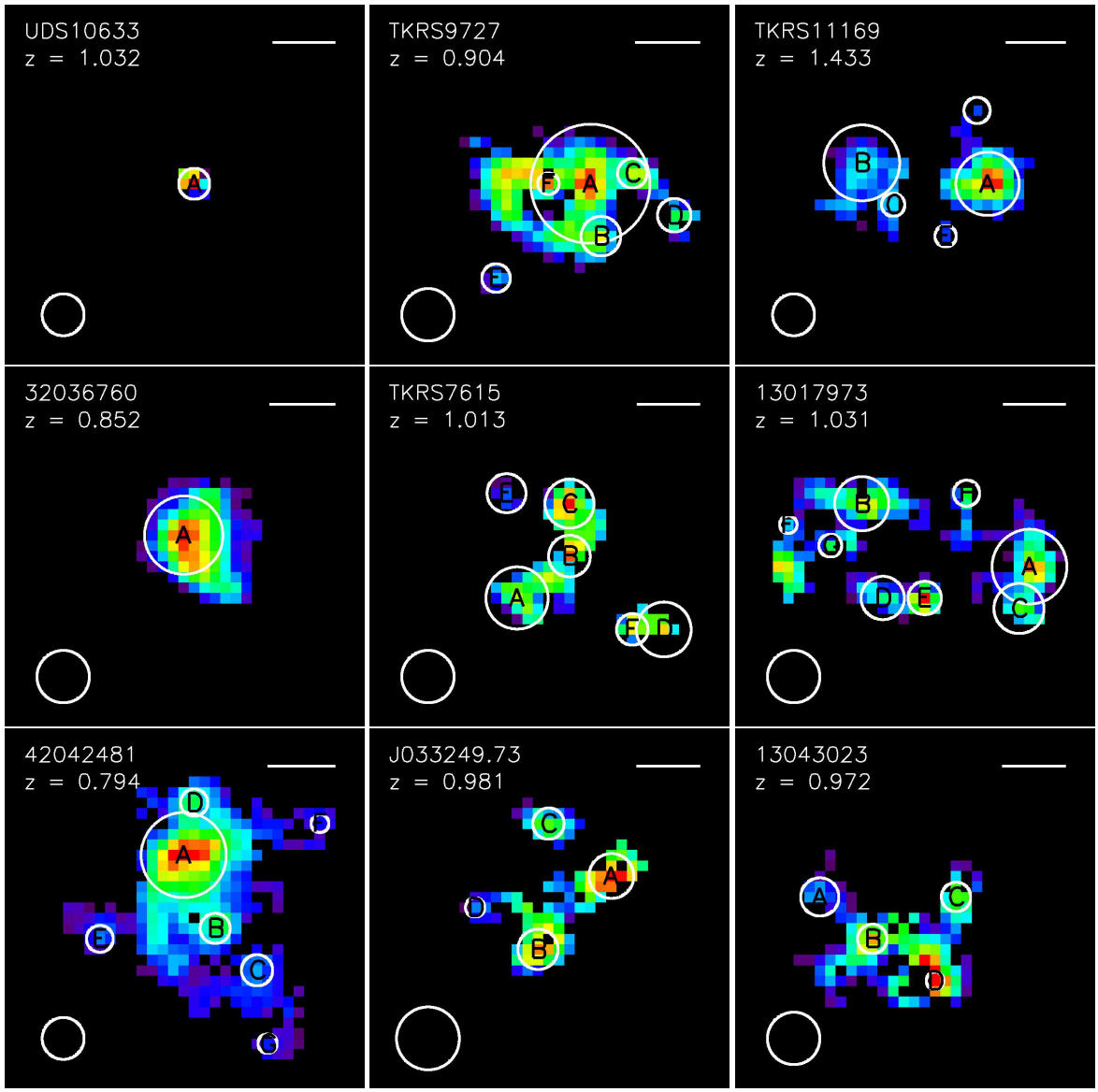

Figure 4.8 Identified clumps locations and sizes of IROCKS sample. In our definition, a clump is a local Hα peak that is separated by more than two pixels from neighbor peaks in Hα maps (second panels in Figure 4.5). The clumps are marked as A, B, and so forth in a descending order of brightness. Panels are organized from the highest to lowest stellar mass estimated by SED fitting. The name and redshift of the galaxy are listed at the top left corner. The length of top right line presents 5 kpc at that redshift. The circle at the bottom left presents the size of smoothing FWHM.

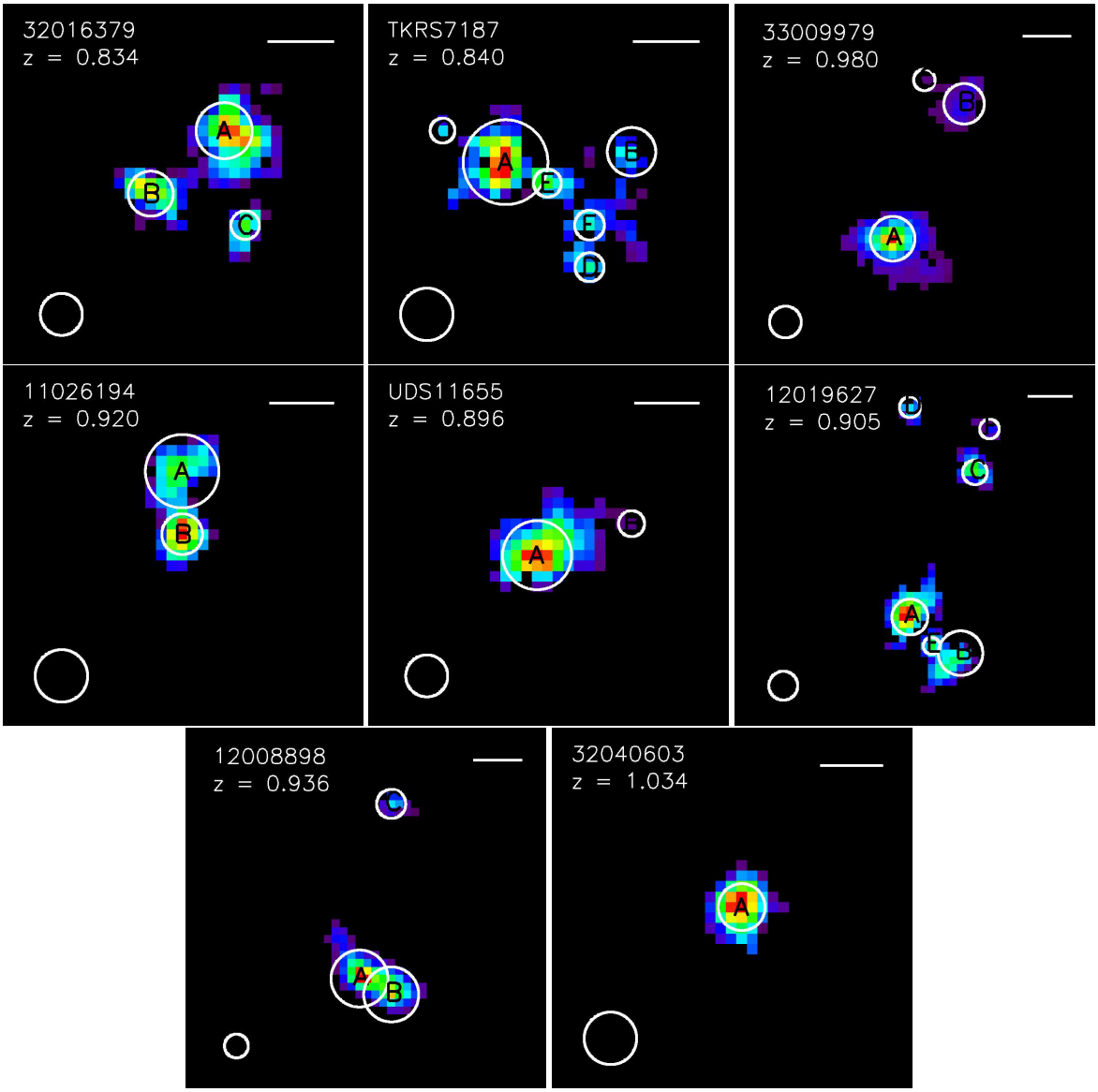
32016379
z = 0.834
A
B
C
TKRS7187
z = 0.840
A
E
F
D
33009979
z = 0.980
B
A
11026194
z = 0.920
A
B
UDS11655
z = 0.896
A
12019627
z = 0.905
C
A
B
12008898
z = 0.936
A
B
32040603
z = 1.034
A

Table 4.8. IROCKS: Clumps

ID	clump	$r_{1/2}$[a] [kpc]	r_{ap}[b] [kpc]	SFR[c] [$M_\odot$/yr]	σ_{1D}[d] [km/s]
11655	A	2.09	2.63	8.44	48.0
	B	···	0.99	0.56	67.8
10633	A	···	1.23	7.54	57.3
42042481	A	2.73	3.13	2.41	61.0
	B	···	1.10	0.21	43.6
	C	···	1.15	0.19	51.2
	D	···	1.00	0.16	50.1
	E	···	0.98	0.12	32.6
	F	···	0.66	0.10	131.8
	G	···	0.70	0.06	79.3
J033249.73	A	0.62	1.75	0.84	77.2
	B	···	1.57	0.78	61.8
	C	···	1.22	0.31	60.4
	D	···	0.76	0.19	93.4
11169	A	1.96	2.62	14.13	96.8
	B	2.62	3.14	9.53	113.9
	C	···	0.96	0.94	66.6
	D	···	1.08	0.88	64.4
	E	···	0.89	0.71	70.8
7187	A	2.75	3.17	1.88	87.7
	B	0.90	1.81	0.50	99.5
	C	···	0.93	0.17	71.7
	D	···	1.08	0.17	56.6
	E	···	1.03	0.14	24.5
	F	···	1.11	0.11	73.5
9727	A	4.27	4.56	26.80	89.7
	B	···	1.52	3.38	86.6
	C	···	1.13	1.69	45.4
	D	···	1.28	0.99	13.3
	E	···	1.09	0.79	40.6
	F	···	0.82	0.66	45.9
7615	A	1.81	2.45	1.78	79.4
	B	···	1.64	1.17	79.6
	C	0.99	1.93	1.15	60.6
	D	1.39	2.16	0.94	64.3
	E	···	1.53	0.60	70.8
	F	···	1.24	0.44	59.8
11026194	A	2.31	2.82	4.56	65.0
	B	···	1.56	2.25	76.4
12008898	A	2.41	2.91	13.89	61.4
	B	2.29	2.81	11.93	59.6
	C	···	1.48	2.07	54.0
12019627	A	1.18	1.99	1.93	45.6
	B	1.88	2.47	1.67	42.6
	C	···	1.36	0.92	58.5

Table 4.8 (cont'd)

ID	clump	$r_{1/2}$[a] [kpc]	r_{ap}[b] [kpc]	SFR[c] [$M_\odot$/yr]	σ_{1D}[d] [km/s]
	D	···	1.15	0.57	71.1
	E	···	0.92	0.39	54.4
	F	···	1.08	0.34	25.3
13017973	A	2.45	2.96	13.14	36.2
	B	1.36	2.14	12.03	161.5
	C	1.08	1.98	4.84	39.6
	D	0.43	1.71	4.19	60.4
	E	···	1.32	3.76	62.0
	F	···	0.69	1.31	117.6
	G	···	0.90	1.23	76.6
	H	···	1.03	0.99	46.6
13043023	A	···	1.49	2.31	104.5
	B	···	1.15	1.39	69.3
	C	···	1.14	0.96	61.1
	D	···	0.69	0.66	58.6
32040603	A	0.82	1.85	1.76	52.5
32016379	A	1.39	2.09	1.20	64.9
	B	0.61	1.68	0.63	27.2
	C	···	1.06	0.26	58.6
32036760	A	2.49	2.95	2.59	55.1
33009979	A	1.62	2.30	7.46	60.8
	B	1.29	2.09	2.44	42.8
	C	···	1.10	0.61	56.5

[a]Half-light radius of clump.

[b]Aperture size (i.e., non corrected size).

[c]ISM corrected SFR inside the half-light radius.

[d]Integrated velocity dispersion inside the half-light radius.

4.9 Summary

In this chapter, we have presented the first results of our IROCKS sample, which is the current largest sample of star-forming galaxies at $z \sim 1$, observed with IFS+AO. The sample consists of sixteen $z \sim 1$ and one $z \sim 1.5$ star-forming galaxies, selected from the four well studied fields, GOODS-North, GOODS-South, DEEP2, and UDS. All of our targets, but one, were observed with the upgraded OSIRIS spectrograph at the Keck I telescope, with the assistance of a newly upgraded AO system. We focused on the kinematics and morphological properties of star-forming galaxies at $z \sim 1$ by using Hα emission line as a star formation tracer. The results of our survey are summarized as follows:

1 In our sample of sixteen star-forming galaxies with $0.794 \leq z \leq 1.03$ (median $z = 0.936$), twelve are classified as "single" and four as "multiple" systems, based on the number of spectrally and/or spatially separated components observed. Our seventeenth source 11169 has $z = 1.43$, and is classified as a "multiple" system.

2 We computed the SFR for each galaxy. Taking into account extinction by ISM only, $SFR_{H\alpha}$ spans $0.2 \leq SFR^{0}_{H\alpha} \leq 42.7\ M_\odot\ yr^{-1}$. Applying extra attenuation from HII regions, it increases by a factor of ~ 2 to 5 and becomes $0.3 \leq SFR^{00}_{H\alpha} \leq 108.4\ M_\odot\ yr^{-1}$. We find that applying both ISM and HII extinction provides better agreement with the SFR esitmated from SED fitting.

3 Using line width measurements, we find all $z \sim 1$ components to have line-of-sight velocity dispersions of

$\sigma_{\rm ave} \gtrsim 48$ km/s, with a median value of 61.6 km/s. In comparison, both components in 11169 ($z \sim 1.4$) have $\sigma_{\rm ave} \sim 90$ km/s.

4 The stellar mass of each galaxy is estimated using SED fitting, and it ranges between $9.6 \leq \log \mathrm{M}_*/\mathrm{M}_\odot \leq 11.2$. Gas mass and virial mass are given through star formation rate and kinematics arguments, and they are between $9.10 \lesssim \log \mathrm{M}_{\rm gas,\,1}/\mathrm{M}_\odot \lesssim 11.04$ and $9.54 \lesssim \log M_{vir} \lesssim 10.62$, respectively. Using both stellar and gas mass, we find the gas fraction in these galaxies ranges between $0.14 < f_{\rm gas} < 0.80$.

5 Four (11655, 42042481, 9727, and 33009979S) out of twenty-one $z \sim 1$ components are well fitted by disk models with low residuals.

6 We identified 68 star-forming clumps, among which 26 are resolved. The sizes of resolved clumps are $r_{1/2} \gtrsim 0.5$ kpc, their SFRs are SFR > 0.8 $\mathrm{M}_\odot$ yr^{-1}, and integrated dispersions are $\sigma_{\rm 1D} > 36$ km/s.

In the next chapter, we will compare IROCKS with other high-redshift galaxy surveys and discuss their implications on the evolution of galaxies. We will also highlight the strengths and limitations of our current results, and use them to charter future work.

Chapter 5

Discussion and Future Work

In the last chapter, I presented the first results from the IROCKS survey of $z \sim 1$ star-forming galaxies. In this chapter, I discuss the implications of these results, in particular, those concerning the global resolved kinematics and properties of star-forming clumps in Section 5.2 and 5.3. I then discuss future prospects for extending this IFS z∼1 data set to future studies in Section 5.4. Finally, in Section 5.5, I summarize the results from the entire thesis, including the SLODAR instrumentation project for atmospheric turbulence experiments (Chapter 2), the OSIRIS grating upgrade at the Keck Observatory (Chapter 3), and the IROCKS $z \sim 1$ star-forming galaxy study using IFS+AO (Chapter 4).

5.1 Sample Bias

Each IFS data sets has potential for selection effects, and it is important to distinguish between each sample and their potential biases. Before discussing the IROCKS results, I will highlight the differences between each of these major IFS high-z surveys. Figure 4.6 shows data points of the SINS survey (Förster Schreiber et al., 2009), the MASSIV survey (Epinat et al., 2012), Law et al. (2007b, 2009), Wright et al. (2007, 2009), the WiggleZ survey (Wisnioski et al., 2011), and IROCKS in four different parameter spaces (redshift, stellar mass, star formation rate, and normalized specific star formation rate). The most noticeable difference is seen in the SINS sample: significantly higher stellar mass and SFR, and overall higher 1D velocity dispersion (σ_{1D}) than the other samples (top second and third panel). A large fraction of the SINS sample has $\log M_*/\mathrm{M}_\odot > 11$, while most of the other samples have $\log M_*/\mathrm{M}_\odot < 11$. Except most of SINS sample, the rest of IFS galaxies span similar stellar mass ranges with Law et al. (2007b, 2009) and Wright et al. (2007, 2009) extend to lower stellar mass ($\log M_*/\mathrm{M}_\odot < 9.5$). Among the galaxy population today ($z = 0$), almost all late-type galaxies have stellar masses of $\log M_*/\mathrm{M}_\odot < 11$, and massive galaxies are dominated by early-type galaxies (e.g. Figure 6 of Schawinski et al., 2014). Our Milky Way Galaxy, for instance, has $\log M_*/\mathrm{M}_\odot \sim 10.8$ (McMillan, 2011). The massive galaxies in the SINS sample will most likely evolve to elliptical galaxies seen today, while the disk-like galaxies today are more likely to be evolved from $\log M_*/\mathrm{M}_\odot < 11$ galaxies at high redshifts. It is therefore important to bear in mind that when comparing galaxy properties, such as size, star formation rate, and velocity dispersion, between different surveys, the observed trends in redshift may be biased by the fact that different surveys target galaxies that possibly follow different evolutionary tracks.

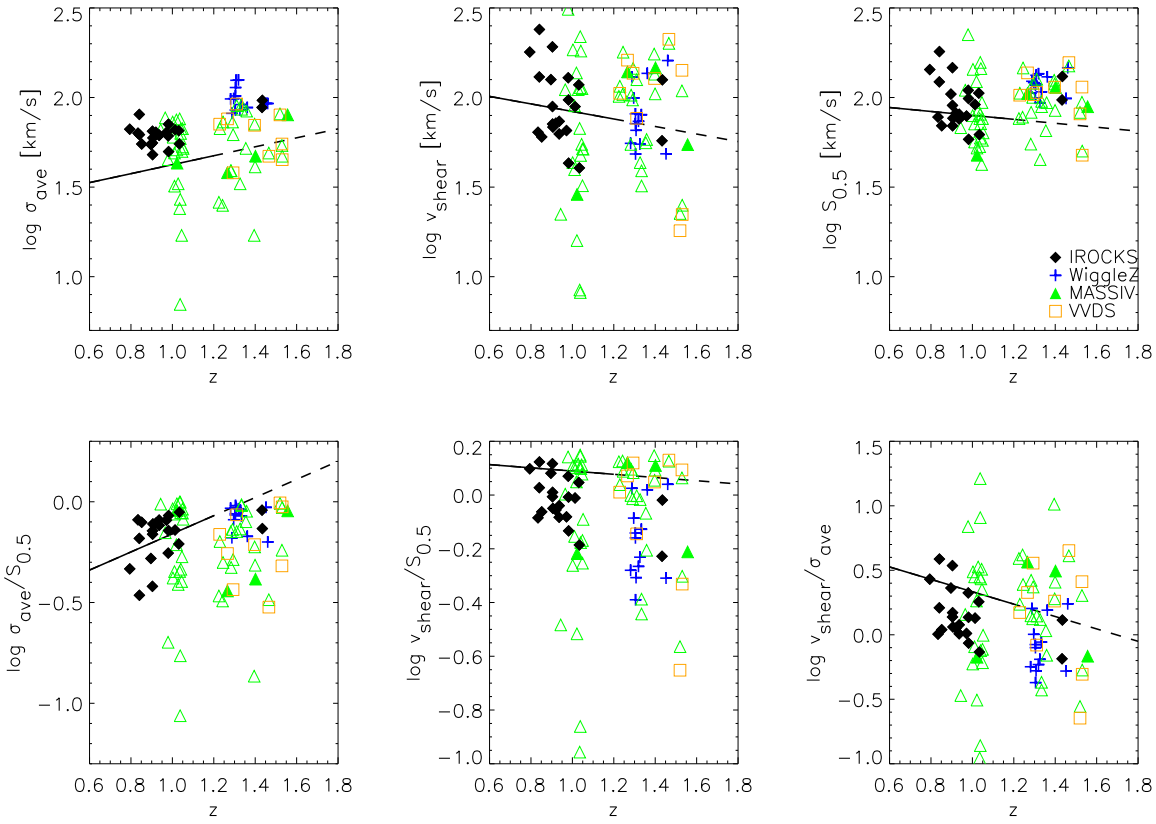

Figure 5.1 Evolution of $\sigma_{\rm ave}$, $v_{\rm shear}$, $S_{0.5}$, and their ratios measured by IROCKS and other IFS high redshift galaxy studies (Epinat et al., 2009; Wisnioski et al., 2011; Epinat et al., 2012). The symbols whose colors and shapes are the same but are open/filled are the difference between non-AO/AO within the same survey. Relationships found by the 1D spectrum study of Kassin et al. (2012) are extended to higher redshifts, and are over-plotted as a black line. Dashed lines are extrapolations beyond $z > 1.2$.

5.2 Discussion on Kinematics of z∼1 galaxies

Measurements of kinematics allow one to probe the process of disk settling that leads to present-day spiral galaxies. In Figure 5.1, we compare the IROCKS sample's $\sigma_{\rm ave}$, $v_{\rm shear}$, and $S_{0.5}$ values as a function of redshift with those reported by other high-z surveys (Epinat et al., 2009, 2012; Wisnioski et al., 2011). We also plot the relationship found by the 1D long-slit study of Kassin et al. (2012) for comparison. For a galactic disk to be considered settled, one expects its organized motion in rotation to dominate over random motion, hence $v_{\rm shear}/\sigma_{\rm ave} >> 1$. This quantity as a function of redshift is shown in the lower right panel of Figure 5.1.

Our measurements deviate from the kinematic relationships found by Kassin et al. (2012): we generally find a higher velocity dispersion, and lower $v_{\rm shear}/\sigma_{\rm ave}$ ratio. Most components in the IROCKS sample have $v_{\rm shear}/\sigma_{\rm ave}$ $\sim$ 1, and only five have $v_{\rm shear}/\sigma_{\rm ave}$ >2. If we apply the definition of settled fraction proposed by Kassin et al. (2012) ($v_{\rm shear}/\sigma_{\rm ave}$ >3), this fraction in our sample would be 2/21, or $\sim$ 10%, which is lower than the disk fraction expected. Some of this discrepancy may be reconciled by a difference in the $v_{\rm shear}$ definition: Kassin et al. (2012) correct their $v_{\rm shear}$ values for inclinations between $30^\circ < i < 70^\circ$, using axis ratios of $V+I$ band HST images, while we do not include any inclination dependence in ours. This difference accounts for at most a factor of two increase in $v_{\rm shear}$ values, which may be one of the reasons why our settled fraction appears to be low. Besides inclintation

effects, our $v_{\rm shear}$ measurements are similar to those of Kassin et al. (2012), implying that the velocities in our sample, both in rotation and dispersion, are higher than their sample.

While $v_{\rm shear}$ measurements may be ambiguous due to the lack of inclination information, the elevated dispersion we measure is robust and consistent with previous IFS+AO studies that found an elevated dispersion comparing to 1D studies. In fact, together with the WiggleZ survey (Wisnioski et al., 2011), who also used IFS+AO, our combined results show a steady decrease of $\sigma_{\rm ave}$ and increase of $v_{\rm shear}/\sigma_{\rm ave}$, consistent with the picture of disk settling.

Other than using $v_{\rm shear}/\sigma_{\rm ave}$, an independent method of determining a disk fraction is through disk fitting. Reiterating our conclusions from Chapter 4, we found four components well-fitted by an inclined disk model. Indeed, three of these disk candidates have some of the highest $v_{\rm shear}/\sigma_{\rm ave}$ (>2) in our sample, while the last one is a nearly face-on disk. Additionally, there are some components, such as DEEP12008898N and 33009979N, that show velocity gradients consistent with rotation by visual inspection, but their small sizes prevent reliable fitting. Overall, it is likely that the common notion that about one-third of the galaxies in high redshift samples are disk-like also applies in our $z \sim 1$ sample, but we need finer sampling and deeper observations to confirm this.

In the last few years, more realistic (with more physics considered) high resolution simulations have become available, and galaxy formation and evolution are now studied at individual galaxy structure size scales. Kassin et al. (2014) compared their observed properties against four zoomed-in hydrodynamics simulations, and found that both their cold (without feedback) and warm (with stellar feedback) gas models follow the same kinematics trend; decreasing $\sigma_{\rm ave}$ and increasing $v_{\rm shear}$ in time. Interestingly, their observational results lie between the cold and warm gas models both in value and in trend. Our results also fall between the two models at $z \sim 1$, suggesting at least a moderate amount of feedback is needed to reproduce our results. However, Kassin et al. (2014) have also commented on their results' possible dependencies on poorly constrained quantities such as the average stellar mass of galaxies and the spatial variations of gas density and temperature. Simulations which probe parameters such as stellar mass, feedback mechanism, and metallicity would certainly be helpful for pinpointing the physics that dictate "feedback" in galaxy evolution.

5.3 Discussion on z~1 Clumps

The empirical properties of star-forming clumps can provide clues to the physical mechanisms that drive their formation and evolution, and it is interesting to compare them to local HII regions. Wisnioski et al. (2012) compared their observations on $z \sim 1.3$ star-forming clumps with data on HII regions and found tight scaling relations between the clump size, luminosity, and velocity dispersion. This led them to conclude that clumps at $z \sim 1.3$ are likely larger analogs of local HII regions. On the other hand, Livermore et al. (2015) using observations on gravitationally lensed galaxies, combined with previous lensed and non-lensed galaxies, found that the mean surface brightness of clumps evolves with redshift, becoming brighter as redshift increases. They argued that this can be explained by an evolving gas mass fraction that increases with redshift, which translates to a higher star formation rate density if the clumps are results of disk fragmentation via gravitational instability. These two results imply two distinct formation mechanisms for star-forming clumps. We will compare our IROCKS measurements with these results, and attempt to reconcile the differences.

Figure 5.2 shows the SFR surface density, $\Sigma_{\rm SFR}$, as a function of redshift, of IROCKS and data points from other surveys (Genzel et al., 2011; Wisnioski et al., 2012; Livermore et al., 2015). Also shown in the Figure is Equation 5 of Livermore et al. (2015), the empirical relation they proposed. We find excellent agreement with their relation, which we consider to be supporting evidence for the disk fragmentation scenario. At the same time,

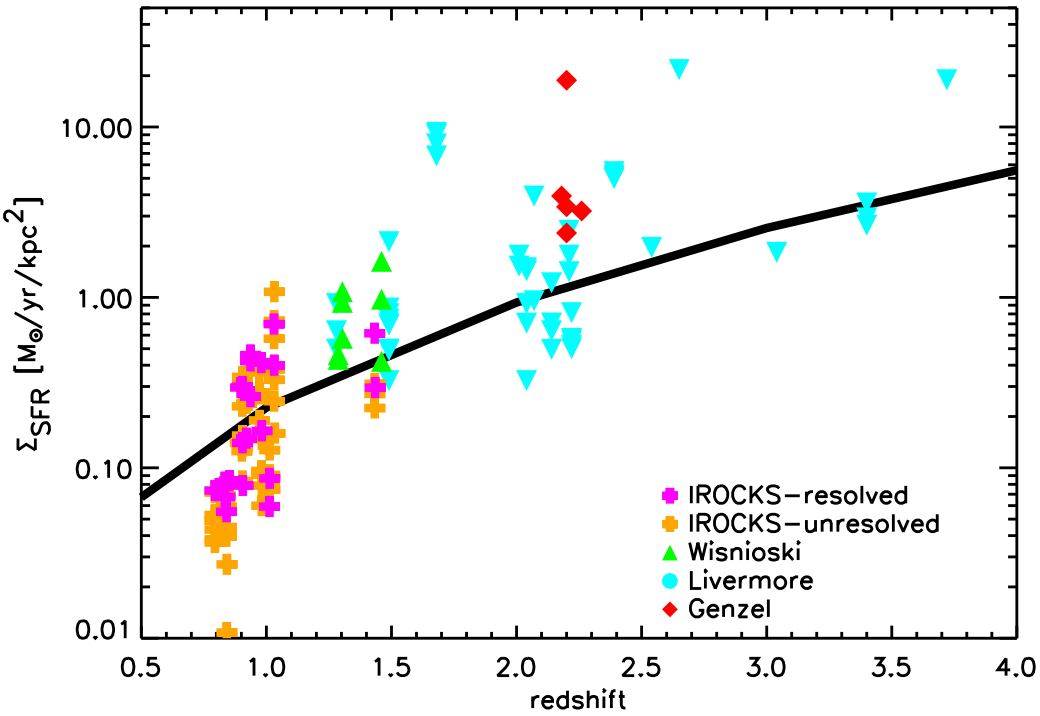

Figure 5.2 Star formation rate surface density of clumps as a function of redshift. IROCKS and previous survey (Genzel et al., 2011; Wisnioski et al., 2012; Livermore et al., 2015) measurements are plotted with an empirical fit by Livermore et al. (2015). IROCKS data points are separated between resolved (magenta) and unresolved (orange) (see §4.8).

our Figure 5.3 shows the relations between our clump size, luminosity, velocity dispersion, and Σ_{SFR}, together with data points from the same surveys as Figure 5.2. While Wisnioski et al. (2012) found that clump luminosity scales with size by the relation: $L \propto r^{2.72}$, using IROCKS data only, we find $L \propto r^{2.36}$. We do not consider this difference to be significant. In fact, like Wisnioski et al. (2012), we find our relation can be reasonably extended to HII regions in $z \sim 0$. However, as already shown by Figure 5.2, this does not imply a lack of time evolution in clump properties. Interestingly, we find that even though we have similar velocity dispersions as the other IFS studies, the SFR surface density is lower in our sample. Clumps with a given velocity dispersion is able to occupy a range of SFR surface density conditions. There are variety of ways to explain this scenario, one explanation could potentially involve the gas fraction of the clump.

Why local HII regions follow a similar luminosity-size scaling relation for high redshift star-forming clumps, despite likely different formation mechanisms, remains an unanswered question. The z∼1 star-forming clumps seem to behave like scaled up versions of the local HII regions when following the size clump relation, similar to Wisnioski et al. (2012). It is important to note that even though high-z clumps and local HII regions share similar relations, they do not occupy the same parameter space, i.e., star-forming clumps are orders of magnitude larger. As a result, when fitting both clump and HII region data for $L \propto r^n$, the resulting relation may be describing how L is different between HII regions and star-forming clumps, rather than between how small and large the regions/clumps.

The z∼ 1 clumps agree well with the slightly higher redshift IFS samples from Wisnioski et al. (2012), but

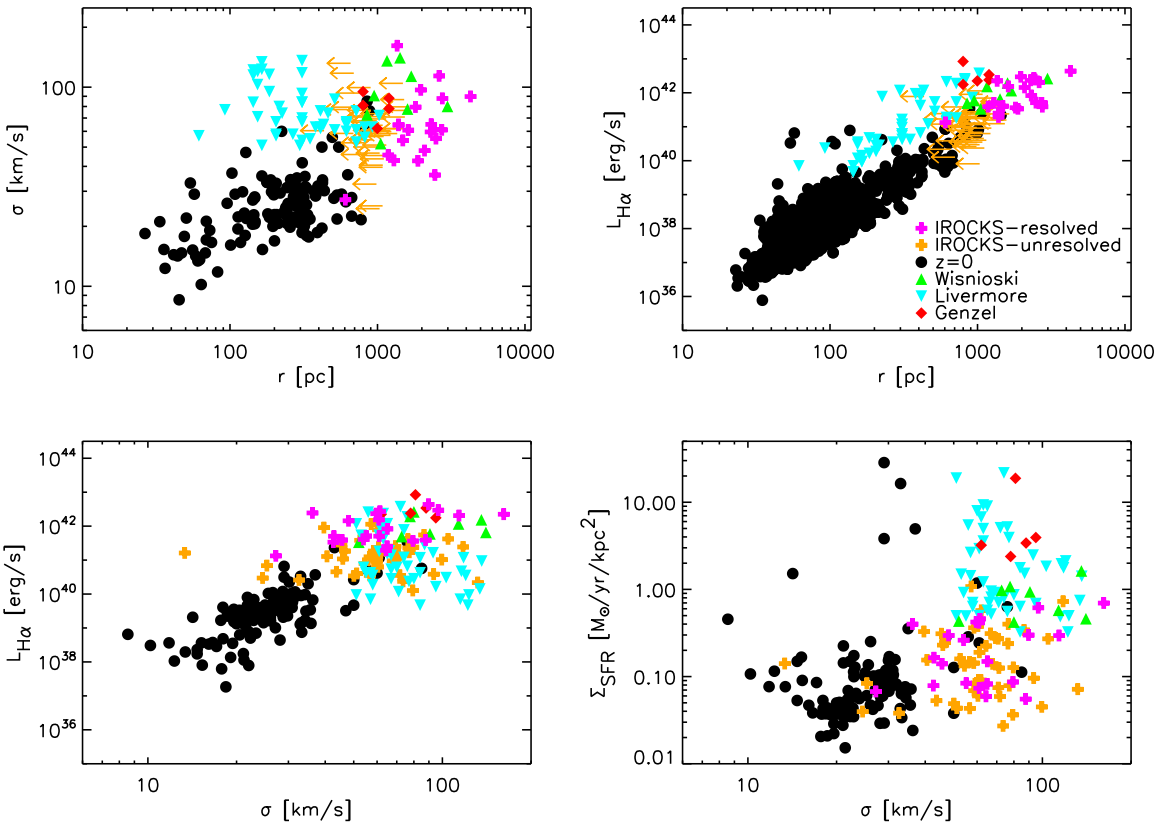

Figure 5.3 Clump size, velocity dispersion, luminosity, and SFR surface density relations. IROCKS and previous surveys (Genzel et al., 2011; Wisnioski et al., 2012; Livermore et al., 2015) are shown. $z = 0$ data points are described in Wisnioski et al. (2012). IROCKS data points are separated between resolved (magenta) and unresolved (orange) clumps or regions. For the top panel, where the x-axis is in units of radii (pc), unresolved points are shown as left point arrows to emphasize these size measurements are upper limits.

has some deviation from the IFS lensed galaxy samples from Livermore et al. (2015). Our clump SFR surface density measurements support the hypothesis of clumps forming from disk fragmentation. We find similarities between local HII regions and high-z star-forming clumps. Yet a larger statistical sample is still needed to explore redshift and stellar mass trends that could point to some environmental impact to clump properties. Also, a better understanding between observational and analysis differences between IFS lensed and un-lensed population is still warranted.

5.4 Future Work

The data we have taken with OSIRIS contains a wealth of information that we have yet to fully explore. For example, we can study the dynamical stability of the galactic disks using combined information from Hα flux maps and fitted disk models. The Toomre parameter Q describes the local gravitational stability of a gaseous disk, and is expressed as:

$$Q_{gas} = \frac{\sigma_0 \kappa}{\pi G \Sigma_{gas}}, \tag{5.1}$$

where Σ_{gas} is the gas surface density that can be evaluated from Equation 4.11, and κ is the epicyclic frequency of the disk. $Q < 1$ is expected to trigger disk fragmentation, and even $Q \sim 1$ to 2 can cause instability-driven large scale turbulence. In our sample, four components (11655, 42042481, 9727, and 33009979S) are well fitted by disk models, so using locally measured gas surface density, velocity dispersion, and rotation, Q can be computed. A precise measurement of local Q values is a key diagnostic for determining whether the observed clumps are formed from disk fragmentation.

We are also interested in investigating spatially resolved line ratios that are coupled with kinematics. For instance, high [NII]/Hα peaks are often indicative of the existence of active galactic nuclei (AGN) (e.g., Wright et al., 2010; Newman et al., 2013b). Comparing galaxies with and without AGN can provide insights for our understanding of AGN as a feedback mechanism. For star-forming galaxies (i.e., non AGNs), [NII]/Hα can be used to estimate metallicity content, following the formula by Pettini & Pagel (2004):

$$12 + \log\left(\frac{\mathrm{O}}{\mathrm{H}}\right) = 8.9 + 0.57 \times \log\left(\frac{[\mathrm{NII}]}{\mathrm{H}\alpha}\right) \tag{5.2}$$

Combining resolved metallicity distributions with kinematics results, the MASSIV survey (Queyrel et al., 2012), using mostly seeing-limited data, found that metal-poor galaxies tend to have positive radial metallicity gradients while metal-rich galaxies have negative gradients, suggesting that metal-poor gas is fed to the galaxy near its center, possibly via cold flows. Their metallicity gradients were only resolved by two to three data points over 10 kpc, and consequently, only the crudest signs of the gradients were measurable. Because our AO data samples at a finer scale, a similar analysis on our IROCKS sample will not only serve as an independent test of their results, but also potentially reveal more detailed metallicity structures in high redshift galaxies.

As technology advances, the capability and influence of IFS continues to grow. For example, KMOS at VLT (Sharples et al., 2004, 2013) contains 24 IFUs to simultaneously observe 24 different pointings. It is now in use and has already started to collect the largest set of seeing-limited sample ever observed by an IFS instrument. Some results have already been produced (e.g., Wisnioski et al., 2015), and the nature of IFS high redshift galaxy studies has began to shift from small surveys of 10~20 galaxies, such as IROCKS and all previous IFS+AO surveys, to large, statistically significant seeing-limited surveys with sample sizes an order of magnitude larger. AO observations remain crucial, however; as Newman et al. (2013b) noted, the remarkable resolution provided by AO can lead to systematic differences in galaxy kinematics classifications between AO and non-AO observations.

While a large number of observations, with and without AO, is needed to advance our statistical understanding of the high redshift universe, it has also become apparent that deeper AO observations are also needed. For example, AO work has had the tendency to find dispersion-dominated systems, because its lower sensitivity to lower surface brightness emission at larger radii has limited its ability to capture the large-scale rotation of galaxies. This can be remedied by taking deeper observations, either by increasing observing time, which is often unrealistically expensive, or using a larger telescope. When extremely large telescopes of the 30-m class become available, IFS+AO studies of high redshift galaxies will be able to tap into the largely unexplored regions in outer galactic high redshift disks.

5.5 Summary

This thesis has attempted to evaluate and improve ground-based observations, and used these observations to study the dynamical and star-forming properties of distant galaxies.

I have presented optical and mechanical designs, and lab testing results, of a portable instrument that was used

in an Arctic site testing campaign. The instrument utilizes SLODAR, the triangulation technique, to measure the vertical profiles of atmospheric turbulence. Our Arctic results show that most of the turbulence ($\sim$ 50%) resides within 1km from the ground at this site, and that the median seeing is 0.65 arcsec, comparable to some of the best observing sites in the world.

I then described a microlens based integral field spectrograph, OSIRIS, which operates behind a recently updated adaptive optics system at the Keck I telescope. I have tested and evaluated the new spectrograph grating component, and found its efficiency to be $\sim$ 80%. After the new grating was installed on OSIRIS, the final throughput improved by an average factor of 1.83. Using this newly upgraded OSIRIS and AO system, we collected the largest $z \sim 1$ star-forming galaxy sample taken by IFS + AO. I have presented the kinematics and morphologies of sixteen $z \sim 1$ (and one $z \sim 1.4$) star-forming galaxies, and found higher than local, but lower than $z > 1.5$, line-of-sight dispersions ($\sigma_{\rm ave} \sim 60$ km/s) at $z \sim 1$. Combined with previous studies, our results are consistent with the expected rate of disk settling. Clump properties in the $z \sim 1$ galaxies were explored for the first time. Comparing to the other high-z clump sample, I showed that they support the models of disk fragmentation as the clump forming mechanism. We also confirm that the z$\sim$1 clumps follow a similar size-luminosity clump relation as local HII regions, even though they are orders of magnitude larger in star formation and size. These results impose interesting constraints on theoretical models of how star formation is generated in distant galaxies.

Appendix A

Adaptive smoothing

In IFS studies of high redshift galaxies, very often data cubes are spatially smoothed by a Gaussian function of FWHM ~ 2 pixels to increase the signal-to-noise ratio (e.g. Law et al., 2009; Wright et al., 2009; Förster Schreiber et al., 2009; Genzel et al., 2011; Wisnioski et al., 2011; Epinat et al., 2012). It usually does not significantly change the global kinematic parameters and stellar properties (e.g., σ_{1D}, σ_{ave}, and SFR) and hence does not affect the analysis results (see for example a discussion in §4.5). However, when we study the spatially resolved quantities, such as the metallicity gradient across the galaxy and resolved clumps, the smoothing process distributes the flux to neighbour pixels and as a result smear out the information. In particular, observations with AO, where diffraction limited observation is potentially achievable, lowering the spatial resolution in the data reduction process is least preferred. In order to increase SNR while preserving as high spatial resolution as possible, the choice of optimum width is crucial. I develop an adaptive smoothing code to find the best choice of smoothing width.

In short, the code iteratively applies smoothing of increasing FWHM to a data cube until spaxels reach a desired or optimal SNR. In each iteration, the entire reduced, un-smoothed cube is smoothed by a single FWHM, and the SNR of each spaxel in an Hα flux map is calculated using the method described in §4.3.3. For the next iteration, the same original, reduced, un-smoothed cube is then smoothed by a wider FWHM, usually increasing by 0.5 pixel for each iteration, and we repeat the process until the maximum FWHM is reached, or most spaxels achieve a high SNR. The smallest smoothing FWHM that allows the spaxel at [i, j] to reach the desired SNR is then recorded as FWHM$_{i,j}$. The most optimized, final smoothing width for the particular data cube is the mean FWHM$_{i,j}$ within the region of interest.

In the Chapter 4 analysis, I use this code only to find the most optimized smoothing width. However, this code has the potential to produce an adaptively smoothed data cube, where spaxels of higher signal would be smoothed by a narrower FWHM. Such a method is suitable for morphology related analysis (e.g., morphology parameter, size, peak location), and particularly beneficial when (1) the galaxy contains an AGN with a high single [NII]/Hα peak, which would allow for a more accurate measurement of the location of the AGN; also, when (2) multiple star forming clumps are located close to each other, which would prevent excess smoothing to smear the boundaries between them. On the other hand, a spatial varying smoothing length makes it difficult to model the beam size correctly. The potential of this method as numerous merits will be explored in future studies.

Bibliography

Abraham, R. G., Tanvir, N. R., Santiago, B. X., et al. 1996, MNRAS, 279, L47

Abraham, R. G., van den Bergh, S., & Nair, P. 2003, ApJ, 588, 218

Abraham, R. G., Nair, P., McCarthy, P. J., et al. 2007, ApJ, 669, 184

Agertz, O., Kravtsov, A. V., Leitner, S. N., & Gnedin, N. Y. 2013, ApJ, 770, 25

Allington-Smith, J., & Content, R. 1998, PASP, 110, 1216

Allington-Smith, J., Murray, G., Content, R., et al. 2002, PASP, 114, 892

Appenzeller, I., Fricke, K., Fürtig, W., et al. 1998, The Messenger, 94, 1

Babcock, H. W. 1953, PASP, 65, 229

Bacon, R., Copin, Y., Monnet, G., et al. 2001, MNRAS, 326, 23

Barman, T. S., Macintosh, B., Konopacky, Q. M., & Marois, C. 2011, ApJ, 733, 65

Begeman, K. G. 1987, PhD thesis, , Kapteyn Institute, (1987)

Bournaud, F. 2015, ArXiv e-prints, arXiv:1503.07660

Bournaud, F., Chapon, D., Teyssier, R., et al. 2011, ApJ, 730, 4

Bruzual, G., & Charlot, S. 2003, MNRAS, 344, 1000

Butterley, T., Wilson, R. W., & Sarazin, M. 2006, MNRAS, 369, 835

Calzetti, D. 2001, PASP, 113, 1449

Catala, L., Crawford, S. M., Buckley, D. A. H., et al. 2013, MNRAS, 436, 590

Chabrier, G. 2003, PASP, 115, 763

Charlot, S., & Fall, S. M. 2000, ApJ, 539, 718

Chilcote, J., Barman, T., Fitzgerald, M. P., et al. 2015, ApJ, 798, L3

Chin, J. C. Y., Stalcup, T., Wizinowich, P., et al. 2010, in Society of Photo-Optical Instrumentation Engineers (SPIE) Conference Series, Vol. 7736, Society of Photo-Optical Instrumentation Engineers (SPIE) Conference Series

Chin, J. C. Y., Wizinowich, P., Campbell, R., et al. 2012, in Society of Photo-Optical Instrumentation Engineers (SPIE) Conference Series, Vol. 8447, Society of Photo-Optical Instrumentation Engineers (SPIE) Conference Series, 4

Christou, J. C., Neichel, B., Rigaut, F., et al. 2010, in Society of Photo-Optical Instrumentation Engineers (SPIE) Conference Series, Vol. 7736, Society of Photo-Optical Instrumentation Engineers (SPIE) Conference Series, 1

Contini, T., Garilli, B., Le Fèvre, O., et al. 2012, A&A, 539, A91

Cowie, L. L., Hu, E. M., & Songaila, A. 1995a, Nature, 377, 603

—. 1995b, AJ, 110, 1576

Daddi, E., Dannerbauer, H., Elbaz, D., et al. 2008, ApJ, 673, L21

Daddi, E., Bournaud, F., Walter, F., et al. 2010, ApJ, 713, 686

Davies, R. I., Müller Sánchez, F., Genzel, R., et al. 2007, ApJ, 671, 1388

Dekel, A., & Birnboim, Y. 2006, MNRAS, 368, 2

Do, T., Ghez, A. M., Morris, M. R., et al. 2009, ApJ, 703, 1323

Do, T., Kerzendorf, W., Winsor, N., et al. 2015, ArXiv e-prints, arXiv:1506.07891

Do, T., Lu, J. R., Ghez, A. M., et al. 2013, ApJ, 764, 154

Drinkwater, M. J., Jurek, R. J., Blake, C., et al. 2010, MNRAS, 401, 1429

Driver, S. P., Windhorst, R. A., & Griffiths, R. E. 1995, ApJ, 453, 48

Eisenhauer, F., Abuter, R., Bickert, K., et al. 2003, in Society of Photo-Optical Instrumentation Engineers (SPIE) Conference Series, Vol. 4841, Instrument Design and Performance for Optical/Infrared Ground-based Telescopes, ed. M. Iye & A. F. M. Moorwood, 1548–1561

Ellis, R. S. 1997, ARA&A, 35, 389

Elmegreen, D. M., Elmegreen, B. G., Ravindranath, S., & Coe, D. A. 2007, ApJ, 658, 763

Epinat, B., Contini, T., Le Fèvre, O., et al. 2009, A&A, 504, 789

Epinat, B., Tasca, L., Amram, P., et al. 2012, A&A, 539, A92

Erb, D. K., Shapley, A. E., Steidel, C. C., et al. 2003, ApJ, 591, 101

Erb, D. K., Steidel, C. C., Shapley, A. E., et al. 2006a, ApJ, 647, 128

—. 2006b, ApJ, 646, 107

Faber, S. M., Phillips, A. C., Kibrick, R. I., et al. 2003, in Society of Photo-Optical Instrumentation Engineers (SPIE) Conference Series, Vol. 4841, Instrument Design and Performance for Optical/Infrared Ground-based Telescopes, ed. M. Iye & A. F. M. Moorwood, 1657–1669

Förster Schreiber, N. M., Shapley, A. E., Erb, D. K., et al. 2011a, ApJ, 731, 65

Förster Schreiber, N. M., Genzel, R., Lehnert, M. D., et al. 2006, ApJ, 645, 1062

Förster Schreiber, N. M., Genzel, R., Bouché, N., et al. 2009, ApJ, 706, 1364

Förster Schreiber, N. M., Shapley, A. E., Genzel, R., et al. 2011b, ApJ, 739, 45

Förster Schreiber, N. M., Genzel, R., Newman, S. F., et al. 2014, ApJ, 787, 38

Fried, D. L. 1966, Journal of the Optical Society of America (1917-1983), 56, 1372

Galametz, A., Grazian, A., Fontana, A., et al. 2013, ApJS, 206, 10

Genel, S., Bouché, N., Naab, T., Sternberg, A., & Genzel, R. 2010, ApJ, 719, 229

Genzel, R., Tacconi, L. J., Eisenhauer, F., et al. 2006, Nature, 442, 786

Genzel, R., Newman, S., Jones, T., et al. 2011, ApJ, 733, 101

Genzel, R., Tacconi, L. J., Lutz, D., et al. 2015, ApJ, 800, 20

Glazebrook, K. 2013, PASA, 30, 56

Glazebrook, K., Ellis, R., Santiago, B., & Griffiths, R. 1995, MNRAS, 275, L19

Gonçalves, T. S., Basu-Zych, A., Overzier, R., et al. 2010, ApJ, 724, 1373

Goodwin, M., Jenkins, C., & Lambert, A. 2013, PASA, 30, 9

Governato, F., Willman, B., Mayer, L., et al. 2007, MNRAS, 374, 1479

Guo, Y., Giavalisco, M., Ferguson, H. C., Cassata, P., & Koekemoer, A. M. 2012, ApJ, 757, 120

Guo, Y., Ferguson, H. C., Bell, E. F., et al. 2015, ApJ, 800, 39

Hardy, J. W. 1998, Adaptive Optics for Astronomical Telescopes

Hartkopf, W. I., Mason, B. D., & Worley, C. E. 2001, AJ, 122, 3472

Hartmann, J. 1900a, ApJ, 11, 400

—. 1900b, ApJ, 12, 30

Herriot, G., Andersen, D., Atwood, J., et al. 2014, in Society of Photo-Optical Instrumentation Engineers (SPIE) Conference Series, Vol. 9148, Society of Photo-Optical Instrumentation Engineers (SPIE) Conference Series, 10

Hopkins, A. M., & Beacom, J. F. 2006, ApJ, 651, 142

Hopkins, P. F., Kereš, D., Murray, N., Quataert, E., & Hernquist, L. 2012, MNRAS, 427, 968

Hopkins, P. F., Narayanan, D., & Murray, N. 2013, MNRAS, 432, 2647

Iizuka, K. 2002, Elements of Photonics, Vol. 2 (New York: A John Wiley & Sons, Inc.)

Joung, M. K. R., & Mac Low, M.-M. 2006, ApJ, 653, 1266

Kassin, S. A., Brooks, A., Governato, F., Weiner, B. J., & Gardner, J. P. 2014, ApJ, 790, 89

Kassin, S. A., Weiner, B. J., Faber, S. M., et al. 2012, ApJ, 758, 106

Kennicutt, Jr., R. C. 1998, ApJ, 498, 541

Kennicutt, Jr., R. C., Calzetti, D., Walter, F., et al. 2007, ApJ, 671, 333

Kereš, D., Katz, N., Weinberg, D. H., & Davé, R. 2005, MNRAS, 363, 2

Kolmogorov, A. 1941, Akademiia Nauk SSSR Doklady, 30, 301

Kolmogorov, A. N. 1991, Royal Society of London Proceedings Series A, 434, 9

Konopacky, Q. M., Barman, T. S., Macintosh, B. A., & Marois, C. 2013, Science, 339, 1398

Lang, P., Wuyts, S., Somerville, R. S., et al. 2014, ApJ, 788, 11

Lardière, O., Andersen, D., Blain, C., et al. 2014, in Society of Photo-Optical Instrumentation Engineers (SPIE) Conference Series, Vol. 9148, Society of Photo-Optical Instrumentation Engineers (SPIE) Conference Series, 1

Larkin, J., Barczys, M., Krabbe, A., et al. 2006, in Society of Photo-Optical Instrumentation Engineers (SPIE) Conference Series, Vol. 6269, Society of Photo-Optical Instrumentation Engineers (SPIE) Conference Series

Larkin, J. E., Quirrenbach, A., Krabbe, A., et al. 2003, in Society of Photo-Optical Instrumentation Engineers (SPIE) Conference Series, Vol. 4841, Society of Photo-Optical Instrumentation Engineers (SPIE) Conference Series, ed. M. Iye & A. F. M. Moorwood, 1600–1610

Larkin, J. E., Moore, A. M., Barton, E. J., et al. 2010, in Society of Photo-Optical Instrumentation Engineers (SPIE) Conference Series, Vol. 7735, Society of Photo-Optical Instrumentation Engineers (SPIE) Conference Series

Laver, C., & de Pater, I. 2009, Icarus, 201, 172

Law, D. R., Shapley, A. E., Steidel, C. C., et al. 2012, Nature, 487, 338

Law, D. R., Steidel, C. C., Erb, D. K., et al. 2007a, ApJ, 669, 929

—. 2007b, ApJ, 669, 929

—. 2009, ApJ, 697, 2057

—. 2007c, ApJ, 656, 1

Le Fèvre, O., Saisse, M., Mancini, D., et al. 2003, in Society of Photo-Optical Instrumentation Engineers (SPIE) Conference Series, Vol. 4841, Instrument Design and Performance for Optical/Infrared Ground-based Telescopes, ed. M. Iye & A. F. M. Moorwood, 1670–1681

Lilly, S., Schade, D., Ellis, R., et al. 1998, ApJ, 500, 75

Lilly, S. J., Le Fevre, O., Hammer, F., & Crampton, D. 1996, ApJ, 460, L1

Livermore, R. C., Jones, T., Richard, J., et al. 2012, MNRAS, 427, 688

Livermore, R. C., Jones, T. A., Richard, J., et al. 2015, MNRAS, 450, 1812

Lotz, J. M., Primack, J., & Madau, P. 2004, AJ, 128, 163

Lyke, J. E., & Campbell, R. D. 2009, AJ, 138, 1090

Macintosh, B., Graham, J., Palmer, D., et al. 2006, in Society of Photo-Optical Instrumentation Engineers (SPIE) Conference Series, Vol. 6272, Society of Photo-Optical Instrumentation Engineers (SPIE) Conference Series, 0

Madau, P., & Dickinson, M. 2014, ARA&A, 52, 415

Madau, P., Ferguson, H. C., Dickinson, M. E., et al. 1996, MNRAS, 283, 1388

Maire, J., Ziad, A., Borgnino, J., et al. 2006, A&A, 448, 1225

Maire, J., Mieda, E., Steinbring, E., et al. 2014, in Society of Photo-Optical Instrumentation Engineers (SPIE) Conference Series, Vol. 9145, Society of Photo-Optical Instrumentation Engineers (SPIE) Conference Series, 3

Martin, C., Matuszewski, M., Morrissey, P., et al. 2015, Nature, doi:10.1038/nature14616

Mason, B. D., Wycoff, G. L., Hartkopf, W. I., Douglass, G. G., & Worley, C. E. 2001, AJ, 122, 3466

Matthews, D. J., Newman, J. A., Coil, A. L., Cooper, M. C., & Gwyn, S. D. J. 2013, ApJS, 204, 21

McConnell, N. J., Ma, C.-P., Gebhardt, K., et al. 2011, Nature, 480, 215

McGregor, P. J., Hart, J., Conroy, P. G., et al. 2003, in Society of Photo-Optical Instrumentation Engineers (SPIE) Conference Series, Vol. 4841, Instrument Design and Performance for Optical/Infrared Ground-based Telescopes, ed. M. Iye & A. F. M. Moorwood, 1581–1591

McGregor, P. J., Bloxham, G. J., Boz, R., et al. 2012, in Society of Photo-Optical Instrumentation Engineers (SPIE) Conference Series, Vol. 8446, Society of Photo-Optical Instrumentation Engineers (SPIE) Conference Series

McMillan, P. J. 2011, MNRAS, 414, 2446

Mieda, E., Wright, S. A., Larkin, J. E., et al. 2014, PASP, 126, 250

Moharam, M. G., & Gaylord, T. K. 1981, Journal of the Optical Society of America (1917-1983), 71, 811

Moore, A. M., Bauman, B. J., Barton, E. J., et al. 2010, in Society of Photo-Optical Instrumentation Engineers (SPIE) Conference Series, Vol. 7735, Society of Photo-Optical Instrumentation Engineers (SPIE) Conference Series

Mouhcine, M., Lewis, I., Jones, B., et al. 2005, MNRAS, 362, 1143

Murray, N., Quataert, E., & Thompson, T. A. 2010, ApJ, 709, 191

Neichel, B., Rigaut, F., Vidal, F., et al. 2014, MNRAS, 440, 1002

Nelson, E. J., van Dokkum, P. G., Brammer, G., et al. 2012, ApJ, 747, L28

Nelson, E. J., van Dokkum, P. G., Momcheva, I., et al. 2013, ApJ, 763, L16

Newman, J. A., Cooper, M. C., Davis, M., et al. 2013a, ApJS, 208, 5

Newman, S. F., Shapiro Griffin, K., Genzel, R., et al. 2012a, ApJ, 752, 111

Newman, S. F., Genzel, R., Förster-Schreiber, N. M., et al. 2012b, ApJ, 761, 43

Newman, S. F., Genzel, R., Förster Schreiber, N. M., et al. 2013b, ApJ, 767, 104

Newman, S. F., Buschkamp, P., Genzel, R., et al. 2014, ApJ, 781, 21

Noll, R. J. 1976, Journal of the Optical Society of America (1917-1983), 66, 207

Oke, J. B., Cohen, J. G., Carr, M., et al. 1995, PASP, 107, 375

Oser, L., Ostriker, J. P., Naab, T., Johansson, P. H., & Burkert, A. 2010, ApJ, 725, 2312

Osterbrock, D. E. 1989, Astrophysics of gaseous nebulae and active galactic nuclei

Pettini, M., & Pagel, B. E. J. 2004, MNRAS, 348, L59

Pfuhl, O., Gillessen, S., Eisenhauer, F., et al. 2015, ApJ, 798, 111

Planck Collaboration, Ade, P. A. R., Aghanim, N., et al. 2014, A&A, 571, A16

Queyrel, J., Contini, T., Kissler-Patig, M., et al. 2012, A&A, 539, A93

Reddy, N. A., Erb, D. K., Steidel, C. C., et al. 2005, ApJ, 633, 748

Retzlaff, J., Rosati, P., Dickinson, M., et al. 2010, A&A, 511, A50

Riffel, R. A., Storchi-Bergmann, T., & Riffel, R. 2015, MNRAS, 451, 3587

Rigaut, F., Neichel, B., Boccas, M., et al. 2014, MNRAS, 437, 2361

Rockosi, C., Stover, R., Kibrick, R., et al. 2010, in Society of Photo-Optical Instrumentation Engineers (SPIE) Conference Series, Vol. 7735, Society of Photo-Optical Instrumentation Engineers (SPIE) Conference Series, 0

Roddier, F. 1981, Progress in optics. Volume 19. Amsterdam, North-Holland Publishing Co., 1981, p. 281-376., 19, 281

Salim, S., Rich, R. M., Charlot, S., et al. 2007, ApJS, 173, 267

Salim, S., Dickinson, M., Michael Rich, R., et al. 2009, ApJ, 700, 161

Schawinski, K., Urry, C. M., Simmons, B. D., et al. 2014, MNRAS, 440, 889

Shack, R. V., & Platt, B. C. 1971, in Spring Meeting of the Optical Society of America, ed. D. S. Chairman, Optical Society of America (Optical Society of America)

Sharples, R., Bender, R., Agudo Berbel, A., et al. 2013, The Messenger, 151, 21

Sharples, R. M., Bender, R., Lehnert, M. D., et al. 2004, in Society of Photo-Optical Instrumentation Engineers (SPIE) Conference Series, Vol. 5492, Ground-based Instrumentation for Astronomy, ed. A. F. M. Moorwood & M. Iye, 1179–1186

Skelton, R. E., Whitaker, K. E., Momcheva, I. G., et al. 2014, ApJS, 214, 24

Sobral, D., Smail, I., Best, P. N., et al. 2013, MNRAS, 428, 1128

Southwell, W. H. 1980, J. Opt. Soc. Am., 70, 998

Springel, V., Frenk, C. S., & White, S. D. M. 2006, Nature, 440, 1137

Steinbring, E., Millar-Blanchaer, M., Ngan, W., et al. 2013, PASP, 125, 866

Tacconi, L. J., Genzel, R., Smail, I., et al. 2008, ApJ, 680, 246

Tacconi, L. J., Genzel, R., Neri, R., et al. 2010, Nature, 463, 781

Tacconi, L. J., Neri, R., Genzel, R., et al. 2013, ApJ, 768, 74

Thatte, N. 2010, The Messenger, 140, 26

Trippe, S., Gillessen, S., Gerhard, O. E., et al. 2008, A&A, 492, 419

Valencia-S., M., Eckart, A., Zajaček, M., et al. 2015, ApJ, 800, 125

Vanderriest, C. 1980, PASP, 92, 858

Vanzella, E., Cristiani, S., Dickinson, M., et al. 2008, A&A, 478, 83

Vogt, N. P., Forbes, D. A., Phillips, A. C., et al. 1996, ApJ, 465, L15

Vogt, N. P., Phillips, A. C., Faber, S. M., et al. 1997, ApJ, 479, L121

Weiner, B. J., Willmer, C. N. A., Faber, S. M., et al. 2006, ApJ, 653, 1027

Whitaker, K. E., van Dokkum, P. G., Brammer, G., & Franx, M. 2012, ApJ, 754, L29

Wilson, R. W. 2002, MNRAS, 337, 103

Wirth, G. D., Willmer, C. N. A., Amico, P., et al. 2004, AJ, 127, 3121

Wisnioski, E., Glazebrook, K., Blake, C., et al. 2012, MNRAS, 422, 3339

—. 2011, MNRAS, 417, 2601

Wisnioski, E., Förster Schreiber, N. M., Wuyts, S., et al. 2015, ApJ, 799, 209

Wizinowich, P. L., Le Mignant, D., Bouchez, A. H., et al. 2006, PASP, 118, 297

Wright, S. A., Larkin, J. E., Graham, J. R., & Ma, C.-P. 2010, ApJ, 711, 1291

Wright, S. A., Larkin, J. E., Law, D. R., et al. 2009, ApJ, 699, 421

Wright, S. A., Larkin, J. E., Barczys, M., et al. 2007, ApJ, 658, 78

Wurster, J., & Thacker, R. J. 2013, MNRAS, 431, 2513

Wuyts, S., Förster Schreiber, N. M., Genzel, R., et al. 2012, ApJ, 753, 114

Zernike, v. F. 1934, Physica, 1, 689

Zitrin, A., Labbé, I., Belli, S., et al. 2015, ApJ, 810, L12